

UC Riverside

UC Riverside Electronic Theses and Dissertations

Title

Evaluating Nanopores for the Rapid, Direct, and Quantitative Analysis of Biomolecules and the Products of Proteolysis

Permalink

<https://escholarship.org/uc/item/35j3k6s7>

Author

Lastra, Lauren Samantha

Publication Date

2023

Peer reviewed|Thesis/dissertation

UNIVERSITY OF CALIFORNIA
RIVERSIDE

Evaluating Nanopores for the Rapid, Direct, and Quantitative Analysis of Biomolecules
and the Products of Proteolysis

A Dissertation submitted in partial satisfaction
of the requirements for the degree of

Doctor of Philosophy

in

Bioengineering

by

Lauren Samantha Lastra

June 2023

Dissertation Committee:

Dr. Kevin Freedman, Chairperson

Dr. William Grover

Dr. Geert Schmid-Shönbein

Copyright by
Lauren Samantha Lastra
2023

The Dissertation of Lauren Samantha Lastra is approved:

Committee Chairperson

University of California, Riverside

ACKNOWLEDGMENTS

.

Thank you to my family, friends, and colleagues for supporting and advising me on this journey.

ABSTRACT OF THE DISSERTATION

Evaluating Nanopores for the Rapid, Direct, and Quantitative Analysis of Biomolecules
and the Products of Proteolysis

by

Lauren Samantha Lastra

Doctor of Philosophy, Graduate Program in Bioengineering
University of California, Riverside, June 2023
Dr. Kevin Freedman, Chairperson

Modern diagnostics strive to be accurate, fast, and inexpensive and aim to properly identify the presence of a disease, infection, or illness. Early diagnosis is key to earlier therapeutic intervention, which can improve prognosis and reduce mortality. The challenge with many diseases is that detectability of the disease scales with disease progression. Modern diagnostic techniques exhibit a specific threshold to be surpassed for accurate, reliable tests to be performed. Often, symptoms do not appear until disease progression has

reached a significant stage. Since single molecule sensors, e.g., nanopores, can sense biomolecules at extremely low concentrations, they have the potential to become clinically relevant in many of today's medical settings. The nanopore-detected current measurements can be used to identify disease biomarkers, determine the presence of pathogens, and monitor the efficacy of drugs. Specifically, solid-state nanopores offer several advantages over traditional diagnostic tools such as speed, accuracy, and cost-effectiveness. As a result, they have become an increasingly popular tool in the diagnostic field and are expected to play a critical role in the development of personalized medicine.

In the first chapter, we investigate the origins of current enhancing events under low ionic strength conditions and propose an alternative theory for the observation of conductive events. Utilizing electroosmotic flow, we show that a flux imbalance in favor of cations allows for detection of DNA and protein to be divergent. In the second chapter, we expand upon low ionic strength conditions to high and asymmetric electrolyte conditions to examine differences in signal-to-noise ratio, molecule dwell time, and configuration. In asymmetric salt, we show the ability of detecting differences in DNA configuration as well as protein alone and bound to DNA complexes, superior to that of the gold standard sensing conditions. Following that, several denaturing agents are integrated into the nanopore system, serving to linearize and provide a uniform negative charge to both whole proteins and peptides of varying lengths. With this, a novel electrolyte sensing condition is introduced that allows for peptide length to be distinguishable by changes in the current amplitude upon molecule translocation via electrophoretic forces.

Lastly, we critically analyze peptide fragments generated by protease digestion in whole blood using a portable device. The utilization of nanopores in this study goes beyond serving as only a sensing device; rather, it represents a breakthrough in the field of diagnostics, as it opens up the possibility of monitoring protease activity levels within the body.

Table of Contents

Chapter 1: Introduction	1
1.1 Nanotechnology and Single Molecule Motivation	1
1.2 The Autodigestion Theory	2
1.3 Different Classes of Nanopores	3
1.4 Nanopore Detection Information	6
1.5 Innovation and Significance	9
1.6 Objectives and Specific Aims	10
1.6.1 Specific Aim 1: Evaluation of Conductive Pulse Sensing and Its Mechanisms for Enhanced Molecular Sensing.....	11
1.6.2 Specific Aim 2: Evaluating Electrolyte Conditions for Enhanced Detection of DNA and Protein Complexes	12
1.6.3 Specific Aim 3: Enhancing Peptide Length Discrimination by Integrating Denaturing Agents	12
1.6.4 Specific Aim 4: Real-time, Nanopore-Based Monitoring of Enzymatically Active Protease in Whole Blood	13
1.7 References.....	14
Chapter 2: Evaluation of Conductive Pulse Sensing and Its Mechanisms for Enhanced Molecular Sensing	19
2.1 Abstract	19
2.2 Introduction.....	19
2.3 Results and Discussion	24
2.3.1 λ -DNA Translocation in Symmetric Low Salt Conditions.....	25
2.3.2 λ -DNA Translocation in Asymmetric High Salt Conditions.....	29
2.3.3 Alkali Chloride Dependence on Event Characteristics.....	35
2.3.4 Protein Conductive Events at Asymmetric Salt Conditions	39
2.3.5 Mechanistic Insight into Conductive Events	42
2.4 Conclusion	44
2.5 Materials and Methods.....	45
2.5.1 Nanopore Preparation	45
2.5.2 Data Acquisition	46
2.5.3 Finite Elements Methods	46

2.6 References	48
Chapter 3: Evaluating Electrolyte Conditions for Enhanced Detection of DNA and Protein Complexes	53
3.1 Abstract	53
3.2 Introduction	54
3.3 Results and Discussion	59
3.3.1 Various Electrolyte Conditions	59
3.3.2 Signal Properties of High Symmetric Compared to High Asymmetric	63
3.3.3 Machine Learning Techniques	65
3.3.4 Event Characteristic Differences Between Symmetric and Asymmetric Salt	70
3.3.5 Molecular Carrier Detection Under Asymmetric Conditions	73
3.4 Conclusion	77
3.5 Materials and Methods	78
3.5.1 Fabrication of Nanopores	78
3.5.2 Electrolyte Preparation	79
3.5.3 Biomolecule Preparation and Translocation Experiments	79
3.5.4 Data Analysis and Machine Learning	80
3.6 References	81
Chapter 4: Enhancing Peptide Length Discrimination by Integrating Denaturing Agents	86
4.1 Abstract	86
4.2 Introduction	87
4.3 Results and Discussion	91
4.3.1 Critical micelle concentration of sodium dodecyl sulfate	91
4.3.2 Detection of Peptides in Denaturing Solution	92
4.3.3 Signal-to-Noise Study in Denaturing Solution	96
4.3.4 Multiplexed Sensing of Peptides Using a Peptide Ladder	99
4.4 Conclusion	102
4.5 Materials and Methods	103
4.5.1 Nanopore Preparation	103
4.5.2 Denaturing Solution and Preparation	104

4.5.3 Data Acquisition and Analysis.....	105
4.6 References.....	106
Chapter 5: Real-time, Nanopore-Based Monitoring of Enzymatically Active Protease in Whole Blood.....	110
5.1 Abstract.....	110
5.2 Introduction.....	111
5.3 Results and Discussion.....	115
5.3.1 Peptide and Protein Characterization in High Ionic Strength Solution.....	115
5.3.2 BSA Digested via Trypsin.....	120
5.3.3 Development of Real-Time Digestion Device.....	123
5.3.4 Autodigestion Observation in Whole Blood.....	124
5.4 Conclusion.....	131
5.5 Materials and Methods.....	132
5.5.1 PDMS Chip Fabrication.....	132
5.5.2 Fabrication of Quartz Nanopipettes.....	134
5.5.3 Electrolyte and Sample Preparation.....	134
5.5.4 Data Acquisition and Analysis.....	135
5.6 References.....	136
Chapter 6: Conclusion and Outlook.....	139
Appendix A: Evaluation of Conductive Pulse Sensing and Its Mechanisms for Enhanced Molecular Sensing.....	144
Appendix B: Evaluating Electrolyte Conditions for Enhanced Detection of DNA and Protein Complexes.....	162

List of Figures

Figure 1. 1: Nanopore Types.	5
Figure 1. 2: Open Pore vs Blocked Pore.....	7
Figure 1. 3: Nanopore Pathway	10
Figure 2. 1: EOF Characterization	27
Figure 2. 2: Comparison Between Various Electrolyte Conditions.....	31
Figure 2. 3: Cationic Flux Imbalance.	35
Figure 2. 4: Lithium and Cesium Chloride Characterization.....	39
Figure 2. 5: Protein Sensing.....	41
Figure 3. 1: Comparison Between Various Concentration Gradients.....	61
Figure 3. 2: Event Property Comparisons.....	63
Figure 3. 3: DNA Folding.....	67
Figure 3. 4: Principal Folding Component Analysis.	69
Figure 3. 5: Dwell Time Comparisons.....	72
Figure 3. 6: Molecular Carrier Detection.....	76
Figure 4. 1: Peptide Characterization in Denaturing Solution.....	91
Figure 4. 2: Signal Dependence on Concentration.	93
Figure 4. 3: Signal-to-Noise Ratio Comparison.	97
Figure 4. 4: Peptide Ladder Translocations.	101
Figure 5. 1: Peptide Detection in 1 M KCl.	117
Figure 5. 2: Protein Detection in 1 M KCl.....	118
Figure 5. 3: BSA Digested via Trypsin at Two Time Points.....	120
Figure 5. 4: Switch from Semi-Continuous to Real-Time Detection	122
Figure 5. 5: Event Properties of Blood Spiked with Trypsin.....	127
Figure 5. 6: Distinguishing Parameters for an Autodigestive State.....	128

List of Tables

Table 1.1: Protein Sensing Challenges.	9
Table 5.1: Biomolecules in Blood..	124
Table 5.2: Current Traces in Blood.....	126

Chapter 1: Introduction

1.1 Nanotechnology and Single Molecule Motivation

Nanotechnology represents the interdisciplinary integration of sciences, engineering, and technology, all conducted at the nanoscale level (<100 nm). The truly captivating aspect of nanoscience lies in the notion that the physics and associated properties governing the macroscopic world differ significantly from those governing the nanoscale realm. However, working at such a minute scale presents a challenge in that visualization requires sophisticated microscopy tools¹ that are often costly and can entail lengthy sample processing steps. To circumvent this, alternative techniques have been developed to explore the nanoscale world without relying on expensive imaging methods. The initial discovery of the nanopore's ability to detect single-stranded DNA using α -hemolysin (α -HL) was published in 1996 by Kasianowicz et. al.², representing a landmark achievement in the field. Since then, the development of other nanopore forms has greatly expanded the range of applications, detection methods, and analyte characterization techniques³⁻⁵. Over the past 30 years, nanopores have demonstrated remarkable capability in specific recognition and quantification of single molecules⁶.

Since the demonstration of using biological nanopores as a single molecule sensor, solid-state nanopores have been developed as a more robust and highly tunable, counterpart⁷. Additionally, nanopores have several advantages in various applications due to their unique properties such as sensitivity, high throughput, and versatility. Firstly, nanopores are highly sensitive to their environmental conditions such as alkali chloride type^{8,9}, electrolyte concentration¹⁰, pH¹¹, and analyte type¹². They also have an extremely

lower detection limit, down to the femtomolar regime¹³ and can be used in heterogeneous samples to analyze multiple molecules simultaneously¹⁴⁻¹⁶. Other features include portability and versatility; the commercially available MinION is the size of a USB stick and can be transported readily¹⁷. For versatility, the nanopore can be used to detect a variety of synthetic¹⁸ and biological molecules¹¹. Lastly, and perhaps most importantly for this study, real-time and label-free detection is possible with nanopores¹⁹⁻²¹. In this work, we document observations of DNA, protein, DNA – protein complexes, and peptides in both homogeneous and highly heterogeneous samples.

1.2 The Autodigestion Theory

Hemorrhagic shock refers to the dangerous and frequently deadly condition that occurs when the body experiences significant blood loss, leading to inadequate perfusion of the tissues. Shock remains the leading cause of death in the intensive care unit (ICU), despite extensive research into the pathophysiology of the condition²². Hemorrhagic shock is often followed by the most common form of shock, hypovolemic shock (HS), which stems from insufficient circulating blood volume²³. There are four stages in HS: initial, compensatory, progressive, and refractory. Accurate diagnosis must occur before refractory period, as it is at this time when the patient has lost more than 40% of their blood volume and the chance of survival is severely limited²⁴. Unfortunately, HS symptoms can vary greatly depending on age, health, cause of injury, and how much blood has been lost, emphasizing the need for an accurate, quick, diagnostic device.

The system-wide destruction, including multiple organ failure, initiates because of the autodigestion theory²⁵. This theory starts in the pancreas, where trypsin is produced. Once trypsin is made, it is shuttled into the small intestine, where it fulfills its duty by digesting proteins from previously eaten food. Under healthy circumstances, trypsin is sequestered in the small intestine, as the epithelial villi effectively restricts the diffusion of enzymes, such as proteases and lipases, into the bloodstream. However, under a state of autodigestion, the mucosal layer within the intestinal lining breaks down, allowing trypsin to escape into the cardiovascular system and continue proteolysis in other organs^{26,27}. Therefore, the loss of barrier function at the epithelial and mucosal layers of the intestine implicates digestive enzymes as key factors in systemic dysfunction and disrupt homeostasis in the body^{28,29}. Of these enzymes, trypsin, a protease, has been the focus of recent studies, with mounting evidence pointing to its key role in shock.

1.3 Different Classes of Nanopores

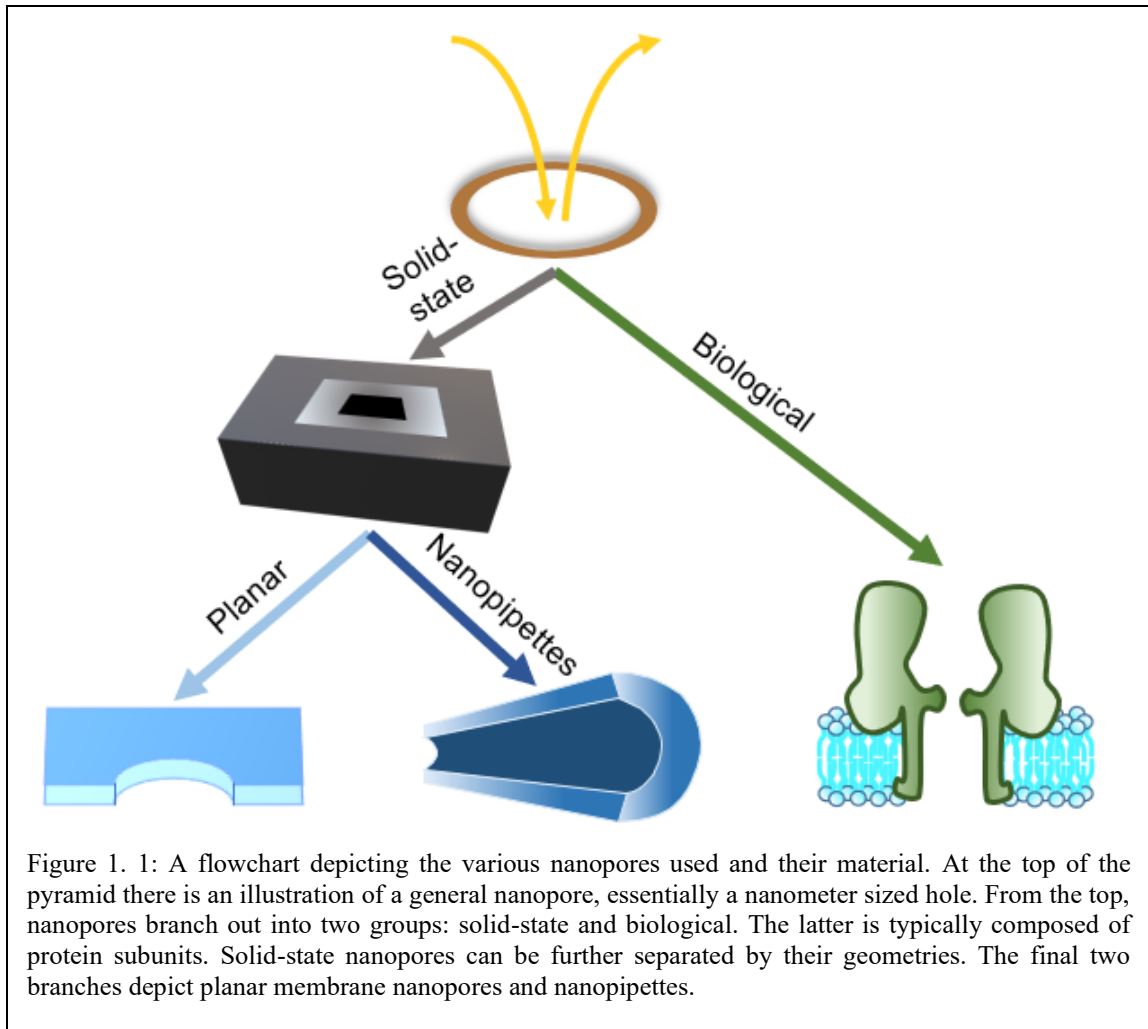
Nanopores, both biological and solid-state (Figure 1.1), have emerged as powerful tools for various sensing and analysis applications. Biological nanopores are protein-based channels found in cell membranes, such as the α -HL pore. They offer unique advantages, including high selectivity and sensitivity^{30,31}. For example, the MinION is capable of rapid sequencing and holds promise as a portable diagnostic tool to identify pathogens and antimicrobial resistance profiles³²⁻³⁴. Additionally, the current gold standard for the detection of oligopeptides (ranging from 2-20 amino acids in length) is typically performed using biological nanopores^{35,36}. However, in this thesis, we demonstrate that solid-state

nanopores (i.e., quartz nanopipettes) can also effectively detect oligopeptides, providing an alternative approach to the established benchmark for short peptide detection.

Challenges in utilizing biological nanopores arise due to limitations in stability, fabrication, and control over their properties. On the other hand, solid-state nanopores are artificially created pores in solid materials, such as silicon nitride or graphene^{37,38}. They provide excellent controllability and stability, making them well-suited for diverse applications. Solid-state nanopores offer high spatial resolution, allowing for precise measurements of molecules passing through the pore. They can be fabricated with different geometries, such as planar membrane nanopores and quartz nanopipettes.

Planar membrane nanopores and quartz nanopipettes represent two different geometries within the realm of solid-state nanopores, each with its own set of advantages and considerations. Planar membrane nanopores, formed by thin films of solid-state materials, provide straightforward fabrication and scalability. They are suitable for high-throughput analysis and have been extensively used in single-molecule sensing. However, planar membrane nanopores suffer from limitations such as the potential for pore clogging and challenges in achieving uniform pore size distribution. Conversely, quartz nanopipettes have a needle-like geometry and are fabricated from quartz or borosilicate capillaries^{39,40}. They offer ease of fabrication, small physical size, and targeted location analysis.

Biological and solid-state nanopores offer distinct advantages and challenges in terms of selectivity, stability, and controllability, providing researchers with versatile options for a wide range of sensing and analysis tasks. While planar silicon nitride



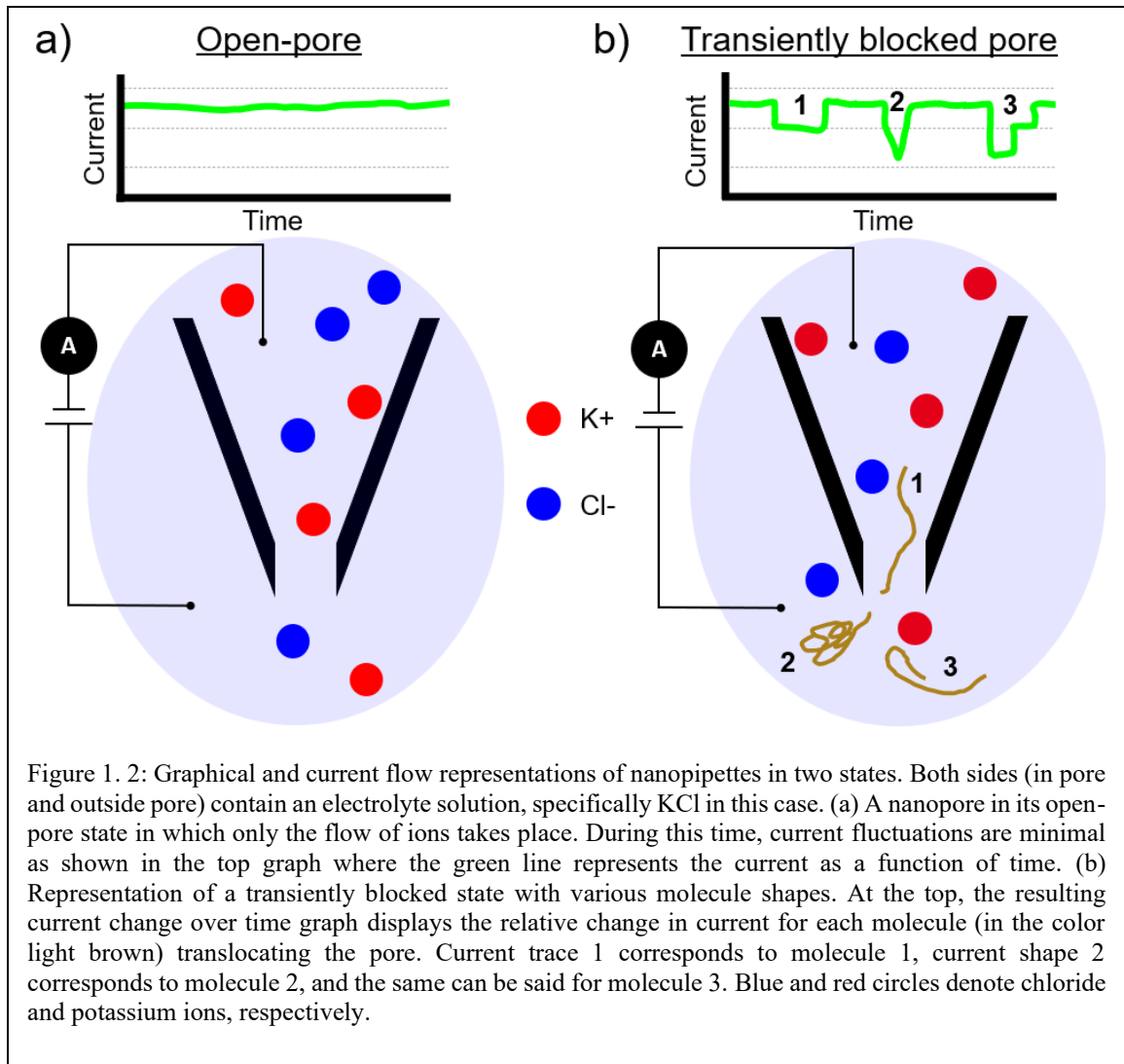
membranes have been predominantly used for nanopore-based protein sensing due to their well-defined pore length, nanopipettes present an alternative with unique benefits. Unlike planar membranes, nanopipettes have a gradual taper length that extends the sensing region of the device^{41,42}. This, combined with their straightforward fabrication methods and ability

to fit into confined spaces, makes nanopipettes the ideal choice of nanopore type for the current work. Nanopipettes have been shown to be capable of sensing within a heterogeneous sample¹⁴, and its long taper length will be of great usage for inserting into the PDMS chip for detection of cleaved peptide fragments from trypsin digestion.

1.4 Nanopore Detection Information

By applying a voltage across a nanoscale aperture, molecules are driven either into or out of the pore, leading to a change in ionic current (i.e. current blockade or current enhancement)⁴³, which is constituted as an “event”. Each event is characterized by the change in current and dwell time (time spent within the pore) which corresponds to the molecule size and charge (among a few other molecule characteristics like length and shape), respectively^{44,45}. Using this technique, some level of molecular discrimination/recognition is possible (Figure 1.2), however, signals are not always mutually exclusive. This thesis will focus on nanopore sensors and their ability to detect polynucleotides, proteins, and peptides generated via protease digestion as a means to obtain diagnostic information.

Since the first nanopore experiment detecting nucleic acids², DNA has become one of the most prevalently used molecule for nanopore research. This is due to their highly negatively charged and linear structure. Because sequencing using solid-state nanopores has not been achieved to date, many efforts have been made to slow down the translocation



of DNA through a solid-state nanopore^{9,10,46}. Additionally, DNA can be thought of as a flexible linear molecule and as such, can enter the nanopore in a variety of different configurations⁴⁷⁻⁴⁹. As nanopore research expands to include molecules other than DNA, it is of utmost importance to characterize and be familiar with the event properties that provide information regarding the molecule attributes. For this reason, our first chapters involve detecting DNA and understanding how various alterations (like electrolyte type, concentration, and method of translocation) affect the signal and the molecule itself. With

this well-developed foundation, we can increase the complexity to detecting molecular carriers (protein bound to DNA) and proteins in their globular state.

Protein detection in solid-state nanopores can be complicated as proteins are composed of differently charged subunits (Table 1.1). Additionally, proteins tend to non-specifically adsorb to solid-state surfaces, preventing proteins from passing through the pore for analysis⁵⁰. To address this issue, researchers utilize what are called molecular carriers to assist in detecting proteins. The motivation for this is that since DNA is simpler in its structure, DNA can be employed as a carrier of a target protein. By mixing the target protein with a DNA molecular carrier, they can form a complex and translocate the pore together. The DNA aids in slowing down the protein and provides a distinct event shape to positively identify protein bound to DNA^{10,14}. This was the focus of our next chapter, as we conceived the idea to detect trypsin that had escaped from the small intestine using DNA as a molecular carrier. In this sense, we could positively identify that trypsin was present in the blood. Upon further investigation, we came to the realization that identification does not indicate function. In other words, the presence of trypsin does not reveal trypsin activity in the blood. Consequently, we pivoted our strategy to detecting peptide fragments generated from trypsin activity in the blood.

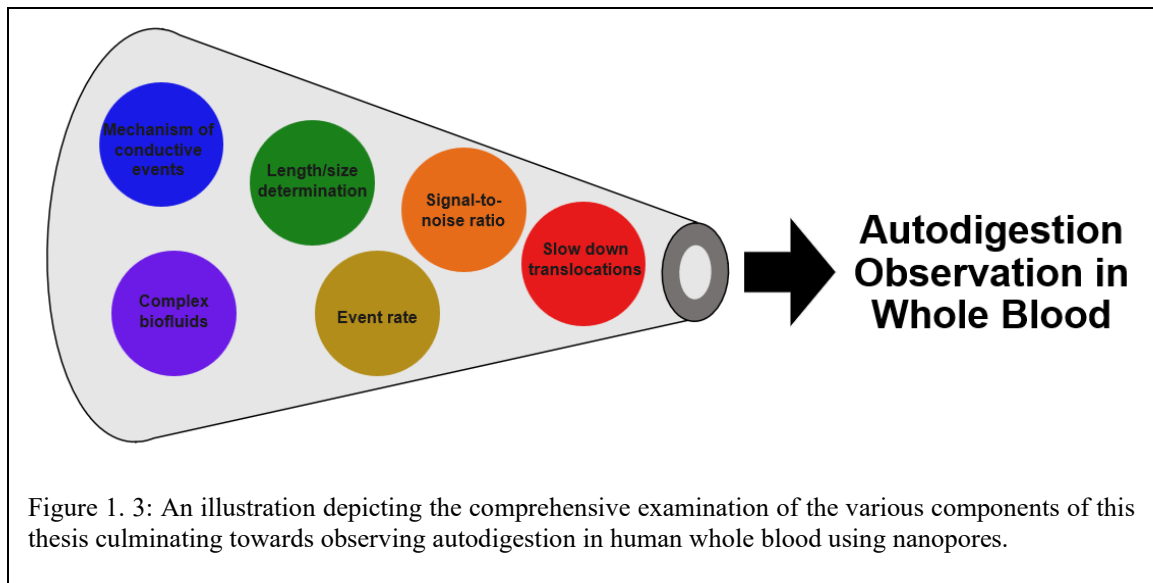
Table 1.1: Descriptions of the well-known challenges when working with proteins as an analyte. The corresponding references either show this obstacle occurring and/or try to alleviate the stated issue.

Protein Sensing Challenges	Description	References
Adsorption and Clogging	Nonspecific adsorption of proteins onto nanopore walls can elicit changes in event characteristics and lead to permanent clogging	Cai et. al. ⁵¹ , Niedzwieki et. al. ⁵² , Awasthi et. al. ⁵³
Fast Translocations	Proteins are compact and globular in structure, allowing them to pass through the pore far more rapidly leading to short dwell times and signal attenuation	Carlsen et. al. ⁵⁴ , Plesa et. al. ⁵⁵
Multiple Conformations	Proteins consist of transitional and conformational structures that can unfold at higher voltages which will modify event properties	Freedman et. al. ⁵⁶ , Li et. al. ⁵⁷
Lower Signal-to-Noise Ratio	Solid-state nanopores exhibit lower signal-to-noise ratio in comparison to their biological counterparts and with difficult to detect analytes (i.e., protein), this challenge is exacerbated	Bandara et. al. ¹¹ , Larkin et. al. ⁵⁸

1.5 Innovation and Significance

The use of nanopores to detect peptide fragments generated by trypsin cleavage represents a major innovation in the diagnosis and monitoring of shock. By capturing these fragments in real-time, it is possible to detect the early stages of autodigestion and to monitor the progression of shock (Figure 1.3). This is particularly significant given the high mortality rate associated with shock, which is often due to delays in diagnosis and treatment. With this new diagnostic approach, doctors will be able to detect shock much earlier and take appropriate measures to prevent its progression.

In addition to its potential clinical applications, the use of nanopores to detect peptide fragments generated by trypsin cleavage also represents an important contribution



to our understanding of the underlying mechanisms of shock. By studying the behavior of these fragments in real-time, researchers can gain new insights into the progression of shock and the role of autodigestion in its development. This, in turn, may lead to the development of new therapeutic approaches that target this critical aspect of the disease. Overall, the use of nanopores to detect peptide fragments generated by trypsin cleavage is a significant advancement in both diagnostic and research applications, with the potential to revolutionize the field of shock management. The central hypothesis motivating this research is that leakage of protease into the circulatory system is a defining feature of shock and quantification of the peptides generated from enzymatically active protease in blood via nanopores will lead to better care of patients and understanding of the disease state.

1.6 Objectives and Specific Aims

To achieve the objective of fabricating a portable device to monitor the protease activity levels in blood using a nanopore, a set of specific aims was developed at the

conception of this study. We propose nanopore technology to obtain a purely electrical (i.e., label-free) signal that can discriminate single molecules according to their individual properties. By applying an electric field across a nanoscale aperture, electrophoretic forces drive molecules into the pore leading to a change in ionic current⁵⁹. This approach was chosen due to its ability to sense molecules at low concentrations as well as the ability to obtain data in real time⁶⁰. Using nanopores to monitor transient variations in the activity level of proteases in the bloodstream will aid in rapidly diagnosing shock and play a role in selecting appropriate interventions. This thesis will work towards the development of a nanodiagnostic tool through the following aims.

1.6.1 Specific Aim 1: Evaluation of Conductive Pulse Sensing and Its Mechanisms for Enhanced Molecular Sensing

In low ionic strength conditions, the electroosmotic flow (EOF) becomes more prominent. The aim of this project is to use EOF to translocate both DNA and proteins for the preparation of molecular carrier design (DNA bound to trypsin) and concentration quantification. The study will determine the effects of two competing metrics, electrophoretic forces and EOF, on molecule translocation time. By the end of this aim, we expect to detect DNA-Protein complexes in low ionic strength conditions and establish a solid foundation for developing molecular carriers and nanopore sensing techniques for the detection of trypsin.

1.6.2 Specific Aim 2: Evaluating Electrolyte Conditions for Enhanced Detection of DNA and Protein Complexes

The optimization of signal-to-noise ratio (SNR) is crucial for accurate and precise detection of the presence of molecular carriers. This aim focuses on determining the optimal electrolyte concentration and method of detection for producing concentration measurements. The project will synthesize molecular carriers (Lambda-phage DNA) to bind specifically to proteins (Cas9) to prepare for the detection of trypsin using molecular carriers in the future. In addition, the study will optimize electrolyte concentrations that allow for a high current amplitude signal without clogging the pore. This aim will set the groundwork for developing and testing molecular carriers and nanopore sensing techniques to accurately detect trypsin bound to DNA.

1.6.3 Specific Aim 3: Enhancing Peptide Length Discrimination by Integrating Denaturing Agents

Pivoting away from molecular carrier detection and towards detecting peptide fragments generated by trypsin (mimicking a state of autodigestion) motivated the development of different electrolyte conditions to characterize peptide length. By detecting the peptide fragments after digestion, we acquire a more detailed view surrounding the enzymatic activity level. With this, incorporation of denaturing agents is employed to unfold, provide a uniformly negative charge, and linearize all molecules within the sample. The results of this study will provide crucial information about the event characteristics that distinguish peptide length, paving the way for future research.

1.6.4 Specific Aim 4: Real-time, Nanopore-Based Monitoring of Enzymatically Active Protease in Whole Blood

In this aim, we will fabricate a device to detect peptide fragments and proteins in real-time by integrating a dialysis unit with solid-state nanopores and a custom-made PDMS chip. The study will investigate the activity levels of trypsin within the blood, representing a state of autodigestion, using solid-state nanopores. The aim is to develop a device that can provide real-time monitoring of peptide fragments generated during trypsin digestion in whole blood. The results of this study will provide a deeper understanding of protease activity, which can help develop better treatment strategies for diseases related to autodigestion.

1.7 References

1. Moerner, W. E. (William E.). Single-Molecule Spectroscopy, Imaging, and Photocontrol: Foundations for Super-Resolution Microscopy (Nobel Lecture). *Angewandte Chemie International Edition* **54**, 8067–8093 (2015).
2. Kasianowicz, J. J., Brandin, E., Branton, D. & Deamer, D. W. Characterization of individual polynucleotide molecules using a membrane channel. *Proceedings of the National Academy of Sciences* **93**, 13770–13773 (1996).
3. Branton, D. *et al.* The potential and challenges of nanopore sequencing. *Nature Biotechnology* vol. 26 1146–1153 Preprint at <https://doi.org/10.1038/nbt.1495> (2008).
4. Schneider, G. F. & Dekker, C. DNA sequencing with nanopores. *Nature Biotechnology* vol. 30 326–328 Preprint at <https://doi.org/10.1038/nbt.2181> (2012).
5. Clarke, J. *et al.* Continuous base identification for single-molecule nanopore DNA sequencing. *Nature Nanotech* **4**, 265–270 (2009).
6. Howorka, S. & Siwy, Z. Nanopore analytics: Sensing of single molecules. *Chemical Society Reviews* **38**, 2360–2384 (2009).
7. Dekker, C. Solid-state nanopores. *Nature Nanotechnology* **2**, 209–215 (2007).
8. Lastra, L. S., Bandara, Y. M. N. D. Y., Nguyen, M., Farajpour, N. & Freedman, K. J. On the origins of conductive pulse sensing inside a nanopore. *Nat Commun* **13**, 2186 (2022).
9. Kowalczyk, S. W., Wells, D. B., Aksimentiev, A. & Dekker, C. Slowing down DNA Translocation through a Nanopore in Lithium Chloride. *Nano Lett.* **12**, 1038–1044 (2012).
10. Lastra, L. S., Bandara, Y. M. N. D. Y., Sharma, V. & Freedman, K. J. Protein and DNA Yield Current Enhancements, Slow Translocations, and an Enhanced Signal-to-Noise Ratio under a Salt Imbalance. *ACS Sens.* **7**, 1883–1893 (2022).
11. Bandara, Y. M. N. D. Y., Farajpour, N. & Freedman, K. J. Nanopore Current Enhancements Lack Protein Charge Dependence and Elucidate Maximum Unfolding at Protein's Isoelectric Point. *J. Am. Chem. Soc.* **144**, 3063–3073 (2022).
12. Chau, C. C., Radford, S. E., Hewitt, E. W. & Actis, P. Macromolecular Crowding Enhances the Detection of DNA and Proteins by a Solid-State Nanopore. *Nano Lett.* **20**, 5553–5561 (2020).

13. Freedman, K. J. *et al.* Nanopore sensing at ultra-low concentrations using single-molecule dielectrophoretic trapping. *Nature Communications* **7**, 10217 (2016).
14. Sze, J. Y. Y., Ivanov, A. P., Cass, A. E. G. & Edel, J. B. Single molecule multiplexed nanopore protein screening in human serum using aptamer modified DNA carriers. *Nature Communications* **8**, 1552 (2017).
15. Chuah, K. *et al.* Nanopore blockade sensors for ultrasensitive detection of proteins in complex biological samples. *Nat Commun* **10**, 2109 (2019).
16. Im, J., Lindsay, S., Wang, X. & Zhang, P. Single Molecule Identification and Quantification of Glycosaminoglycans Using Solid-State Nanopores. *ACS Nano* **13**, 6308–6318 (2019).
17. Carr, C. E. *et al.* Nanopore sequencing at Mars, Europa, and microgravity conditions. *npj Microgravity* **6**, 1–6 (2020).
18. Maccaferri, N., Vavassori, P. & Garoli, D. Magnetic control of particle trapping in a hybrid plasmonic nanopore. *Applied Physics Letters* **118**, 193102 (2021).
19. Thakur, A. K. & Movileanu, L. Real-time measurement of protein–protein interactions at single-molecule resolution using a biological nanopore. *Nat Biotechnol* **37**, 96–101 (2019).
20. Haque, F., Li, J., Wu, H.-C., Liang, X.-J. & Guo, P. Solid-State and Biological Nanopore for Real-Time Sensing of Single Chemical and Sequencing of DNA. *Nano Today* **8**, 56–74 (2013).
21. Fuller, C. W. *et al.* Real-time single-molecule electronic DNA sequencing by synthesis using polymer-tagged nucleotides on a nanopore array. *Proceedings of the National Academy of Sciences of the United States of America* **113**, 5233–5238 (2016).
22. Vincent, J. L. & De Baker, D. Circulatory Shock. <http://dx.doi.org/10.1056/NEJMc1314999> (2014) doi:10.1056/NEJMc1314999.
23. *Tintinalli's emergency medicine: a comprehensive study guide.* (McGraw-Hill Education, 2019).
24. Gutierrez, G., Reines, Hd. & Wulf-Gutierrez, M. E. Clinical review: Hemorrhagic shock. *Critical Care* **8**, 373 (2004).
25. Rossaint, J. & Zarbock, A. Pathogenesis of Multiple Organ Failure in Sepsis. *CRI* **35**, (2015).

26. Schmid-Schönbein, G. W. & Chang, M. The Autodigestion Hypothesis for Shock and Multi-organ Failure. *Ann Biomed Eng* **42**, 405–414 (2014).
27. Baker, J. W., Deitch, E. A., Li, M. A., Berg, R. D. & Specian, R. D. Hemorrhagic Shock Induces Bacterial Translocation from the Gut. *Journal of Trauma and Acute Care Surgery* **28**, 896–913 (1988).
28. Altshuler, A., Kistler, E. & Schmid-Schönbein, G. Autodigestion: Proteolytic Degradation and Multiple Organ Failure in Shock. *Shock* **45**, 483–489 (2016).
29. Aletti, F. *et al.* Peptidomic Analysis of Rat Plasma: Proteolysis in Hemorrhagic Shock. *Shock* **45**, 540–554 (2016).
30. Cao, J. *et al.* Giant single molecule chemistry events observed from a tetrachloroaurate(III) embedded Mycobacterium smegmatis porin A nanopore. *Nat Commun* **10**, 5668 (2019).
31. S. Júnior, J. J. *et al.* Alpha-hemolysin nanopore allows discrimination of the microcystins variants. *RSC Advances* **9**, 14683–14691 (2019).
32. Chapman, R. *et al.* Nanopore-Based Metagenomic Sequencing in Respiratory Tract Infection: A Developing Diagnostic Platform. *Lung* **201**, 171–179 (2023).
33. Wang, J. MinION nanopore sequencing of an influenza genome. *Frontiers in Microbiology* **6**, 766 (2015).
34. Kilianski, A. *et al.* Use of unamplified RNA/cDNA-hybrid nanopore sequencing for rapid detection and characterization of RNA viruses. *Emerging Infectious Diseases* **22**, 1448–1451 (2016).
35. Hu, Z.-L. *et al.* Nanopore Deciphering Single Digital Polymers Towards High-Density Data Storage. *Chemistry – A European Journal* **29**, e202203919 (2023).
36. Fujita, S., Kawamura, I. & Kawano, R. Cell-Free Expression of De Novo Designed Peptides That Form β -Barrel Nanopores. *ACS Nano* **17**, 3358–3367 (2023).
37. Karawdeniya, B. I., Bandara, Y. M. N. D. Y., Nichols, J. W., Chevalier, R. B. & Dwyer, J. R. Surveying silicon nitride nanopores for glycomics and heparin quality assurance. *Nat Commun* **9**, 3278 (2018).
38. Merchant, C. A. *et al.* DNA Translocation through Graphene Nanopores. *Nano Lett.* **10**, 2915–2921 (2010).
39. Farajpour, N., S. Lastra, L., Sharma, V. & J. Freedman, K. Measuring trapped DNA at the liquid-air interface for enhanced single molecule sensing. *Nanoscale* **13**, 5780–5790 (2021).

40. Farajpour, N., Lastra, L. S., Sharma, V. & Freedman, K. J. Calibration-Less DNA Concentration Measurements Using EOF Volumetric Flow and Single Molecule Counting. *Frontiers in Nanotechnology* **3**, (2021).
41. Ying, Y.-L., Cao, C. & Long, Y.-T. Single molecule analysis by biological nanopore sensors. *Analyst* **139**, 3826–3835 (2014).
42. Fragasso, A., Schmid, S. & Dekker, C. Comparing Current Noise in Biological and Solid-State Nanopores. *ACS Nano* **14**, 1338–1349 (2020).
43. Kesselheim, S., Müller, W. & Holm, C. Origin of Current Blockades in Nanopore Translocation Experiments. *Phys. Rev. Lett.* **112**, 018101 (2014).
44. Keyser, U. F. *et al.* Direct force measurements on DNA in a solid-state nanopore. *Nature Physics* **2**, 473–477 (2006).
45. Heins, E. A., Siwy, Z. S., Baker, L. A. & Martin, C. R. Detecting Single Porphyrin Molecules in a Conically Shaped Synthetic Nanopore. *Nano Lett.* **5**, 1824–1829 (2005).
46. Sharma, V., Farajpour, N., Lastra, L. S. & Freedman, K. J. DNA Coil Dynamics and Hydrodynamic Gating of Pressure-Biased Nanopores. *Small* **18**, 2106803 (2022).
47. Kumar Sharma, R., Agrawal, I., Dai, L., Doyle, P. S. & Garaj, S. Complex DNA knots detected with a nanopore sensor. *Nat Commun* **10**, 4473 (2019).
48. Plesa, C. *et al.* Direct observation of DNA knots using a solid-state nanopore. *Nature Nanotech* **11**, 1093–1097 (2016).
49. Steinbock, L. J., Otto, O., Chimere, C., Gornall, J. & Keyser, U. F. Detecting DNA Folding with Nanocapillaries. *Nano Lett.* **10**, 2493–2497 (2010).
50. Tang, Z. *et al.* Surface Modification of Solid-State Nanopores for Sticky-Free Translocation of Single-Stranded DNA. *Small* **10**, 4332–4339 (2014).
51. Cai, S.-L. *et al.* Surface charge modulated aptasensor in a single glass conical nanopore. *Biosensors and Bioelectronics* **71**, 37–43 (2015).
52. Niedzwiecki, D. J., Grazul, J. & Movileanu, L. Single-Molecule Observation of Protein Adsorption onto an Inorganic Surface. *J. Am. Chem. Soc.* **132**, 10816–10822 (2010).
53. Awasthi, S. *et al.* Polymer Coatings to Minimize Protein Adsorption in Solid-State Nanopores. *Small Methods* **4**, 2000177 (2020).

54. Carlsen, A. T., Zahid, O. K., Ruzicka, J. A., Taylor, E. W. & Hall, A. R. Selective Detection and Quantification of Modified DNA with Solid-State Nanopores. *Nano Lett.* **14**, 5488–5492 (2014).
55. Plesa, C. *et al.* Fast Translocation of Proteins through Solid State Nanopores. *Nano Lett.* **13**, 658–663 (2013).
56. Freedman, K. J., Haq, S. R., Edel, J. B., Jemth, P. & Kim, M. J. Single molecule unfolding and stretching of protein domains inside a solid-state nanopore by electric field. *Scientific Reports* **3**, 1638 (2013).
57. Li, J., Fologea, D., Rollings, R. & Ledden, B. Characterization of Protein Unfolding with Solid-state Nanopores. *Protein and Peptide Letters* **21**, 256–265 (2014).
58. Larkin, J., Henley, R. Y., Muthukumar, M., Rosenstein, J. K. & Wanunu, M. High-Bandwidth Protein Analysis Using Solid-State Nanopores. *Biophysical Journal* **106**, 696–704 (2014).
59. Kasianowicz, J. J., Brandin, E., Branton, D. & Deamer, D. W. Characterization of individual polynucleotide molecules using a membrane channel. *Proc. Natl. Acad. Sci. U.S.A.* **93**, 13770–13773 (1996).
60. Freedman, K. J. *et al.* Nanopore sensing at ultra-low concentrations using single-molecule dielectrophoretic trapping. *Nature Communications* **7**, 10217 (2016).

Chapter 2: Evaluation of Conductive Pulse Sensing and Its Mechanisms for Enhanced Molecular Sensing

2.1 Abstract

Nanopore sensing is nearly synonymous with resistive pulse sensing due to the characteristic occlusion of ions during pore occupancy, particularly at high salt concentrations. Contrarily, conductive pulses are observed under low salt conditions wherein electroosmotic flow is significant. Most literature reports counterions as the dominant mechanism of conductive events (a molecule-centric theory). However, the counterion theory does not fit well with conductive events occurring via net neutral-charged protein translocation, prompting further investigation into translocation mechanics. In this chapter, we demonstrate theory and experiments underpinning the translocation mechanism (i.e., electroosmosis or electrophoresis), pulse direction (i.e., conductive or resistive) and shape (e.g., monophasic or biphasic) through fine control of chemical, physical, and electronic parameters. Results from these studies predict strong electroosmosis plays a role in driving DNA and protein events and generating conductive events due to polarization effects (i.e., a pore-centric theory).

2.2 Introduction

Since their first use as a biosensor, solid-state nanopores continue to explore new biophysical phenomena and have cemented their place in history as high-throughput, low-cost overhead, real-time, single-molecule resolution electrical read-out platforms. Although the translocation profiling of biochemically, biomedically, and pharmaceutically

impactful new molecules and particles has gained tremendous traction in laboratories across the world, the high electrolyte concentration paradigm in which experiments are performed has been rather unchanged since the sensing inception of nanopores in 1996¹. The attractiveness associated with high electrolyte solutions is largely due to the high signal-to-noise ratio (SNR), high electrophoretic throughput, and reliable generation of resistive pulses stemming from DNA transiently blocking ions (typically potassium and chloride). The physical principles in which DNA modulates the flow of ionic current within a nanopore have been studied extensively²⁻⁴. Although nanopore sensing is mostly associated with resistive pulse sensing due to transient ionic current perturbation by the molecule, the resistive nature of events is not consistent across all DNA translocation experiments^{1,5,6}. In 2004, Chang et. al., reported on current-enhancing events at low electrolyte concentrations wherein the DNA-occupied pore conducted more ions compared to the DNA-free pore⁷. Therefore, pulses generated through translocations can be categorized as either current-reducing (i.e., resistive event, RE), or current-enhancing (i.e., conductive event: CE).

As electrolyte concentration decreases, CEs are often observed in both planar membrane nanopores as well as conical nanopipettes, suggesting that CEs are not pore geometry specific⁸⁻¹⁶. It is also at this regime where electroosmotic flow (EOF) strengthens, sometimes leading to the translocation of molecules opposing electrophoretic flow (EPF). Although EOF and CEs often coincide, it is important to note that they are not mechanistically linked. For example, CEs are seen in nanopores where EOF is reduced to allow EPF-driven events⁹. Despite the large number of experiments describing CEs, the

origins of CEs in the presence of low ionic strength have been elusive. The leading consensus is that the combination of additional counterions and frictional effects influence the production of CEs³. Specifically, CEs stem from the introduction of additional counterions by the charged DNA (i.e. K^+) within the nanopore is greater than the number of ions within the DNA-free pore⁷. Once electrolyte concentration decreases below ~ 0.02 M, mostly counterions are present within the pore, which explains the current enhancement^{17,18}. Interestingly, at ~ 0.4 M, counterions are thought to precisely compensate for the DNA-occupied regions of the pore and yields no current modulation¹⁹.

The results presented in this chapter conflict with the conventional consensus and may be better explained by another potential theory; namely that current enhancement is due to a flux imbalance which causes (1) charge density polarization and (2) voltage changes at the pore (V_{pore}). Indeed, the first report of nanopore sensing at asymmetric salt conditions suggested that V_{pore} may be reduced and was used as an explanation for slower DNA translocations²⁰. Perhaps the most convincing evidence presented here for the need of a new model lies with the fact that conductive events are observed for proteins at both symmetric low salt conditions and asymmetric high salt conditions. The heterogeneous surface charge of proteins would mean that counterions would be of mixed valency (+e, -e). Even if positive counterions were more prevalent on the surface of the protein, we would expect the current enhancement to be minimal. Instead, we found that the current enhancement is greater than that of DNA. The flux imbalance theory presented here does not depend on the analyte at all but rather is modeled using the steady state flux of ions through pore.

Asymmetric high salt conditions, explored by Zhang et al, also produced CEs and the authors used a multi-ion model composed of Nernst-Planck and Stokes equations to explain their observations²¹. Namely, EOF enhancement in the space between the DNA and the pore is significantly higher than the ions blocked by DNA occupancy in the pore²¹. Our experimental observations with PEG (a natively neutral polymer that functions as a polycationic polymer through cation adsorption) cannot be explained through this model where CEs were seen with smaller diameter pores (Appendix A, Figure A.S1). Protein (i.e., holo form of human serum transferrin) translocation under a low ionic strength condition, yielded CEs as well (Appendix A, Figure A.S2). Thus, the intriguing question, why does ionic current increase during transient DNA and protein occupancy of a nanopore, remains under-examined and warrants further investigation. Since a cohesive theory for the nature of conducting events is still elusive, we studied the transport of DNA and protein within a nanopipette using various monovalent salts and under symmetric and asymmetric salt conditions.

A second fundamental question that remains debated in the literature is: can low salt conditions promote EOF-driven DNA transport. Although it may seem obvious, electroosmotic dominant transport of DNA is hardly reported (first predicted in 2010²²) and therefore, less known in the nanopore community^{23,24}. On the other hand, electrophoretic transport of DNA through nanopores is a well-reported and almost unanimously used mode of transport. While electroosmosis has seen widespread adoption in protein and glycan characterization, its use in DNA experiments is meager, largely due to the high linear charge density associated with DNA and (high) salt conditions typically

used in experiments^{25,26}. However, tuning of electroosmosis has been used to, for example, promote single file translocation, improve throughput, and tune translocation time^{25,27,28}. To the best of our knowledge, no previous reports exist outlining the electroosmotic DNA transport through nanopipettes. Thus, in this chapter, we characterized EOF-driven events (anti-electrophoretic, or anti-EPF) with Lambda DNA (λ -DNA)—the gold standard of the nanopore community to benchmark new developments due to its well-known physicochemical parameters—using quartz nanopipettes.

In summary of our findings, DNA CEs are extremely cation-, pore size-, and voltage-specific and potentially the result of an imbalance of ionic fluxes and leads to charge density polarization and a violation of net neutrality²⁹. We utilize a Poisson-Nernst-Planck (PNP) model to describe the flux imbalance between cation and anions within a nanopore which differs from the more traditional Nernst-Planck (NP) equations in how electro-neutrality and charge conservation is formulated. The PNP model more accurately describes the boundary layers (1-10 nm) at electrodes and charged surfaces³⁰. For nanopores that are on the same order of magnitude as the boundary layers, the PNP equations are a more complete treatment of charged species transport. The net effect is that flux imbalances have the ability to change the space charge density and the voltage throughout the fluidic system. We will discuss the electrokinetic and hydrodynamic phenomena that affect event shapes such as counterion cloud, ion mobility, pore size, and electrolyte composition. This section elucidates some of the fundamental pre-requisites for observing CEs when DNA translocates through a nanopore and paves the way for harnessing CE mechanisms for molecular carrier detection and characterization.

2.3 Results and Discussion

While most nanopore-based, single-molecule sensing is performed using planar membranes, which have a well-defined pore length (i.e. effective membrane thickness), nanopipettes have a gradual taper length (Figure 2.1a) that increases the sensing region of the device³¹. We fabricated nanopipettes by laser pulling glass nanocapillaries, producing two identical quartz nanopores (see Methods for fabrication details). With this technique, <10 nm inner pore diameters can be achieved as shown in Figure 1a. This process is fast, inexpensive, and does not require a clean-room environment³². The pore conductance (G) was evaluated using the linear slope of a current-voltage (I-V) curve (Figure 2.1b) and thereafter used to estimate the size of the aperture using^{33,34}:

$$d_i = \frac{4Gl}{\pi K d_b} \quad (1)$$

where l is the length of the conical pore (taper length), K is the measured conductivity of the buffer, and d_b is the diameter of the capillary (0.7 mm) at the beginning of the conical taper. The taper length was measured using an optical microscope. The G , measured by calculating the slope of the linear portion at the negative voltages, varied between 0.6 and 5.4 nS and the I-V curve showed ionic current rectification which is consistent with the previous reports³⁵. The tabulated G values yield pore diameters between 5 (± 0.5) and 48 (± 4) nm, respectively. The pore sizes were also occasionally confirmed using transmission electron microscopy (see Figure A.S3 in Appendix A).

2.3.1 λ -DNA Translocation in Symmetric Low Salt Conditions

After retrieving the I-V information, translocation experiments with λ -DNA at a final concentration of 500 pM were performed in 10 mM Tris-EDTA buffered at pH \sim 7.4. We opted for very a low salt concentration (i.e., 10 mM) to maximize the EOF while maintaining a high enough SNR for pulse extraction (see discussion Appendix A for more details on SNR). The pH was maintained at the physiological pH which renders the glass to be negatively charged (\approx -(10-20) mC/m²)³⁶ and therefore EOF and EPF to be opposing in the case of λ -DNA. For electroosmotic capture to take place, it should outweigh the electrophoretic force (provided the two are opposing rather than complementing) exerted on the DNA molecule by the applied voltage. For a molecule to translocate, it must first diffuse to the capture zone, drift to the pore opening and overcome electrostatic and free energy barriers (e.g., entropy). The shape and extent of the capture volume are exceedingly crucial as they would govern the transport dynamics of the device. It is known, when EPF dominates, the capture volume outside the nanopore assumes a nearly spherical shape surrounding the pore's orifice^{20,37-40}. EOF, on the other hand, depends on the fluid flow profiles. According to the EOF streamlines, the capture volume adopts a shape confined along the sides of the pore⁴¹. There also lies a crossover concentration point in which EOF reverses direction, where EOF is generated along the glass surface and radiates away from the pore aperture⁴¹. Finite element analysis was performed to determine the fluid flow rate at different voltages (Figure 2.1c). Herein, we adopted the operational configuration where the anode electrode is placed inside the pipette side and grounded electrode in the bath (under low salt conditions). Since the glass surface is negatively charged at the operational

pH, at negative applied voltages, the resultant fluid flow would be towards the taper region (i.e., from the bath to the tip). At positive biases, the fluid flow direction switches. In brevity, the simulation depicted in Figure 2.1c was carried out in the following manner: Poisson-Nernst-Planck-Stokes equations were solved simultaneously to account for ionic species spatial concentrations, electrostatic forces on ions and convective forces on ions. EOF was imposed as a force on the surrounding liquid by integrating the spatial accumulation of ions into a volume force that acts on the liquid (boundary conditions can be found and simulations details can be found in Appendix A.S5). The fluid velocity acts as a moving frame of reference for the DNA and can be compared directly with the electrophoretic drift velocity imposed by the electric field. Electrophoretic drift velocity was calculated by extracting the electric field and multiplying by the electrophoretic mobility of DNA ($\mu=3.2 \times 10^4$ cm/Vs)⁴². Simulated results shown in Figure 1c indicate, under low ionic strength conditions, the EOF velocity is greater than the EPF drift velocity rendering the net velocity to be in the same direction as the EOF profile.

Given the inherent differences associated with capture volume shapes associated with EOF and EPF dominant mechanisms, the next step was to elucidate the entrance trajectory of DNA. To do this, λ -DNA was added to the bath and a negative voltage bias was applied to the other electrode to ensure if translocations were to happen (i.e., from the bath to the tip side; forward translocation direction), it would be caused by electroosmosis rather than by the conventional electrophoresis. The fluid flow profiles around pore-tip were simulated to further understand the EOF-driven capture of DNA. The simulated results are shown in Figure 1d and indicate DNA proceeds to diffuse around the solution

until it enters the EOF capture volume, where it is then transported through the pore. To reiterate, this transport is fundamentally possible when the EOF velocity is greater than the EPF drift velocity. Since DNA events occur anti-EPF, mapping the fluid motion is indicative of the capture zone. To experimentally validate the finite element analysis

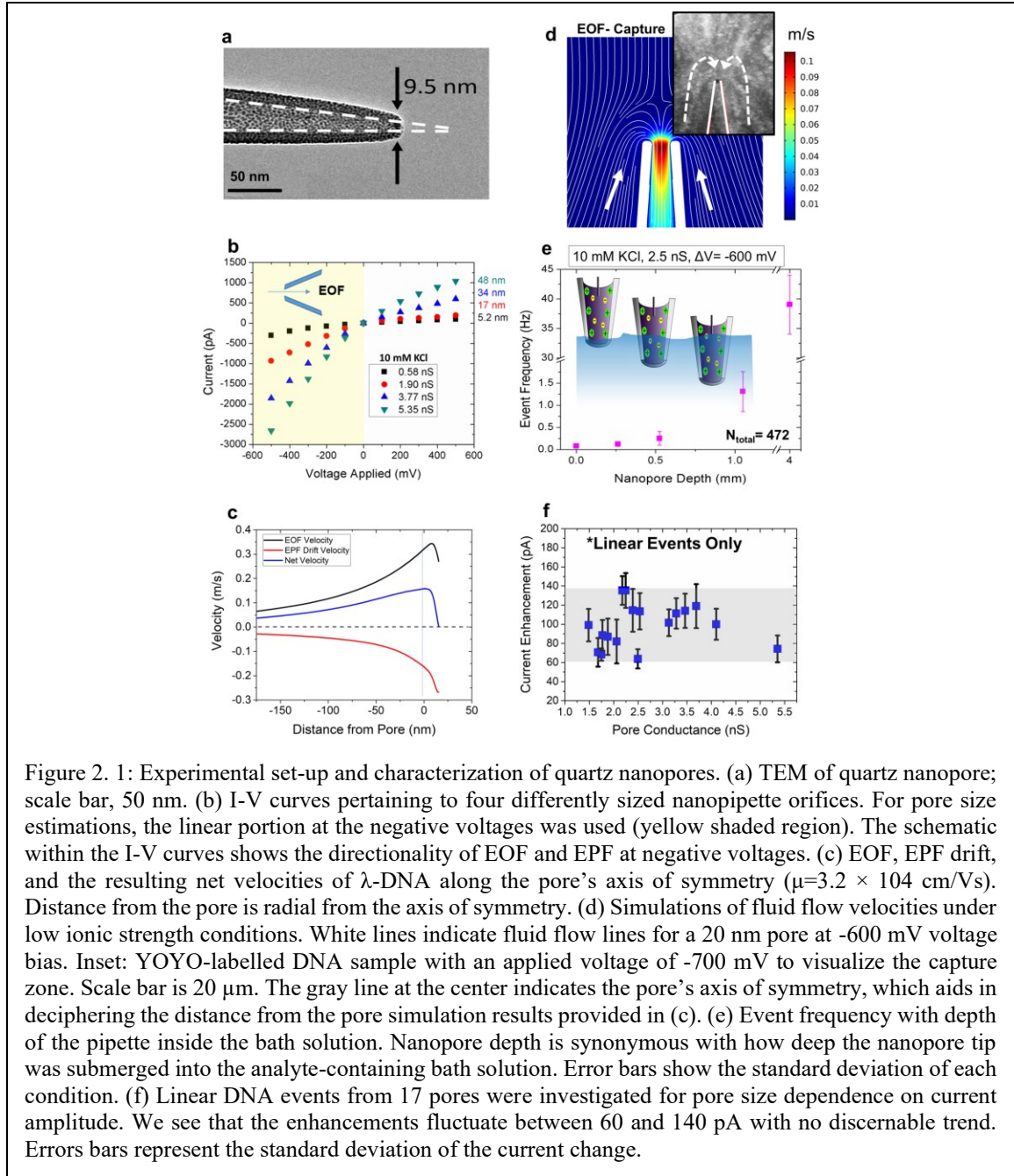


Figure 2. 1: Experimental set-up and characterization of quartz nanopores. (a) TEM of quartz nanopore; scale bar, 50 nm. (b) I-V curves pertaining to four differently sized nanopipette orifices. For pore size estimations, the linear portion at the negative voltages was used (yellow shaded region). The schematic within the I-V curves shows the directionality of EOF and EPF at negative voltages. (c) EOF, EPF drift, and the resulting net velocities of λ -DNA along the pore's axis of symmetry ($\mu = 3.2 \times 10^4$ cm/Vs). Distance from the pore is radial from the axis of symmetry. (d) Simulations of fluid flow velocities under low ionic strength conditions. White lines indicate fluid flow lines for a 20 nm pore at -600 mV voltage bias. Inset: YOYO-labelled DNA sample with an applied voltage of -700 mV to visualize the capture zone. Scale bar is 20 μ m. The gray line at the center indicates the pore's axis of symmetry, which aids in deciphering the distance from the pore simulation results provided in (c). (e) Event frequency with depth of the pipette inside the bath solution. Nanopore depth is synonymous with how deep the nanopore tip was submerged into the analyte-containing bath solution. Error bars show the standard deviation of each condition. (f) Linear DNA events from 17 pores were investigated for pore size dependence on current amplitude. We see that the enhancements fluctuate between 60 and 140 pA with no discernable trend. Errors bars represent the standard deviation of the current change.

(Figure 1d), λ -DNA was tagged with YOYO-1 and the nanopipette tip placed in the focal plane of a water immersion objective (Nikon, NA=1.2). A stacked time series of images (acquired from a Princeton Instruments ProEM emCCD) allowed us to observe λ -DNA capture at -700 mV (Figure 2.1d inset reveals that fluid motion along the sides of the pore is responsible for λ -DNA translocation).

Under high salt conditions, DNA transport has been categorized to adopt a range of configurations including linear, looped, partially folded, and knotted: reported with both planar nanopores^{43–46} and nanocapillaries³³. However, reports on the DNA conformations under EOF dominant transport are yet to be published. Thus, after confirming the mode of dominant transport, we looked at the conformations adopted by translocating DNA molecules. Realizing that the capture volume in EOF-driven translocations surrounds the outer walls of the nanopipette, we first optimized the throughput of the device by adjusting the pipette position with respect to the bath liquid surface as shown in Figure 2.1e. The capture volume can be controlled by submerging varying lengths of the taper length inside the salt solution containing λ -DNA. The nanopore was suspended at 0, 0.26, 0.53, 1.1, and 4.0 mm below the electrolyte solution surface containing λ -DNA. For exact measurements, the nanopore was suspended from a linear stage actuator. Translocations were obtained for voltages between -100 and -1000 mV, in increments of 100 mV. Recording at -600 mV yielded the most consistent translocations without clogging the pore. Events were recorded at -600 mV and the I-V relationship yielded a 2.5 nS pore. The capture rate was calculated at each depth (see Appendix A Section 6 for capture rate calculation details). As nanopore depth increases, capture volume also increases, leading to higher event frequency with

larger depth values. As more of the nanopore is exposed to the λ -DNA solution, the capture volume enlarges, leading to an increase in event frequency and corroborates the EOF capture mechanism more strongly than the electrophoretic capture mechanism. Finally, using a custom-coded MATLAB script, translocation conformations of DNA were examined which revealed that DNA adopts the widely seen conformations: linear, partially folded, and fully folded (see Appendix A Section 7 for further details). By solely selecting linear events, we were able to evaluate the relationship between CE amplitude and pore size; a relationship that may be hidden by multiple conformations of DNA. As seen in Figure 2.1f, no observable trends were seen in CE amplitude with pore conductance (a proxy for pore size).

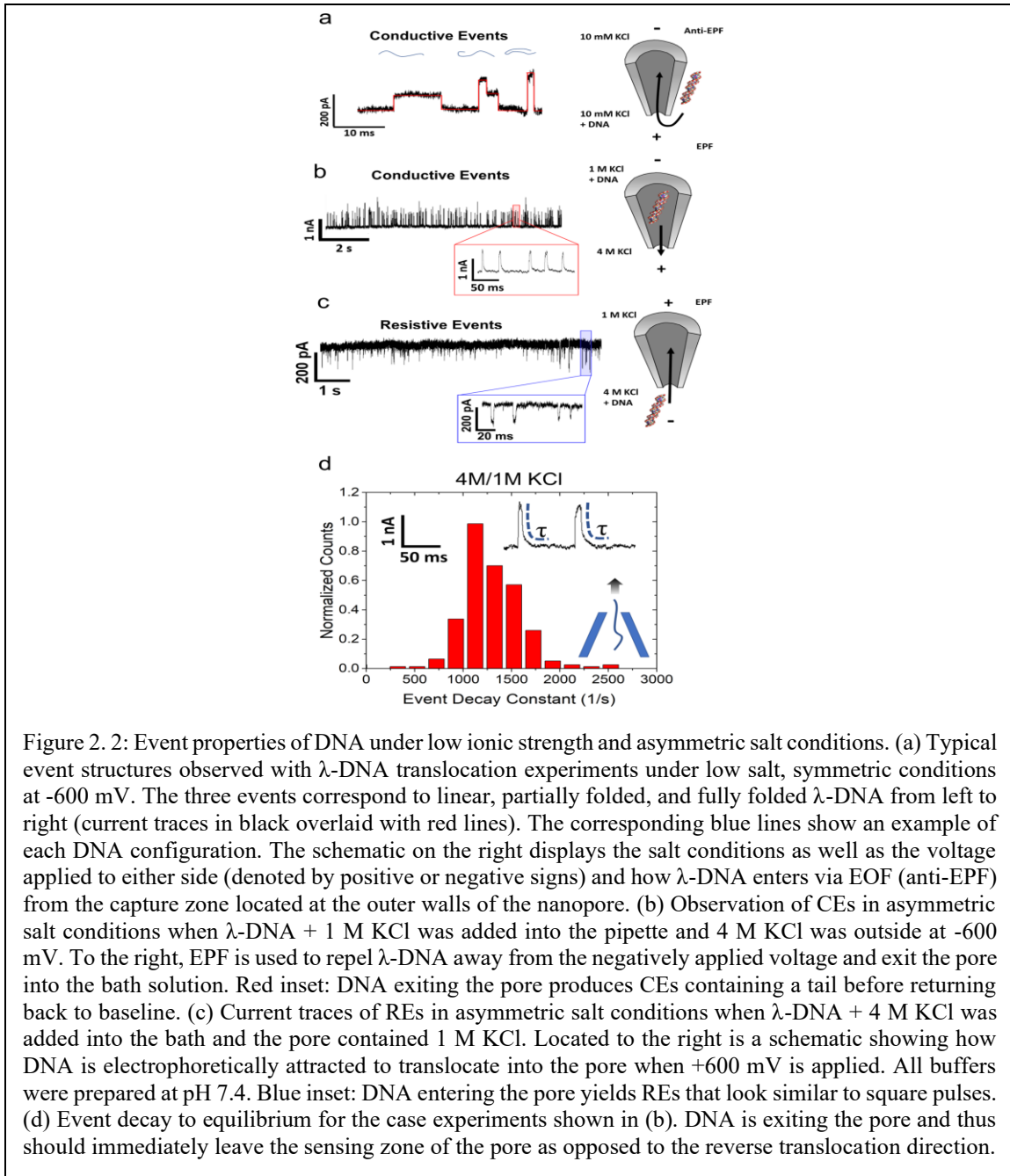
2.3.2 λ -DNA Translocation in Asymmetric High Salt Conditions

Simulations performed in 2009 predicted that current enhancements could be seen at high ionic strength conditions⁴⁷ with small pore diameters (<2.2 nm) using hairpin DNA. In acknowledgment of that finding, we also show that CE phenomenon is not limited to low ionic strength conditions. We employed the usage of salt concentration gradients where the pipette was filled with 1 M KCl and the bath was filled with 4 M KCl. λ -DNA was either added to the pipette (Figure 2.2b: case I) or bath (Figure 2.2c: case II) and a voltage bias consistent with the conventional EPF-dominated transport was applied to the pipette. Note that EOF is deemed negligible under the high salt conditions that these experiments operate. In case I, with an applied voltage of -600 mV, λ -DNA was driven outside the pore through EPF, resulting in CEs. This contradicts the conventional expectation of REs under high salt conditions and CEs under low salt conditions. On the contrary, in case II, with an

applied voltage of +600 mV, λ -DNA was driven into the pipette resulting in REs. Although directional dependence of DNA transport has been reported previously with nanopipettes⁴⁸, a change in the direction of the pulses has not been previously observed. The conductive pulse observations shown here showcase the shortcomings of theory used for nearly two decades which presume excess charge introduced by DNA compensates for the ionic current blockade by DNA to eventually yield conductive pulses. Furthermore, with asymmetric salt conditions (1 M inside, 4 M outside), both the forward and reverse translocations produced unconventional event shapes. It is well known that the translocation direction of a particle is reflected through its event shape with tapered pore geometries unlike their cylindrical counterparts⁴⁹. Moreover, shapes analogous to that shown in Figure 2.2b are typically observed for reverse translocations (i.e., when a molecule enters the pipette through the bath and travels along the confined tapered region). In other words, the geometry of the pore determines the electric field profile and by extension the sensing zone of the pore. Despite the DNA exiting the pore, there is a transient decay back to the baseline current level (Figure 2.2b). Conversely, reverse translocations produced a square pulse rather than a pulse with a decaying tail (Figure 2.2c). Figure 2.2b red inset and 2.2c blue inset provide examples of unconventional shapes seen under their respective conditions. By fitting the current to an exponential decay, the decay constant of forward translocations was found to be approximately $1150 \pm 243 \text{ s}^{-1}$ which corresponds to a 10% to 90% rise time of $\sim 1.2 \text{ ms}$. This is substantially longer than the rise time associated with the 10 kHz lowpass filter used while recording the data ($\sim 33 \text{ }\mu\text{s}$)⁵⁰. Although it is not clear as to what produces the observed waveform shapes, we

speculate ion flux imbalance, its direction, and DNA translocation direction, to play a key role in the mechanism.

Conceptually, a pore can become ion-selective depending on its surface charge. If the pore is charge neutral, it would not exhibit any selectivity whereas if it is negatively



charged, the pore would be cation-selective (Figure 2.3a). Simulations with a negatively charged pore submerged in 10 mM KCl solution showed that although the pore's total ionic flux was not altered significantly by EOF (K^+ flux increased and Cl^- flux decreased by the same amount), it does significantly impact the flux imbalance between cation and anion (see Appendix A Section 8 for simulation details). The terms EOF- and EPF- pumping are used here to signify that ions are being moved by the insertion of electrical energy and energy is required to maintain the system in that state. Flux imbalance, defined here as $|K^+$ flux| minus $|Cl^-$ flux|, can be generated through externally applied conditions and parameters; for example, flux imbalance increases with both the pore diameter and the applied voltage (Appendix A Figure A.S11). This finding will be important when discussing other monovalent salts wherein transitions between REs and CEs occur. Nevertheless, the finding that EOF can increase the counterion (K^+) flux imbalance is particularly noteworthy since (i) CEs were observed at high asymmetric salt conditions which would also cause ionic flux imbalance and (ii) further supports the previous experimental observations of CEs occurring under asymmetric salt conditions as DNA translocates through the pore²¹. With a salt gradient, in addition to the electrical potential gradient, ions could move as result of the chemical potential gradient. Thus, for the asymmetric salt cases, assuming the same spatial voltage distribution, one ion will outweigh the flux of the oppositely charged ion, as shown in Figure 2.3c. Note that 10 mM/10 mM conditions are also cation selective at all voltages and is shown in Appendix A Section 5. In case I, K^+ moves along both the electrical and chemical potential gradients opposing the DNA translocation direction whereas in case II, due to the positive bias, Cl^-

ions move along both the gradients cooperative with DNA translocation direction. This is also reflected through the translocation time (Δt) where case I produced events that were $\sim 3\times$ slower compared to case II (Δt were 3.2 ms and 1.1 ms respectively for case I and case II). Taken together, these results imply a flux imbalance in favor of Cl^- produces REs whereas CEs stem from a flux imbalance in favor of K^+ . This is notably different than ion selectivity which is typically a characteristic of the pore itself. Rather, flux imbalances can be generated through externally applied conditions and parameters. This computational finding further supports the previous experimental observations of CEs occurring under asymmetric salt conditions as DNA translocate the pore.

The impact of the flux imbalance seems to play a role in redistributing the voltage drop inside the nanopipette; in particular, the taper region where there is a confining negative surface. Using finite-element simulations, and varying the surface charge density incrementally, it is shown that higher surface charges lead to two main effects. First, EOF flow velocity increases, and secondly, the excess charge inside the taper length of the pipette causes ion polarization effects. For example, as surface charge is increased, the electric potential drops significantly between -100 and -400 nm inside the nanopipette (Figure 2.3d). Under asymmetric salt conditions, the impact is also voltage dependent since both EOF and EPF are voltage regulated; both producing a flux imbalance. Under positive voltages, the Cl^- is rejected from the pore to the tapered region decreasing the voltage drop occurring inside the taper of the nanopipette. That is, as seen in Figure 2.3, compared to a neutral pore surface, the tapered region becomes more conductive (i.e., less voltage drop occurs). On the other hand, if a negative bias is applied inside the pore, K^+ ions are

accepted to the pore interior causing the voltage drop inside the taper to increase compared to a neutral pore since the tapered region becomes more resistive (i.e., larger voltage drop compared to a neutral pore). Thus, the net positive or net negative charges stored inside the pipette change the voltage distribution and therefore the sensing zone of the nanopipette sensor. The decrease in charge storage at low salt is observed in Figure 2.3e wherein there is always a positive charge accumulation, but it is lessened or exacerbated by EOF. While EOF is the mechanism of charge transport, it is the flux imbalance that ultimately determines the degree of polarization. While charge density polarization effects are commonly taken into account on electrode-electrolyte interfaces, it seems rarely considered for nanoscale confinements until relatively recently^{51,52}.

2.3.3 Alkali Chloride Dependence on Event Characteristics

Now that a relationship between the ion flux imbalance and pulse direction is apparent, the question of whether the nature of the monovalent cation would have any effect on the transport properties was examined. For example, LiCl is known to shield the charge of DNA and slow it down compared to KCl since the former can bind more covalently to charged moieties compared to the latter⁵³. Additionally, LiCl had a

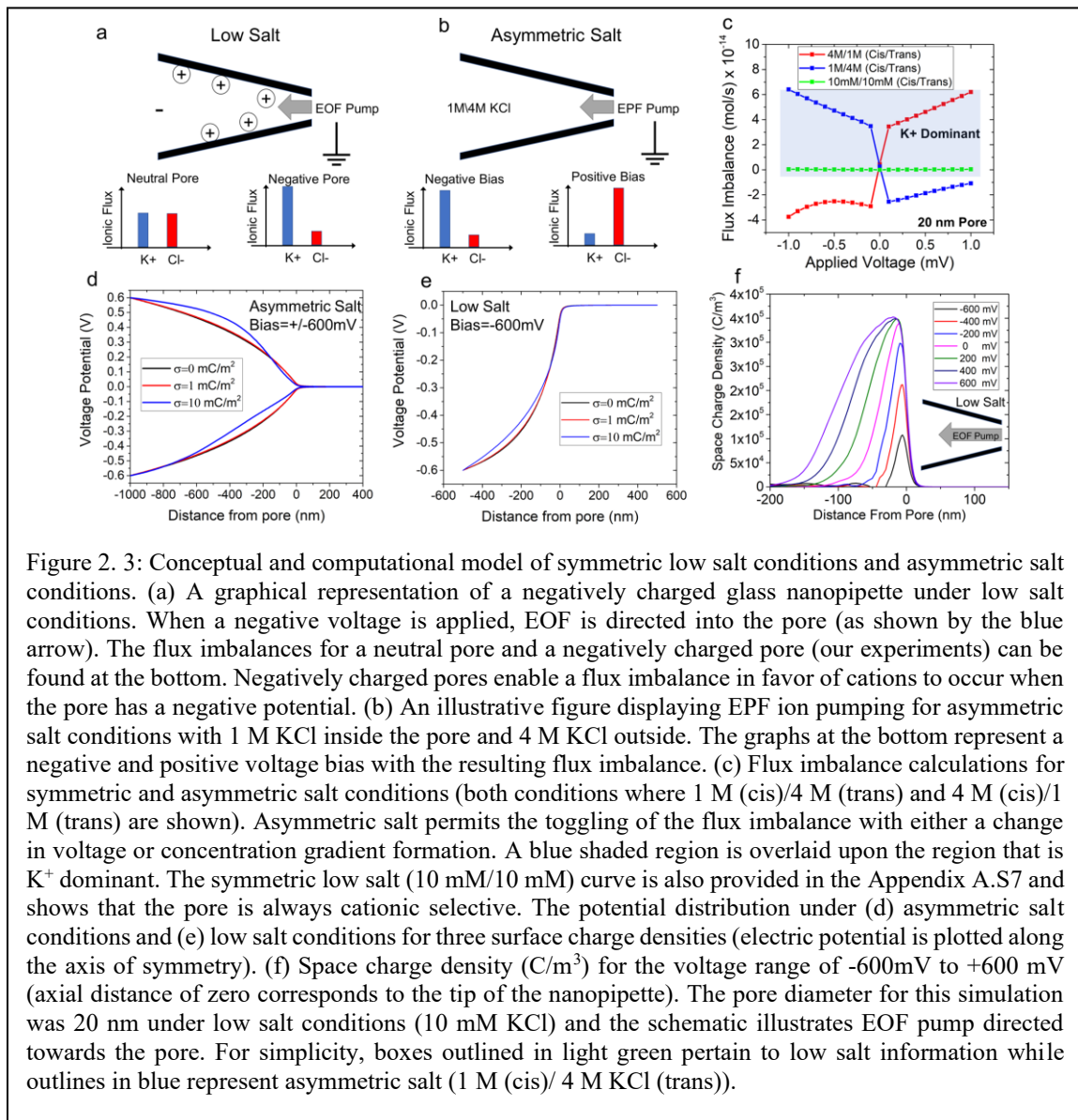


Figure 2. 3: Conceptual and computational model of symmetric low salt conditions and asymmetric salt conditions. (a) A graphical representation of a negatively charged glass nanopipette under low salt conditions. When a negative voltage is applied, EOF is directed into the pore (as shown by the blue arrow). The flux imbalances for a neutral pore and a negatively charged pore (our experiments) can be found at the bottom. Negatively charged pores enable a flux imbalance in favor of cations to occur when the pore has a negative potential. (b) An illustrative figure displaying EPF ion pumping for asymmetric salt conditions with 1 M KCl inside the pore and 4 M KCl outside. The graphs at the bottom represent a negative and positive voltage bias with the resulting flux imbalance. (c) Flux imbalance calculations for symmetric and asymmetric salt conditions (both conditions where 1 M (cis)/4 M (trans) and 4 M (cis)/1 M (trans) are shown). Asymmetric salt permits the toggling of the flux imbalance with either a change in voltage or concentration gradient formation. A blue shaded region is overlaid upon the region that is K^+ dominant. The symmetric low salt (10 mM/10 mM) curve is also provided in the Appendix A.S7 and shows that the pore is always cationic selective. The potential distribution under (d) asymmetric salt conditions and (e) low salt conditions for three surface charge densities (electric potential is plotted along the axis of symmetry). (f) Space charge density (C/m^3) for the voltage range of $-600mV$ to $+600mV$ (axial distance of zero corresponds to the tip of the nanopipette). The pore diameter for this simulation was 20 nm under low salt conditions (10 mM KCl) and the schematic illustrates EOF pump directed towards the pore. For simplicity, boxes outlined in light green pertain to low salt information while outlines in blue represent asymmetric salt (1 M (cis)/ 4 M KCl (trans)).

significantly higher streaming current compared to both KCl and CsCl (see Appendix A Section 9 for more details). In this section, first, we draw comparisons between the translocation properties of λ -DNA in symmetric 10 mM KCl and 10 mM LiCl salts followed by 10 mM CsCl.

The nanopipette containing 10 mM LiCl was inserted inside a solution containing 10 mM LiCl and λ -DNA (buffered at pH~7.4) and current traces were recorded from -300 mV to -900 mV in 200 mV increments (Figure 4a). As seen in Figure 2.4a, a crossover from REs to CEs that is independent of salt concentration was observed. At voltages of -300 and -500 mV, λ -DNA translocations resulted in REs and at voltages of -700 and -900 mV, it resulted in CEs (also see Figure 2.4c). Intrigued by this observation, we explored the pulse behavior at -600 mV where the event current shape assumed both a resistive and conductive region resembling a biphasic waveform (Appendix A Figure A.S13). The biphasic nature of the events at the transitional voltages (-500, -600, and -700 mV) suggests that both resistive and conductive modulation mechanisms can conjointly act and perhaps act at different timescales in relation to the translocation event. For example, in the moments before or after the DNA enters the pore, DNA would still exist within the EOF flow field of the pore leading to current modulations on a potentially longer timescale.

Another comparison was done using two nanopipettes with inner diameters of 33 ± 3 nm. One nanopipette contained 10 mM KCl while the other contained 10 mM LiCl. Both were submerged in 10 mM LiCl with 500 pM λ -DNA (all buffered at pH ~7.4). Interestingly, at -600 mV, CEs were observed for the pore containing KCl whereas REs were observed for LiCl (Figure 2.4e). At -600 mV, finite element simulations (for the $33 \pm$

3 nm nanopipette) predicted that the nanopipette is strongly cation-selective in KCl and weakly cation-selective in LiCl, which may be a possible explanation for the event types observed. If the transition to CE occurs at a flux imbalance of 2×10^{-16} mol/s as shown in Figure 2.4c, the same discriminating line appears to be valid for predicting KCl and LiCl current modulation (Figure 2.4e). The stronger flux imbalance observed with KCl (under the same pore size, voltage, and salt concentration) led to CEs while LiCl produced REs (Figure 2.4d-e). The critical value of the flux imbalance has no clear meaning at this time but is extracted from a combination of experimental and numerical approaches.

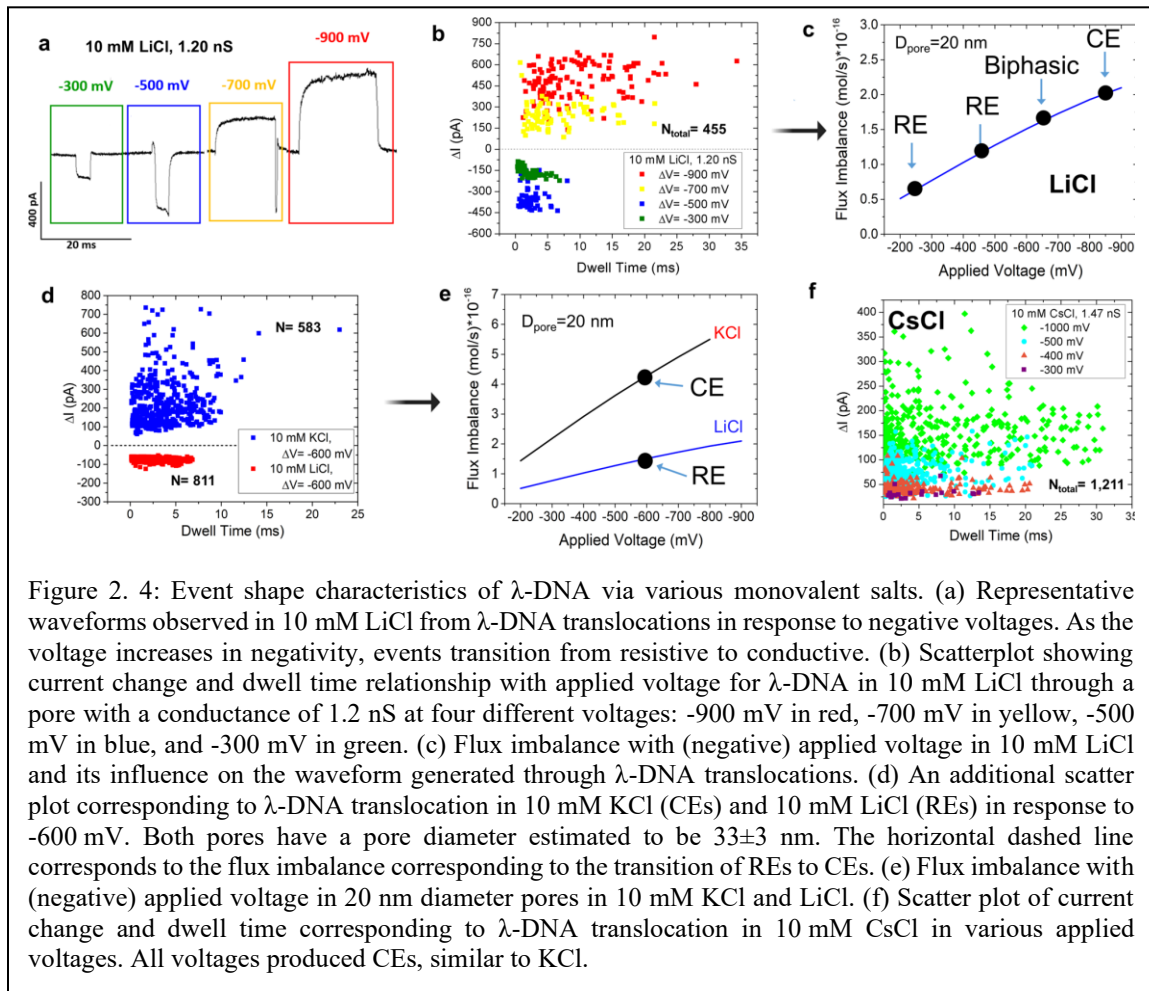
Interestingly, KCl had longer event durations at these low salt conditions (3.1 ± 1.5 ms compared to 1.9 ± 0.7 ms in LiCl): a counterintuitive observation if DNA was electrophoretically driven since LiCl is known to slowdown DNA translocation through charge shielding compared to KCl⁵³. Since translocations in both KCl and LiCl are EOF driven, we suspect the effective charge shielding ability of LiCl allows EOF to transport the DNA with less opposing force. Other than the differences in Δt , as seen in Figure 2.4d, the ΔI of REs observed for LiCl are much more tightly clustered together compared to ΔI of CEs observed with KCl (-70 ± 8 pA versus 200 ± 122 pA, respectively). The source of the variability of CEs observed in KCl is still not fully understood and requires further investigation. Once LiCl events transition to become CEs (Figure 2.4b), current modulations become more scattered compared to REs. Additional information from λ -DNA translocating in 10 mM LiCl can be seen in Appendix A Section 10.

Recently, CsCl was shown to have an advantage over KCl in respect to sequencing using solid-state nanopores¹¹. This publication used CsCl because it disrupts the hydrogen

bonding between guanines, therefore denaturing the G-quadruplex into single-stranded structures. Although we are not working with ssDNA, we aimed to compare KCl event properties with another alkali metal chloride that holds promise in the nanopore community. Therefore, we performed experiments using nanopipettes filled with 10 mM CsCl inserted into 10 mM CsCl with λ -DNA (Figure 2.4f). Similar to KCl, pulse direction in CsCl is expected to be voltage independent since K^+ and Cs^+ have nearly the same diffusion coefficient⁵⁴. To confirm this, a pore with a conductance of 1.5 nS (14 ± 2 nm diameter) was used under low ionic strength conditions and voltages of -300 mV, -400 mV, -500 mV, and -1000 mV were applied. All voltages resulted in CEs. To further strengthen this observation, flux imbalance for CsCl was simulated (Appendix A Section 11) which revealed the pore to be cation-selective across the experimentally viable voltage range. Simulated results of KCl and CsCl were nearly identical due to nearly identical diffusion coefficients for K^+ and Cs^+ (2.02×10^{-5} and 2.00×10^{-5} cm²/s, respectively⁵⁴).

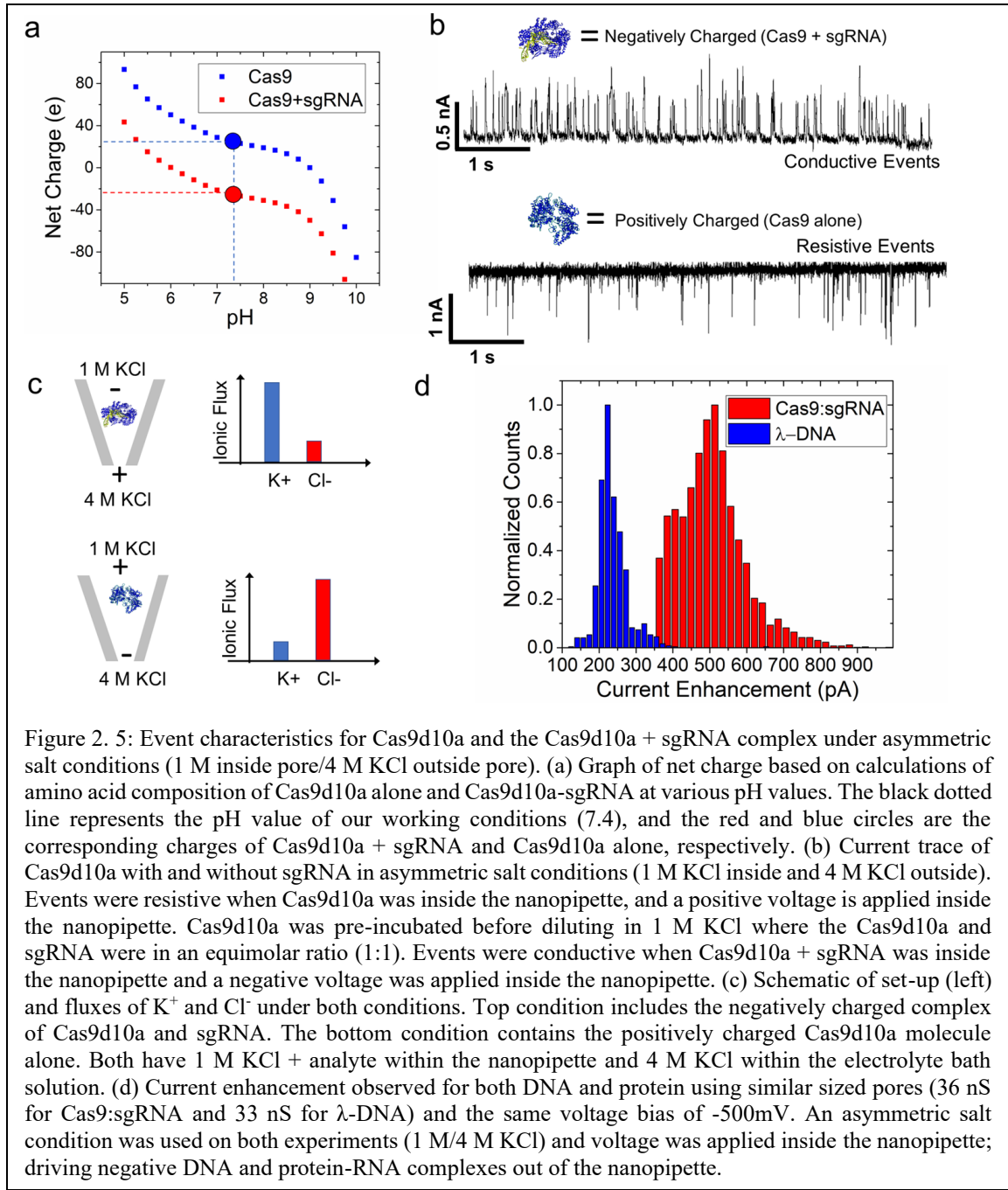
2.3.4 Protein Conductive Events at Asymmetric Salt Conditions

According to the experimental and numerical evidence, flux imbalance seems to play a role in producing CEs. Using the asymmetric salt conditions, we showed that a flux imbalance can be generated that favors potassium ions (i.e., case I). A reversed voltage polarity would therefore generate a flux imbalance that favors chloride ions (i.e., case II). We further wanted to investigate whether this would hold for protein structures since they notably have a heterogeneously charged surface. If analyte counterions played a role in CEs, we would expect cation and anion counterions would cancel out and there would be



no observation of CEs. To study this, we chose to study the Cas9 mutant, Cas9d10a, because unbound it carries a net positive charge at pH \sim 7.4, and once bound to sgRNA, the complex becomes negatively charged⁵⁵. This protein would also serve as a proxy for detecting trypsin in future studies. For added specificity, amino acid sequence calculations were performed on the Cas9d10a complex alone and bound to sgRNA, providing net charges of both (Figure 2.4a). The pH was not changed to be consistent with the previous set of experiments (e.g., same charge density on the pore and thus similar EOF). Furthermore, the same asymmetric salt conditions were employed, as before, where 1 M KCl was inside the nanopipette and 4 M KCl was outside the nanopipette. The Cas9d10a protein was added inside the nanopipette (in 1 M KCl) with and without sgRNA (resulting current traces are shown in Figure 2.5b and 2.5c, respectively). The Cas9d10a-sgRNA complex was achieved by incubating Cas9d10a with sgRNA (equimolar amounts) for 1 hour at room temperature. Voltages were applied to be consistent with the expected electrophoretic transport directions: positive bias for the Cas9d10a + sgRNA complex and a negative bias for the Cas9d10a protein. Like λ -DNA, Cas9d10a + sgRNA complex produced CEs (Figure 2.5b). Under this condition, K^+ from the outside (4 M KCl) is driven into the pipette. However, upon reversing the voltage, the pore's flux imbalance was in favor of Cl^- and thus Cas9d10a produced REs. In this condition, Cl^- from the outside (4 M KCl) is driven into the pipette (referred to previously as EPF pumping of ions). The events at positive voltage could indeed be from either Cas9d10a + sgRNA complex or sgRNA alone since both are negatively charged. However, Cas9d10a binding of sgRNA is typically fast with slowly reversible reaction kinetics⁵⁶. The pulse direction is consistent with our

previous observations where cation selectivity yielded CEs and anion selectivity yielded REs. It is also noteworthy to discuss the magnitude of the current enhancement between DNA and protein.



2.3.5 Mechanistic Insight into Conductive Events

We have proposed a pore-centric model of CEs that is based on the dynamic distribution of ions inside of the nanopore. Volume exclusion is the typical mechanism of observing REs and we believe volume exclusion is still the main mechanism of CEs as well; both yield a transient ionic perturbation based on molecular occupancy of the pore. Since the voltage at the extreme ends of the fluidic reservoirs is clamped, charge build-up (i.e., potassium) tends to generate a voltage that, in turn, lowers the effective voltage for ion conduction at the pore. Inherent to a system with cation/anion flux imbalances is the concept of net neutrality, which is, by definition, violated by the conditions discussed here. Since electrostatics and ionic concentration profiles are coupled, voltage and ion flow are linked mechanistically. That is, especially with low electrolyte conditions, excess of either ion (cation or anion) could increase or decrease the voltage drop through the tapered region. The model developed for this study avoided the use of classical Nernst-Planck equations which assume net neutrality. Instead, a Poisson-Nernst-Planck (PNP) model was developed which permits ionic modulation of the electrostatic system. In the case of asymmetric salt conditions, the ion flux is also dependent on the chemical potential gradient where ions move from high salt to low salt generating a charge density polarization effect. In asymmetric salt, the pore can even be anion selective, which is not possible under symmetric conditions. Depending on the voltage bias, the pore is either cation selective or anion selective, which changes the voltage drop in the tapered region and the pore. For low salt conditions, the pore is always cation selective since the quartz surface has a negative surface charge. The magnitude of the EOF is the critical factor that influences the current

enhancement. For example, LiCl has less EOF (both in terms of average velocity and volumetric flow) in comparison to KCl and a transition to conductive events occurs at higher voltage (higher EOF). We speculate that a DNA-occupied pore transiently stops EOF (i.e., the effective pore size decrease during DNA occupation which would result in diminished EOF) effectively lowering the charge stored inside the pore. Finite element methods demonstrate the accumulation of charge inside the glass pore (Figure 2.3). The increase in stored charge with applied voltage is a characteristic trait of an ionic capacitor⁵⁷. We believe that charge storage and dissipation dynamically impact the voltage at the pore therefore indirectly measures the occupancy of the molecule inside the pore.

An assumption used in the flux imbalance theory presented here is that occupancy of the DNA or protein leads to less polarization through disturbing the equilibrium conditions of the open-pore. For nanopore conditions in which a flux imbalance is created by convective flow, it is easy to see how a translocating entity can block fluid flow. For asymmetric salt conditions, the role of osmotic flow and its role in generating a flux imbalance is an important area that needs exploration. Nevertheless, even for conditions with no fluid flow, the mere reduction of ionic flow (equal reduction of K^+ flux and Cl^- flux) may reduce the polarization of the nanopore. Based on the decay rate of events (Figure 2.2), it seems that polarization is in dynamic equilibrium and, furthermore, associated with a time constant. A second point to consider is the role of nanopore geometry. Based on the asymmetric salt conditions that were studied, a K^+ flux imbalance into the nanopipette seems to yield the greatest polarization effect that led to a greater current enhancement for DNA translocation. K^+ flux out of the nanopipette did not achieve the same level current

enhancement Upon DNA entering the pore. The rationale that positive charge can be stored in the negative taper length of the nanopipette is used to explain the high current enhancements at this condition: 1 M + DNA inside the pipette, 4 M outside.

2.4 Conclusion

Ionic-generated potentials are typically named according to the principle in which they are generated. For example, diffusion potentials, streaming potentials, and exclusion potentials⁵⁸. Nevertheless, charge separation is a commonality of these potentials as well as our capacitor model which ultimately could generate voltage and current transients. Data thus far support the hypothesis that a flux imbalance plays an important role in the generation of CEs and the evidence here demonstrates the importance of the pore's charged surface, voltage-bias, and associated electro-hydrodynamics in generating CEs. In this study, we described multiple electro-hydrodynamic effects that influence EOF-driven DNA translocations under low ionic strength conditions. We have found that EOF can be used in various alkali chlorides. Confirmation that EOF capture volume resides along the sides of the tip aperture and directs flow inward has been shown. The resulting current enhancement or reduction dependence on pore size can be explained by a pore's flux imbalance. Secondly, we discovered a pulse crossover point from CEs to REs, independent of salt concentration and specific to LiCl, by scanning the applied voltage from -300 mV to -900 mV. We show that changing the electrolyte influences the event shape, SNR values, and event frequency, which is highly regarded information that can be utilized for the detection of other biomolecules. The pulse nature was also explored for proteins with Cas9 mutant, Cas9d10a, in both free form and bound to sgRNA wherein CEs were observed for

the Cas9d10a- sgRNA complex and REs were observed for the free Cas9d10a protein. The pulse direction results were in good agreement with the flux imbalance theory proposed for DNA. With this, we have detected both DNA and protein by modulating the ionic flux, providing the framework for detecting the DNA – trypsin complex in future chapters. Evaluating polarization effects and its role in producing CEs will provide a framework for understanding experimental results at these low salt and asymmetric salt conditions. Therefore, we propose an additional possible theory for conductive events based on charge density polarization where accumulation of positive charge (for a negatively charged pore), via a flux imbalance, appears to effectively lower the voltage bias at the pore during open pore conditions and enhances the current when the equilibrium conditions are altered.

2.5 Materials and Methods

2.5.1 Nanopore Preparation

Nanopore fabrication began with quartz capillaries (Sutter Instrument Co.) of 7.5 cm in length, 1.00 mm in outer diameter, and 0.70 mm in inner diameter. Capillaries were plasma cleaned for five minutes before laser-assisted machine pulling to remove any surface contaminations. Afterwards, quartz capillaries were placed within the P-2000 laser puller (Sutter Instrument Co.) and a one-line protocol was used: (1) HEAT: 630; FIL: 4; VEL: 61; DEL: 145; PULL: between 135 and 195. This resulted in two identical, conical nanopores. The heat duration was approximately 4.5 s.

Electrodes were constructed using silver wires dipped in bleach for 30 minutes followed by thorough rinsing with water to remove any residual bleach. Freshly pulled

nanopipettes were then backfilled with either 10 mM KCl (Sigma Aldrich), LiCl (Sigma Aldrich), or CsCl (Alfa Aesar) buffered at pH~7.4 using the Tris-EDTA buffer (Fisher BioReagents). The conductivities of each alkali chloride were recorded using an Accumet AB200 pH/Conductivity Benchtop Meter (Fisher Scientific). The results were as follows: 10 mM KCl= 0.26 S/m, 10 mM LiCl= 0.23 S/m, and 10 mM CsCl= 0.26 S/m at room temperature. An optical microscope was used to inspect the nanopipettes at this stage for any irregularities. Once the nanopipettes had been inspected, electrodes were connected to the head stage of the Axopatch 200B (Molecular Devices).

2.5.2 Data Acquisition

The Axopatch 200B patch-clamp amplifier was used in voltage-clamp mode to measure the ionic current changes. The gain was optimized before each experiment and the signal was filtered with the inbuilt low-pass Bessel filter at 10 kHz and digitized using Digidata 1550B (Molecular Devices). The data was acquired at a frequency of 250 kHz. Data analysis for DNA translocations and folding was performed using a custom MATLAB code.

2.5.3 Finite Elements Methods

COMSOL Multiphysics was used for modeling nanopipette geometries that were based on SEM and TEM images acquired from the same pipette pulling protocols that were used in sensing experiments. A 2D axisymmetric model was employed to reduce the computational resources required. Once the geometries were created in COMSOL, the physics that were utilized included Poisson–Nernst–Planck–Stokes equations: laminar

flow, transport of diluted species, and electrostatics. The electrostatics boundary condition for the glass was set at a surface charge density of $-2 \times 10^{-2} \text{ C/m}^2$. To model electroosmotic flow, a volume force on the fluid was set to the space charge density of the ions in solution multiplied by the electric field vectors (r and z vectors). An in-built EOF boundary condition was also tested and yielded similar results. Diffusion coefficients and mobility values were obtained from Lee et. al.⁵⁴. All models were tested with different solvers, solving conditions, and reservoir sizes to ensure the accuracy of results. The Stokes flow boundary conditions were no-slip, and the inlet and outlet were kept at the same 1 atm of pressure which is consistent with experiments. The z-component of the flux was extracted for each model from a 2D line that spans the width of the pore. The flux was then integrated across this 2D line to obtain the flux in moles/s.

2.6 References

1. Kasianowicz, J. J., Brandin, E., Branton, D. & Deamer, D. W. Characterization of individual polynucleotide molecules using a membrane channel. *Proc. Natl. Acad. Sci. U.S.A.* **93**, 13770–13773 (1996).
2. van Dorp, S., Keyser, U. F., Dekker, N. H., Dekker, C. & Lemay, S. G. Origin of the electrophoretic force on DNA in solid-state nanopores. *Nature Physics* **5**, 347–351 (2009).
3. Kesselheim, S., Müller, W. & Holm, C. Origin of Current Blockades in Nanopore Translocation Experiments. *Phys. Rev. Lett.* **112**, 018101 (2014).
4. Keyser, U. F. *et al.* Direct force measurements on DNA in a solid-state nanopore. *Nature Physics* **2**, 473–477 (2006).
5. Haque, F., Li, J., Wu, H.-C., Liang, X.-J. & Guo, P. Solid-State and Biological Nanopore for Real-Time Sensing of Single Chemical and Sequencing of DNA. *Nano Today* **8**, 56–74 (2013).
6. Dekker, C. Solid-state nanopores. *Nature Nanotechnology* **2**, 209–215 (2007).
7. Chang, H. *et al.* DNA-mediated fluctuations in ionic current through silicon oxide nanopore channels. *Nano Lett* **4**, 1551–1556 (2004).
8. Smeets, R. M. M. *et al.* Salt Dependence of Ion Transport and DNA Translocation through Solid-State Nanopores. *Nano Lett.* **6**, 89–95 (2006).
9. Wang, V., Ermann, N. & Keyser, U. F. Current Enhancement in Solid-State Nanopores Depends on Three-Dimensional DNA Structure. *Nano Lett.* **19**, 5661–5666 (2019).
10. Steinbock, L. J., Lucas, A., Otto, O. & Keyser, U. F. Voltage-driven transport of ions and DNA through nanocapillaries. *Electrophoresis* **33**, 3480–3487 (2012).
11. Ho, C. *et al.* Electrolytic transport through a synthetic nanometer-diameter pore. *Proc. Natl. Acad. Sci. U.S.A.* **102**, 10445–10450 (2005).
12. Martins, D. C., Chu, V. & Conde, J. P. The effect of the surface functionalization and the electrolyte concentration on the electrical conductance of silica nanochannels. *Biomicrofluidics* **7**, 034111 (2013).
13. Stein, D., Kruithof, M. & Dekker, C. Surface-Charge-Governed Ion Transport in Nanofluidic Channels. *Phys. Rev. Lett.* **93**, 035901 (2004).

14. Karnik, R., Castelino, K., Fan, R., Yang, P. & Majumdar, A. Effects of Biological Reactions and Modifications on Conductance of Nanofluidic Channels. *Nano Lett.* **5**, 1638–1642 (2005).
15. Siwy, Z., Kosińska, I. D., Fuliński, A. & Martin, C. R. Asymmetric Diffusion through Synthetic Nanopores. *Phys. Rev. Lett.* **94**, 048102 (2005).
16. Fan, R. *et al.* DNA Translocation in Inorganic Nanotubes. *Nano Lett.* **5**, 1633–1637 (2005).
17. Cui, S. Current blockade in nanopores in the presence of double-stranded DNA and the microscopic mechanisms. *J Phys Chem B* **114**, 2015–2022 (2010).
18. Cui, S. T. Counterion-Hopping along the Backbone of Single-Stranded DNA in Nanometer Pores: A Mechanism for Current Conduction. *Phys. Rev. Lett.* **98**, 138101 (2007).
19. Smeets, R. M. M., Keyser, U. F., Dekker, N. H. & Dekker, C. Noise in solid-state nanopores. *Proceedings of the National Academy of Sciences* **105**, 417–421 (2008).
20. Wanunu, M., Morrison, W., Rabin, Y., Grosberg, A. Y. & Meller, A. Electrostatic focusing of unlabelled DNA into nanoscale pores using a salt gradient. *Nature Nanotechnology* **5**, 160–165 (2010).
21. Zhang, Y. *et al.* Ionic current modulation from DNA translocation through nanopores under high ionic strength and concentration gradients. *Nanoscale* **9**, 930–939 (2017).
22. Luan, B. & Aksimentiev, A. Control and reversal of the electrophoretic force on DNA in a charged nanopore. *J. Phys.: Condens. Matter* **22**, 454123 (2010).
23. Zhan, L., Zhang, Y., Si, W., Sha, J. & Chen, Y. Detection and Separation of Single-Stranded DNA Fragments Using Solid-State Nanopores. *The Journal of Physical Chemistry Letters* **12**, 6469–6477 (2021).
24. Yang, H. *et al.* Identification of single nucleotides by a tiny charged solid-state nanopore. *The Journal of Physical Chemistry B* **122**, 7929–7935 (2018).
25. Zhang, Y. *et al.* Electroosmotic Facilitated Protein Capture and Transport through Solid-State Nanopores with Diameter Larger than Length. *Small Methods* **4**, 1900893 (2020).
26. Karawdeniya, B. I., Bandara, Y. N. D., Nichols, J. W., Chevalier, R. B. & Dwyer, J. R. Surveying silicon nitride nanopores for glycomics and heparin quality assurance. *Nature communications* **9**, 1–8 (2018).

27. Ermann, N. *et al.* Promoting single-file DNA translocations through nanopores using electro-osmotic flow. *The Journal of chemical physics* **149**, 163311 (2018).
28. Bandara, Y. N. D. *et al.* Beyond nanopore sizing: improving solid-state single-molecule sensing performance, lifetime, and analyte scope for omics by targeting surface chemistry during fabrication. *Nanotechnology* **31**, 335707 (2020).
29. Levy, A., de Souza, J. P. & Bazant, M. Z. Breakdown of electroneutrality in nanopores. *Journal of Colloid and Interface Science* **579**, 162–176 (2020).
30. Subramaniam, A. *et al.* Analysis and Simulation of One-Dimensional Transport Models for Lithium Symmetric Cells. *Journal of The Electrochemical Society* **166**, A3806 (2019).
31. Steinbock, L. J., Bulushev, R. D., Krishnan, S., Raillon, C. & Radenovic, A. DNA Translocation through Low-Noise Glass Nanopores. *ACS Nano* **7**, 11255–11262 (2013).
32. J. Steinbock, L. *et al.* Probing the size of proteins with glass nanopores. *Nanoscale* **6**, 14380–14387 (2014).
33. Steinbock, L. J., Otto, O., Chimere, C., Gornall, J. & Keyser, U. F. Detecting DNA Folding with Nanocapillaries. *Nano Lett.* **10**, 2493–2497 (2010).
34. DeSorbo, W. Ultraviolet effects and aging effects on etching characteristics of fission tracks in polycarbonate film. *Nuclear Tracks* **3**, 13–32 (1979).
35. Ai, Y., Zhang, M., Joo, S. W., Cheney, M. A. & Qian, S. Effects of Electroosmotic Flow on Ionic Current Rectification in Conical Nanopores. *J. Phys. Chem. C* **114**, 3883–3890 (2010).
36. Behrens, S. H. & Grier, D. G. The charge of glass and silica surfaces. *J. Chem. Phys.* **115**, 6716–6721 (2001).
37. Sohi, A. N., Beamish, E., Tabard-Cossa, V. & Godin, M. DNA Capture by Nanopore Sensors under Flow. *Anal. Chem.* **92**, 8108–8116 (2020).
38. Charron, M., Briggs, K., King, S., Waugh, M. & Tabard-Cossa, V. Precise DNA Concentration Measurements with Nanopores by Controlled Counting. *Anal. Chem.* **91**, 12228–12237 (2019).
39. Grosberg, A. Y. & Rabin, Y. DNA capture into a nanopore: Interplay of diffusion and electrohydrodynamics. *J. Chem. Phys.* **133**, 165102 (2010).
40. Qiao, L. & Slater, G. W. Capture of rod-like molecules by a nanopore: Defining an “orientational capture radius”. *J. Chem. Phys.* **152**, 144902 (2020).

41. Laohakunakorn, N., Thacker, V. V., Muthukumar, M. & Keyser, U. F. Electroosmotic Flow Reversal Outside Glass Nanopores. *Nano Lett.* **15**, 695–702 (2015).
42. Ferree, S. & Blanch, H. W. Electrokinetic Stretching of Tethered DNA. *Biophysical Journal* **85**, 2539–2546 (2003).
43. Plesa, C. *et al.* Direct observation of DNA knots using a solid-state nanopore. *Nature Nanotech* **11**, 1093–1097 (2016).
44. Kumar Sharma, R., Agrawal, I., Dai, L., Doyle, P. S. & Garaj, S. Complex DNA knots detected with a nanopore sensor. *Nature Communications* **10**, 4473 (2019).
45. Li, J., Gershow, M., Stein, D., Brandin, E. & Golovchenko, J. A. DNA molecules and configurations in a solid-state nanopore microscope. *Nature Materials* **2**, 611–615 (2003).
46. Storm, A. J., Chen, J. H., Zandbergen, H. W. & Dekker, C. Translocation of double-strand DNA through a silicon oxide nanopore. *Phys. Rev. E* **71**, 051903 (2005).
47. Comer, J., Dimitrov, V., Zhao, Q., Timp, G. & Aksimentiev, A. Microscopic Mechanics of Hairpin DNA Translocation through Synthetic Nanopores. *Biophysical Journal* **96**, 593–608 (2009).
48. Chen, K., Bell, N. A., Kong, J., Tian, Y. & Keyser, U. F. Direction-and salt-dependent ionic current signatures for DNA sensing with asymmetric nanopores. *Biophysical journal* **112**, 674–682 (2017).
49. Lan, W.-J., Kubeil, C., Xiong, J.-W., Bund, A. & White, H. S. Effect of surface charge on the resistive pulse wavelshape during particle translocation through glass nanopores. *The Journal of Physical Chemistry C* **118**, 2726–2734 (2014).
50. Pedone, D., Firnkens, M. & Rant, U. Data analysis of translocation events in nanopore experiments. *Analytical chemistry* **81**, 9689–9694 (2009).
51. Tivony, R., Safran, S., Pincus, P., Silbert, G. & Klein, J. Charging dynamics of an individual nanopore. *Nature communications* **9**, 1–8 (2018).
52. Gupta, A., Zuk, P. J. & Stone, H. A. Charging Dynamics of Overlapping Double Layers in a Cylindrical Nanopore. *Physical review letters* **125**, 076001 (2020).
53. Slowing down DNA Translocation through a Nanopore in Lithium Chloride | Nano Letters. <https://pubs.acs.org/doi/abs/10.1021/nl204273h>.

54. Lee, S. H. & Rasaiah, J. C. Molecular Dynamics Simulation of Ion Mobility. 2. Alkali Metal and Halide Ions Using the SPC/E Model for Water at 25 °C. *J. Phys. Chem.* **100**, 1420–1425 (1996).
55. Wang, P. *et al.* Genome Editing for Cancer Therapy: Delivery of Cas9 Protein/sgRNA Plasmid via a Gold Nanocluster/Lipid Core–Shell Nanocarrier. *Adv Sci (Weinh)* **4**, (2017).
56. Raper, A. T., Stephenson, A. A. & Suo, Z. Functional Insights Revealed by the Kinetic Mechanism of CRISPR/Cas9. *J. Am. Chem. Soc.* **140**, 2971–2984 (2018).
57. Lian, Z., Chao, H. & Wang, Z.-G. Effects of Confinement and Ion Adsorption in Ionic Liquid Supercapacitors with Nanoporous Electrodes. *ACS nano* (2021).
58. He, Y., Tsutsui, M., Scheicher, R. H., Miao, X. S. & Taniguchi, M. Salt-Gradient Approach for Regulating Capture-to-Translocation Dynamics of DNA with Nanochannel Sensors. *ACS Sens.* **1**, 807–816 (2016).

Chapter 3: Evaluating Electrolyte Conditions for Enhanced Detection of DNA and Protein Complexes

3.1 Abstract

Nanopores are a promising single-molecule sensing device class that captures molecular-level information through resistive or conductive pulse sensing (RPS and CPS). The latter is typically observed in low salt conditions and thought to arise from auxiliary ionic flux overcoming the volumetric occlusion of the analyte near the pore orifice. For the first time, we report toggling of RPS and CPS using salt gradients to modulate the transport properties of the canonical calibration standard of nanopore technology, λ -DNA, at relatively high salt concentrations (≥ 1 M). More specifically, CPS was observed when cation movement along both electrical and chemical gradients was favored which led to a $\sim 3\times$ improvement in SNR (i.e., signal to noise ratio) and an $\sim 8\times$ increase in translocation time. Interestingly, a reversal of the salt gradient reinstates the more conventional resistive pulses and may help elucidate RPS-CPS transitions. The asymmetric salt conditions also permitted the successful discrimination of DNA configurations including linear, partially folded, and completely folded DNA states. These findings were then utilized for the detection of Cas9 mutant, Cas9d10a—a protein with broad utilities in genetic engineering and immunology—bound to DNA target strands as well as the unbound Cas9d10a + sgRNA complexes; also showing significantly longer event durations than typically observed for proteins and demonstrating utilization for detection of other proteins via molecular carriers.

3.2 Introduction

Nanopores are an emerging high-throughput, low-cost overhead single-molecule sensing class with a predominantly growing application footprint in a myriad of biomolecule and bioparticle classes wherein properties and phenomenon such as protein folding^{1,2}, membrane and cargo properties of soft particles,³ glycan characterization,⁴ DNA configurations,^{5,6} topologies,^{7,8} and binding states⁹ have been investigated. The operational principle is simple, where a molecule transits across the nanopore in response to electrophoretic, electroosmotic, diffusion forces occluding the open-pore ion flow and generating resistive (or conductive) pulses that stamp analyte-specific information.¹⁰ Surface charge contributions—both from the nanopore and the analyte—come into play at low electrolyte concentrations where, for example, deviation from the ohmic nature of nanopore conductance is seen (i.e., ion current rectification). Similarly, an interplay between the volume occlusion by the analyte and mobile counterions carried by the analyte is thought to influence the event pulse nature (i.e., resistive or conductive and their shape) where the latter become prominent at low ionic strengths (i.e. < 0.4 M) and has been speculated to lead to conductive pulses.^{11,12} Unlike cylindrical nanopores where a nearly uniform electric field exists across the pore (especially for high aspect ratio pores), conical nanopores have a higher electric field near its orifice leading to potentially asymmetric current signatures. Thus, pulse sensing in conical nanopores is more complex and even provides directional context pertaining to analyte movement (i.e., to or from the tapered nanopore interior) which cylindrical nanopores cannot provide. Moreover, the signal to noise ratio (SNR), pulse shape, and throughput are also dependent on the transit direction

in tapered pores which adds an extra layer of complexity over its cylindrical counterparts. The asymmetric electric field induced effects in tapered pores suggests that they are phenomenologically divergent from their cylindrical counterparts, rendering interpolation of observations challenging in some instances. For example, asymmetric electroosmotic flow in tapered geometries leads to different capture rates depending on the transit direction.¹³

Salt asymmetry has been used with planar nanopores where a simultaneous increase in throughput and translocation time was observed with decreasing *cis* concentration. For example, the work of Wanunu et. al. shows the capture of DNA at a mere 3.8 pM concentration while maintaining an appreciable capture rate of ~ 1 molecule/s¹⁴ and the concept has been further explored by others to flag target molecules through molecular transit retardation.¹⁵ Notably, the *cis* component was always at a low salt concentration (i.e., ~ 0.2 M and below mostly) except in a few select cases¹⁶. Typically, the *trans* side (i.e., voltage application chamber) is kept at a higher concentration compared to the *cis* chamber (grounded side) and a positive bias (in the case of DNA) is applied to the *trans* side which causes the positive ions to flow in favor of chemical and electrical gradients (*trans* to *cis*) polarizing the *cis* side pore opening leading to a higher capture rate and slower translocation time. However, to the best of our knowledge, no prior work exists with the use of asymmetric salt conditions with nanopipettes.

Given the plethora of unique transport phenomena exhibited by tapered configurations,^{17–20} it is worthwhile exploring how such gradients would impact the

transport properties of molecules across such geometries. Thus, we seek to explore the influence of salt asymmetry over translocation properties using the canonical benchmark molecule, DNA (more specifically λ -DNA). DNA has been the most commonly used analyte for nanopore experiments given its stability and uniform linear charge density. Because of this, a vast number of discoveries pertaining to different DNA configurations as it enters the pore have been published^{7,8,21}. Event properties stemming from multi-level events (folded in some way) are different than linearly translocating DNA events. For example, DNA folding occurs more often in larger pores as well as with longer DNA strands compared to smaller pores and shorter DNA strands, respectively^{22,23}. The ability to distinguish between linear and nonlinear DNA configurations is highly advantageous to biophysical applications such as the use of molecular carriers, DNA data storage, and sequencing. For example, when a molecule is bound to DNA, the complex yields a secondary change in current^{6,9}, similar to a folded/knotted DNA.

Promoting single-file DNA translocations is a key factor for the accurate detection molecules bound to DNA whereby false-positive classification of folded/knotted DNA as a bound molecular carrier can be minimized. Furthermore, linearized DNA is preferred for sequencing (also used to read out data-encoded DNA) efforts to minimize conformational ambiguity within the constricted 3D space of the sensing zone. Intuitively, promoting linearized (i.e., single file) DNA translocations would also minimize analyte clogging in the < 5 nm pore regime where the size is just enough for folded over conformations. Thus, linearized DNA translocations have intriguing applications (and implications) in nanopore technology. However, irrespective of the approach, a sufficiently high enough SNR should

be maintained to discriminate from open-pore noise and its subtle variations and become even more crucial in multi-analyte samples. To this extent, we explored various asymmetric salt conditions and toggled the starting location of the analyte (i.e., bath vs inside the taper) as well.

Despite operating at a higher electrolyte concentration, we observed conductive pulses that are typically seen with low electrolyte concentration regimes due to a secondary ionic flow mechanism outweighing volumetric occlusions.²⁴ In addition to the conventionally offered advantages by the asymmetric salt condition such as higher throughput and slower translocation time, the high salt conditions offer high SNR to improve pulse detection capability. The opposing cationic flow could, in theory, lead to a higher linear translocation population analogous to that seen in cases where electrophoretic force is opposed by the electroosmotic force. This is more crucial with larger diameter pores where more 3D space is available for the transiting molecule to adopt a multitude of conformations such as partially folded, fully folded, and/or knotted. We hypothesized, the asymmetric electric field distribution within the nanopipette along with the salt gradient, could promote linear translocations over other conformations (partially folded, fully folded, or knotted).

Nanopipettes under asymmetric salt conditions were used to identify DNA folding states as well as protein-DNA complexes (Cas9 mutant bound to DNA). Cas9 is an RNA-guided DNA nuclease and plays a vital role in bacterial immunity and is widely used for gene editing applications. Although Cas9 is positively charged at the operational pH, the

guide RNA induces a charge reversal.²⁵ Detecting globular proteins such as Cas9 are mostly challenged by the inherent fast-moving (i.e., free translocations) nature of such, defying the electronic bounds of the ubiquitous amplifier used in the field. Solutions to overcome signal attenuation due to fast translocations include, but are not limited to, the use of higher bandwidth instruments, surface chemical modifications to promote protein-pore interactions, and, electroosmotic flow tuning²⁶⁻²⁸. Increasing the dwell time of translocating proteins is also of interest. Specifically, methods such as: functionalizing the nanopore wall with fluid bilayers²⁶ and working near the protein's isoelectric point,²⁹ among others, have demonstrated slowing-down translocating protein molecules. The ion flow associated with the salt gradient would substantially slow down the Cas9 movement (i.e., into milli-second regime), and given the structural and size difference compared to other components in the mixture, a unique pulse signature that is not attenuated could be detected. Although machine learning approaches to nanopore data analysis have been reported several times³⁰⁻³², we exploited these methods to detect DNA folding in conductive event data.

In this chapter, we compare the gold standard (high salt DNA translocations via electrophoretic forces) experimental condition with multiple variations of concentration gradients using glass nanopipettes. In a recently published study, we have shown the role of cationic flux in determining the electrical direction (either resistive or conductive) of events.³³ By utilizing asymmetric salt conditions, ion flux is generated and capable of sensing DNA configurations with enhanced discrimination between states, slowing down the DNA translocation speed, as well detecting topological structures on DNA (protein

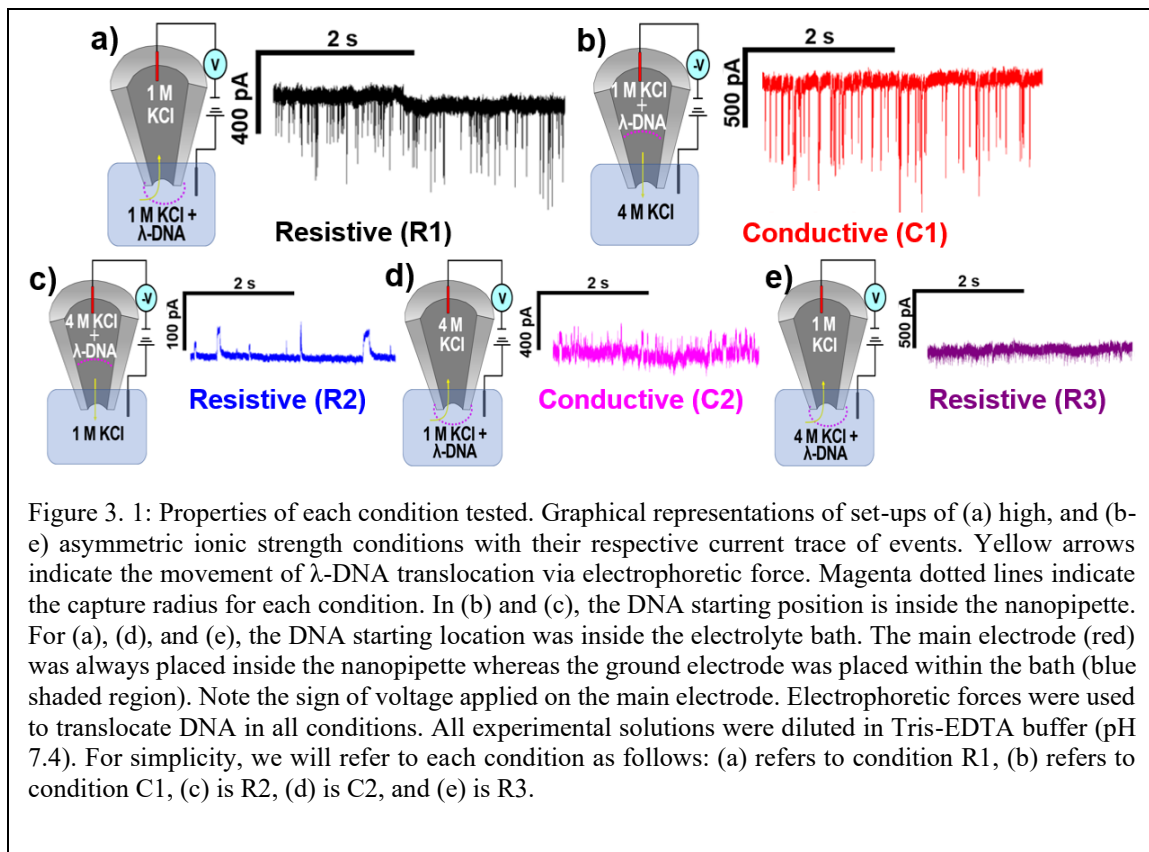
bound to DNA), all of which stem from an understanding of flux imbalances within the pore.

3.3 Results and Discussion

3.3.1 Various Electrolyte Conditions

Seven pores were fabricated (2 high and 5 asymmetric salts) from which five salt conditions were examined with one being symmetric and the other four being asymmetric to explore the effect of salt concentration and gradient direction on translocation properties of λ -DNA. More specifically, 1 M (high symmetric), 4 M/1 M (bath/pipette), and 1 M/4 M (bath/pipette) KCl concentrations buffered at the physiological pH (~ 7.4) were used (Figure 3.1). Since the Debye length shares an inverse relationship with electrolyte concentration, the effect of the counterion layer proximal to the nanopore surface charge arising from the deprotonation of surface head groups (or protonation of head groups in the case of basic functional groups) to the overall nanopore conductance become more apparent at low salt concentrations. This is also known to induce ion concentration polarization effects where accumulation or depletion of ions take place in response to an applied voltage bias and have been postulated to influence the shape and direction of the pulse.³⁴ This argument is in good agreement with our observations with 1 M KCl (symmetric case), where pulses are resistive. In the case with symmetric 1 M KCl configuration, the suppression of the electrical double layer meant electroosmotic forces are meager and the translocation takes place via electrophoretic movement of DNA (Figure 1a, condition R1). Despite electroosmotic flow and conductive events often coinciding,

they are not mechanistically linked. For example, we observed conductive events with electrophoretic translocations under (high) asymmetric salt conditions. Furthermore, others have reported electrophoretic and conductive events by using PEG to reduce EOF.³⁵ Reports of conductive events occurring in nanopores where EOF is reduced to allow electrophoretically-driven events also produced conductive events.³⁶ The hypothesis concerning the introduction of counterions by DNA cannot be applied to the high salt 4 M/1 M (bath/pipette + DNA) KCl gradients in which conductive pulses were observed (Figure 3.1b, condition C1). Instead, our results complement a previous report stating that flux imbalances play a significant role in determining the event shape (i.e., conductive or resistive).³³ Interestingly, Zhang et. al. observed a similar trend with planar silicon nitride nanopores with 1 M/4 M (*cis/trans*) NaCl gradient where they attributed the current enhancement at high salt concentrations to strong electroosmotic flow in the region between the nanopore surface and DNA (i.e., the outer section in their simulation).³⁷ They hypothesized, with a salt gradient, the electroosmotic flow is enhanced and helps bring more ions to the nanopore effectively increasing the drift current leading to conductive pulses. However, a reversed gradient where the *cis* side is higher than the *trans* side (i.e., 4 M/1 M (*cis/trans*) NaCl gradient) was not provided in that study to provide more concrete evidence to the proposed theory.



We speculate, in the C1 gradient (4 M/1 M (bath/pipette + DNA) KCl), the preferential cation flow through both electrical and chemical gradient from bath to the pipette creates a polarized zone near the inner pipette side of the pore. Thus, when DNA translocates from the pipette side to the bath side, it introduces more cations to the pore tip as it disturbs the cation distribution near the pore orifice in the inner pipette side. However, when the gradient is reversed (i.e., Figure 3.1c, condition R2), the ion polarization is near the pore opening on the bath side. Thus, the translocation of DNA from the pipette side to the bath side does not introduce additional ions to the pore to increase its local conductivity. To further prove this hypothesis, we conducted two additional experiments where the DNA

was kept at the bath side with the 1 M/4 M (bath + DNA/pipette, Figure 3.1d, condition C2) and 4 M/1 M (bath + DNA/pipette, Figure 3.1e, condition R3) salt gradients. In the case of C2 gradient, the application of a positive voltage to the pipette side drives the cations along the chemical and electrical gradient to the bath side generating a polarized zone near the pipette tip in the bath side while DNA translocates opposing this ion travel generating conductive pulses as expected. In the case of R3 gradient, the ion travel and DNA translocation would be to the same side and generate resistive pulses as expected. We chose to utilize the C1 condition for the remainder of this study as it provided the best SNR and event rate in comparison to the other asymmetric (R2, C2, and R3) conditions. We attribute the differences in signal of all six conditions to stem mainly from salt concentrations (high or asymmetric), DNA starting location (in nanopipette or the bath), and direction of translocation (electrophoretic forces against or with cation flow). Signal dependency on pore size will be discussed regarding high and asymmetric (C1) salt.

Both high R1 and asymmetric C1 conditions (Figure 3.2a and 3.2b) led to 67% single file translocations for the smaller pore sizes (~ 9 nm and 8 nm, respectively). Next, a larger pore was used (~ 40 nm) under asymmetric C1 conditions, and the distribution was still 65% single file translocations. This is despite the fact that larger pores inevitably tend to permit greater folded configurations of DNA. The larger pore (~ 25 nm) at the high R1 salt condition was the least favorable to passing linear DNA with approximately 10% single file translocations. Larger pores invariably permit the translocation of a multitude of conformations such as folded over, loop, and knotted partly due to the available 3D space. This is also related to the persistence length of DNA: the electrostatic persistence length of

DNA is $\sim 3\times$ less than the size of the larger pore. Despite operating in the electrophoretic dominant transport regime, salt gradients have an added advantage over symmetric salt configurations: they can oppose the travel of DNA through the transport of ions through electrical and chemical gradients. We hypothesized, this opposition, which is the case with the C1 gradient configuration, can promote single-file translocations (Appendix B Figure B.S2) analogous to electroosmotic flow opposing the electrophoretic motion.³⁸

3.3.2 Signal Properties of High Symmetric Compared to High Asymmetric

In both cases (C1 and R1), we see an increase in the variability of ΔI with increasing pore diameter (Figure 3.2a and b), which also alludes to the fact that DNA folding is more likely at larger pore sizes. After retrieving current change information, a 30-second current trace containing no events was analyzed for the RMS noise of the signal. The changes in the current and noise calculations for each of the four pores under both conditions were used to determine the SNR of each condition as a function of pore diameter (Figure 3.2c).

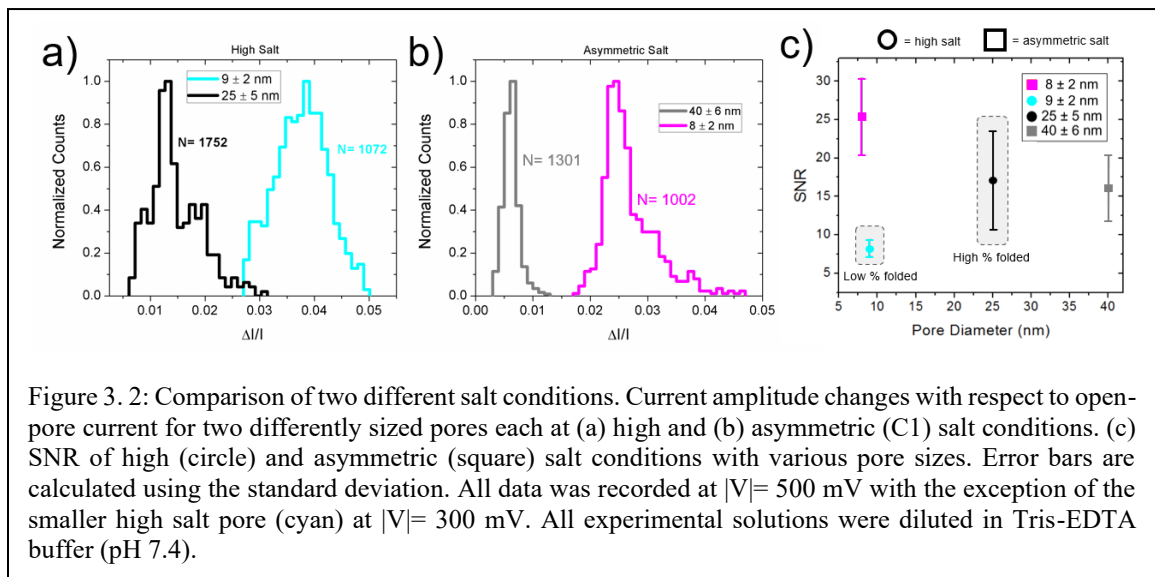


Figure 3. 2: Comparison of two different salt conditions. Current amplitude changes with respect to open-pore current for two differently sized pores each at (a) high and (b) asymmetric (C1) salt conditions. (c) SNR of high (circle) and asymmetric (square) salt conditions with various pore sizes. Error bars are calculated using the standard deviation. All data was recorded at $|V|= 500$ mV with the exception of the smaller high salt pore (cyan) at $|V|= 300$ mV. All experimental solutions were diluted in Tris-EDTA buffer (pH 7.4).

This trend is expected since the more available 3D space within the larger pore would facilitate non-linear conformations. This increase in standard deviation, seen in Figure 3.2c, goes hand in hand with the different configurations that DNA assumes upon translocation when the pore size is greater than double the DNA cross-sectional area. The larger pore sizes (seen mostly at high salt) allow for more opportunities for DNA to translocate the pore in folded configurations which increase the current amplitude, thus increasing the standard deviation of the SNR. An investigation of the capture rates of high symmetric (R1) salt and R3 salt was performed and can be found in Figure B.S3 in Appendix B.

Based on the data collected at each salt condition, it was evident that folded DNA was present and qualitatively more distinguishable from other configurations under asymmetric salt conditions. A comparative analysis to find which salt condition would yield the best discrimination of DNA folding states was therefore worthwhile. For this, a machine learning algorithm (Appendix B Figure B.S4) based on support vector machines was developed to categorize DNA events into three frequently seen configurations: linear, partially folded, and fully folded. Events used for the classification of each population are shown in Figure 3.3a where linear, partially folded, and fully folded are displayed in green, navy, and maroon, respectively. At least 10 events are selected as examples of each configuration in the training set for three classes. It is important to note, at any given voltage, the knot configurations were negligible compared to linear, partially folded, and fully folded configurations. Depending on the configuration of DNA as it enters the capture zone, DNA will translocate either linearly, folded in some way, or knotted. If DNA is captured along its backbone or at its ends, it can translocate the pore in a folded or linear

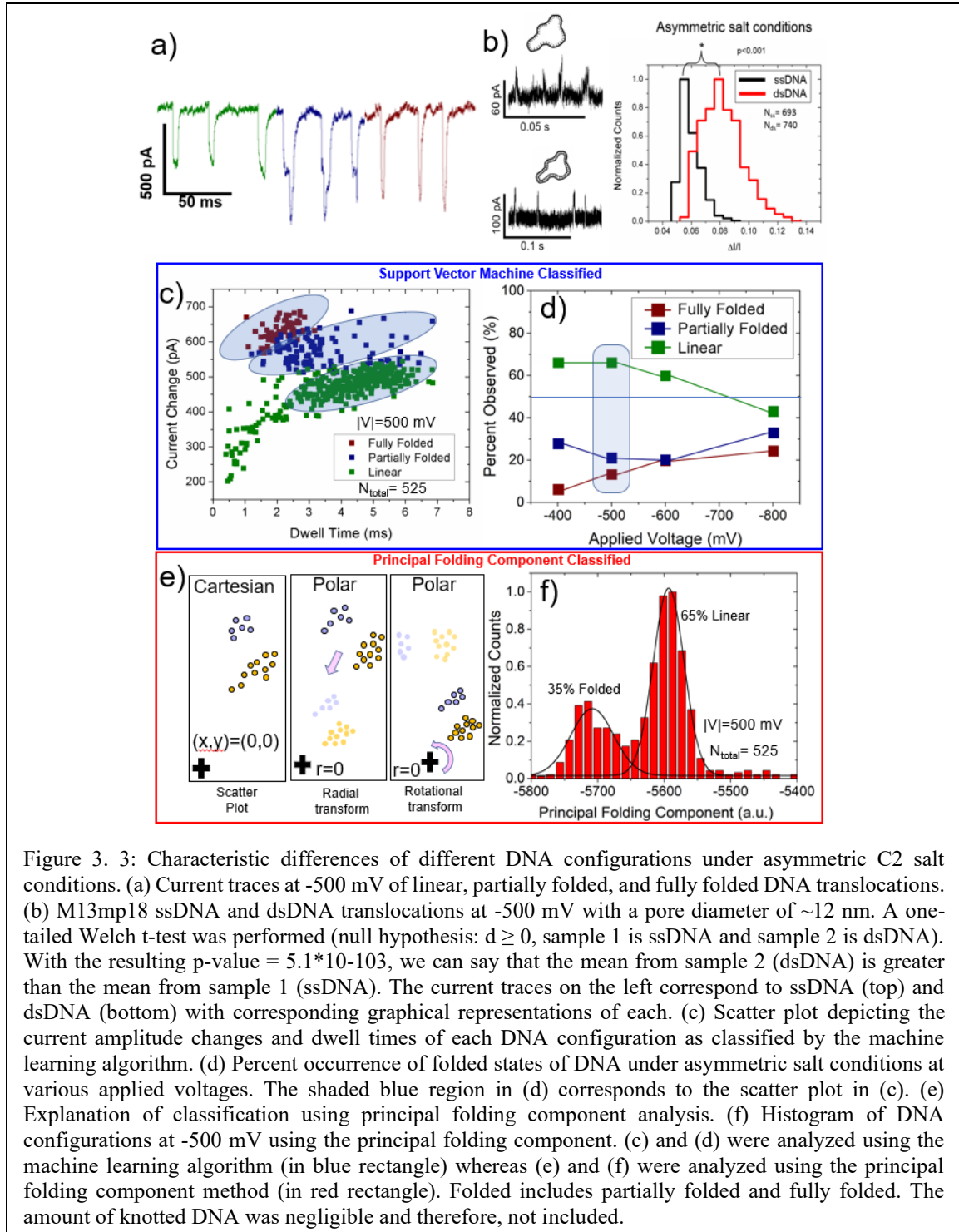
configuration, respectively. To confirm that the event shapes are due to different DNA configurations, an experiment using M13mp18 ssDNA and dsDNA was performed. The ssDNA and dsDNA acted as representatives of linear and folded DNA, respectively, when entering the pore. The same pore (~12 nm in diameter) was used for both analytes as well as the same applied voltage (-500 mV) under the asymmetric C1 conditions. The results can be seen in Figure 3b, where a one-tailed Welch t-test was executed, producing a p-value = 5.1×10^{-103} . Therefore, the mean $\Delta I/I$ of dsDNA (mimicking folded DNA) is greater than the mean $\Delta I/I$ of ssDNA (mimicking linear DNA). These results support that the secondary changes in current can be explained by different DNA configurations, i.e., an increased change in current amplitude is due to > 1 DNA strands in the pore at once.

3.3.3 Machine Learning Techniques

Linear kernels were then used to divide the multi-dimensional space between each class, yielding three DNA configurations classified via linear support vector machine learning (Figure 3.3c). This process was repeated for various voltages and the percentage configurations for each class can be seen in Figure 3.3d. Next, we investigated the effect of voltage on the translocation conformation of DNA. Specifically, it is the funnel-shaped distribution of voltage near the pore that interacts with the flexible polymer DNA chain and leads to the different folding configurations observed here. Few reports of DNA folding exist as a function of voltage³⁹, especially for asymmetric salt conditions and DNA exiting the confinement of a nanopipette. The enhanced ability to resolve the different folding states of DNA under asymmetric salt conditions also makes the voltage effects worth investigating. For this set of experiments, we used a ~8 nm pore with the C1 salt

conditions. Based on support vector machine classification, the linear percentage decreased with increasingly negative voltage (Figure 3.3d). This is contrary to what has been observed with planar nanopores under symmetric voltage conditions where single-level translocations increase with increasing applied voltage due to the stretching of DNA by the electric field.³⁹ We speculate that asymmetric salt conditions, preferential cationic (K^+) pumping counter to DNA motion, and the persistence length DNA, play key roles in this observation. That is, with increasingly negative applied voltage, more cations are pumped through the chemical and potential gradients across the pore leading to an increase in ion accumulation near the pore opening. Appendix B Figure B.S5 illustrates the current amplitude of R1 and C1 conditions along with their respective RMS noise. Since the persistence length decreases with increasing ion concentration, at lower voltages, the

polymer would be less flexible compared to higher voltages and outweigh the electric field-induced stretching of DNA which could explain the folding trends seen in Figure 3.3d.



Although machine learning provided an excellent method of classifying events (Appendix B Figure B.S6), the drawbacks include i) the need for training and ii) the possibility of training bias. Since the folding states were so clearly identifiable based on the scatter plot (Figure 3.3c), we believed that an alternative method could be also used based on principal component analysis and 1-dimensional binning. However, because of the large variance of linearly translocating events, specifically the events with shorter dwell times, principal component analysis (PCA) failed to provide a principal component for the classification of the DNA folding states. Instead, we transformed the dwell time and current change axes into a single principal component, which could be used to classify different DNA folding populations. The procedure for extracting the principal folding component (PFC) starts by transforming the dwell time and current amplitude into a polar coordinate system. The polar coordinates are then translated and rotated by user-inputted values to enhance the clustering of events along one axis (Figure 3.3e). To automate the process and avoid user input, the translation and rotation steps were automated to maximize Chi-square goodness-of-fit test. With and without training sets (SVM versus PFC), both classification methods showed similar results (roughly 65% linear events at $|\Delta V|=500$ mV, Figure 3.3f).

Again, utilizing the principal folding component analysis, the process of classifying different DNA shapes was repeated under high and low salt conditions at $|\Delta V|=500$ mV (Figure 4). Both histograms and density scatter plots are shown for both asymmetric and high salt conditions (Figure 3.4a and b, respectively) with their corresponding Gaussian best fits. The black dotted lines were added as visual aids that discriminate between linear and folded DNA events. Unlike high salt, asymmetric C1 salt shows a distinct ability to

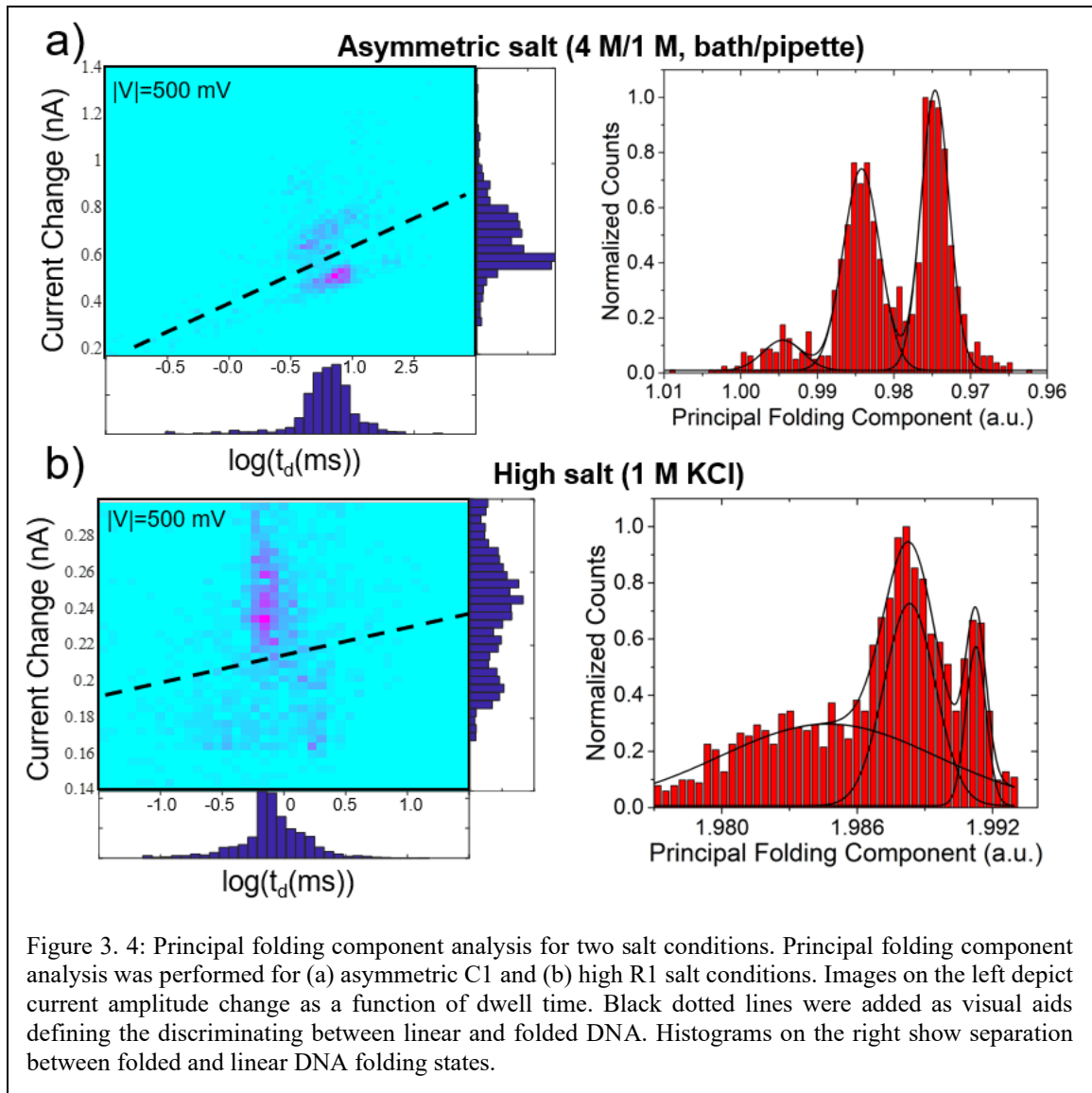


Figure 3. 4: Principal folding component analysis for two salt conditions. Principal folding component analysis was performed for (a) asymmetric C1 and (b) high R1 salt conditions. Images on the left depict current amplitude change as a function of dwell time. Black dotted lines were added as visual aids defining the discriminating between linear and folded DNA. Histograms on the right show separation between folded and linear DNA folding states.

discriminate folding states based on dwell time which leads to a slanted axis of folding discrimination. Additionally, we see a great separation between the classes of DNA as shown by the peaks (Figure 3.4a, right). High R1 salt conditions enable classification to occur mostly upon the current change parameter and slightly upon dwell time. We also begin to see each class peak become shorter in distance to one another. High salt conditions have the greater overlap between differing DNA configurations. The area under the curve (specifically: the overlapping distributions on the PFC axis) corresponds to the degree of uncertainty about the events that lie within that overlapping region. In this regard, asymmetric C1 salt led to the least amount of overlap. The data indicates that the salt influences the DNA configuration inside the pore and possibly is related to the smaller persistence length of DNA at higher salt⁴⁰. In other words, at higher salt concentrations, the DNA is more compact and therefore more likely to enter the pore in the folded state. In this work, both pore size and salt concentration seem to influence DNA folding during translocation.

3.3.4 Event Characteristic Differences Between Symmetric and Asymmetric Salt

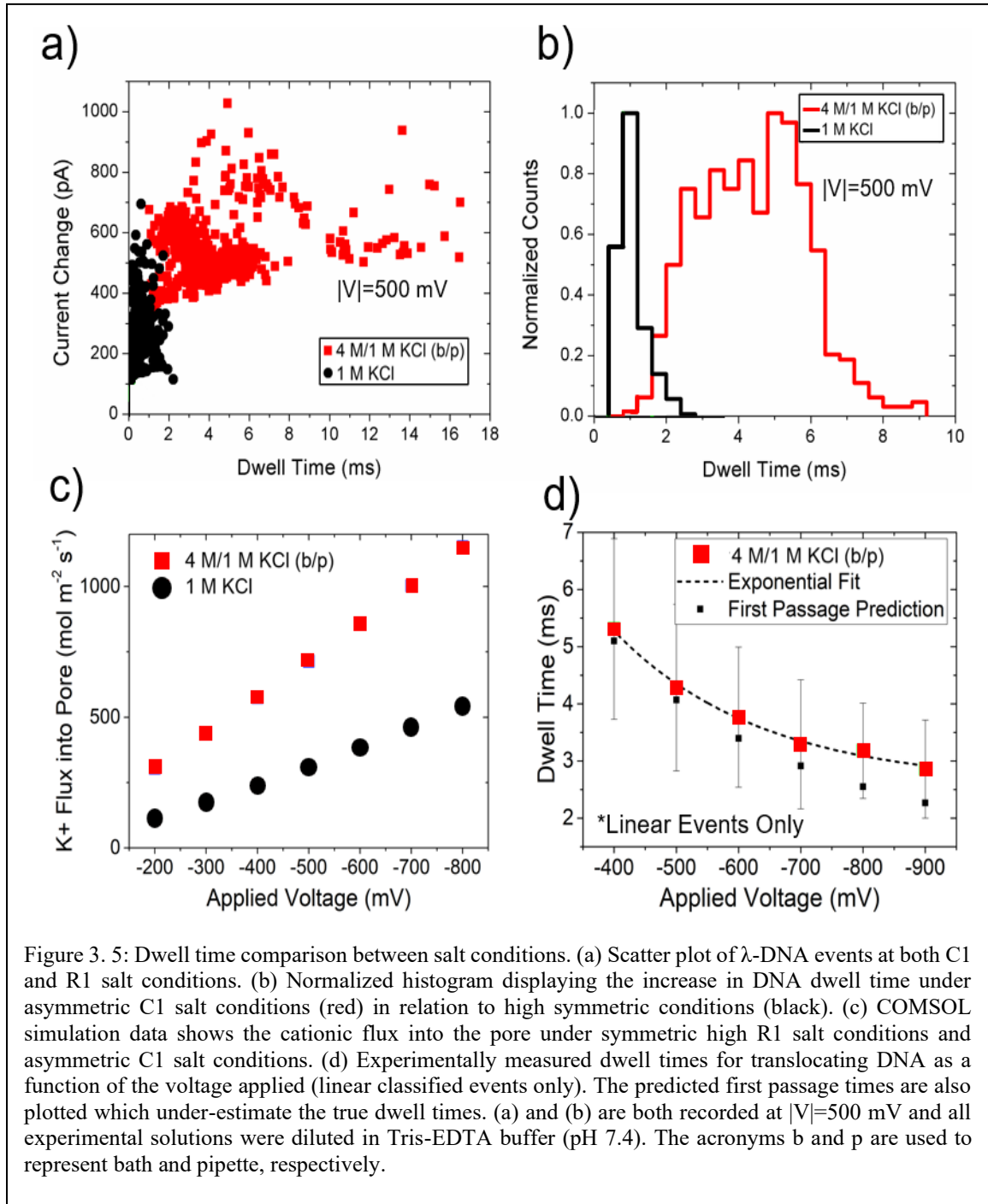
By comparing both conditions (Figure 3.5a), it was clear that DNA translocations were slowest under asymmetric salt conditions (all pores biased at $|V|=500$ mV). What is most noticeable in Figure 5a is that for symmetric high R1 salt conditions, the events are tightly clustered together, with little to no visualization of more than one population. On the other hand, under asymmetric C1 salt conditions (red squares), we begin to see the formations of differing populations. Additionally, when looking at the event dwell times, we see that asymmetric salt conditions appear to “slow down” the translocating DNA

molecule by around $\sim 8\times$ in comparison to the symmetric high R1 salt conditions (Figure 3.5b). Since the electroosmotic flow is expected to be negligible, the large influx of potassium into the pore (from the 4 M side to the 1 M side) may impart drag on the DNA, which transits the pore in the opposite direction. Under the 10^6 V/m electric fields inside the pore, the ionic velocities and drag effects can be significant.^{41–43} In asymmetric salt conditions, we believe that potassium is electrophoretically pumped into the pore and so we explored the aspect of ionic flux as a possible explanation for the increase in dwell time. COMSOL simulations revealed that concentration gradients present a flux imbalance in favor of K^+ more so than its symmetric counterparts (Figure 3.5c). Because of the combating electrophoretic force against the cationic flux, the translocating DNA molecule is “slowed down” by going against the large influx of potassium into the pore. A voltage-dependent study of dwell time was then conducted to determine how the potassium flux and DNA velocity scale with voltage. By taking only the linear DNA events we observed an exponential decay in dwell time (Figure 3.5d). The data point at $|\Delta V|=400$ mV was fit using the first passage time equation given by:

$$f(\tau) = \frac{l}{\sqrt{4\pi D\tau^3}} \exp\left(-\frac{(l-v\tau)^2}{4D\tau}\right) \quad (2)$$

where τ , D , v and l are the effective passage or dwell time of DNA, the diffusion coefficient of DNA, the drift velocity of DNA, and the effective sensing length of the nanopipette, respectively. D , v , and l were used as fitting parameters in the $|\Delta V|=400$ mV case, and D and l were kept constant for all voltages thereafter ($D=5\times 10^{-10}$ m²/s, $l=10$ μ m). The velocity of DNA was then scaled to the experimentally applied ΔV to show the

expected trend in DNA dwell time. We observed that the experimental data on dwell time was consistently slower (longer dwell times) than predicted by first passage time statistics. The difference is most extreme at the highest voltage applied ($\Delta V = -900$ mV). The first



passage fit of experimental data at -400 mV, as well as the first passage probability curves can be found in Appendix Figure B.S7.

3.3.5 Molecular Carrier Detection Under Asymmetric Conditions

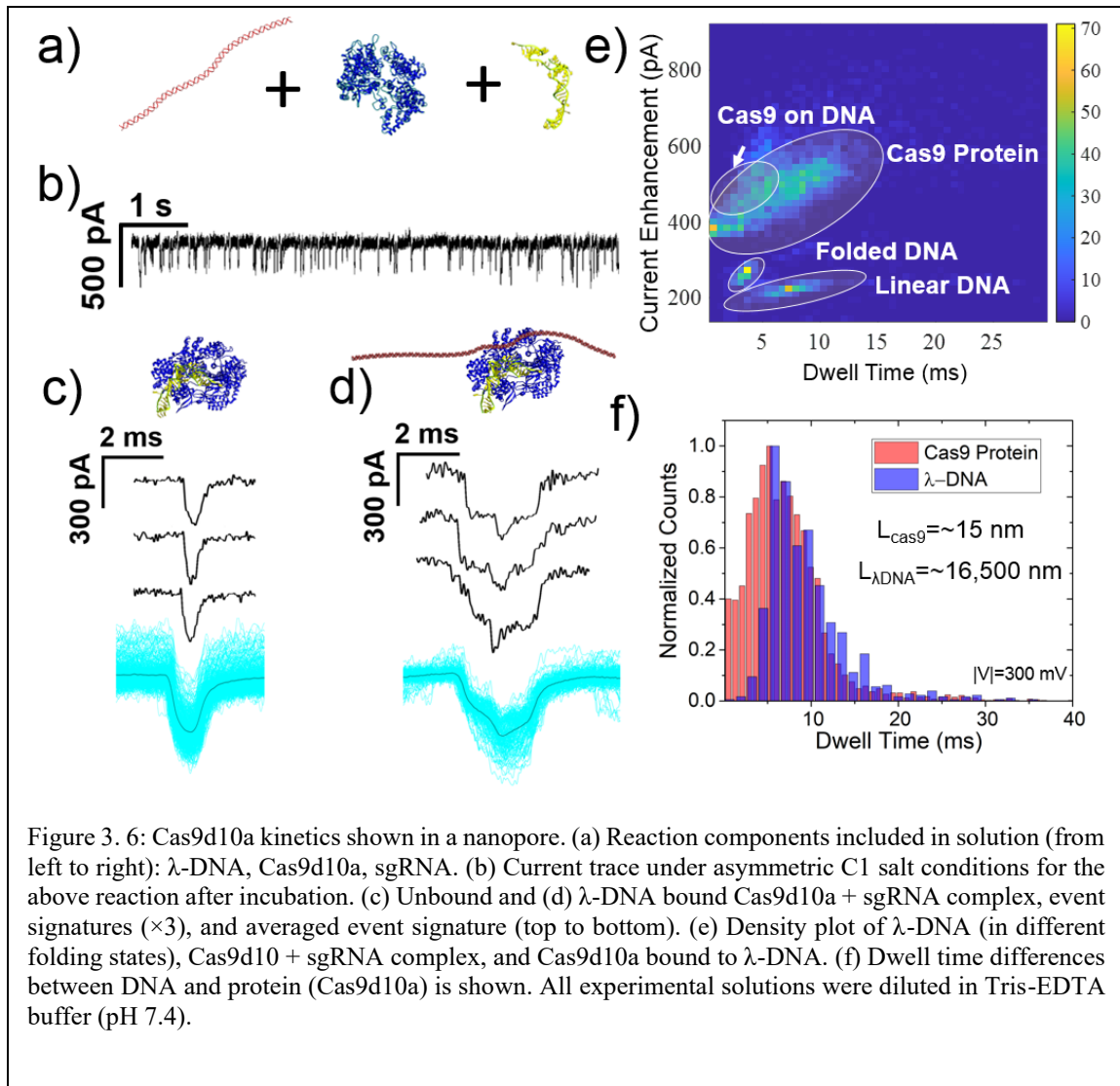
Fast protein translocations defying the bandwidth limitations is well documented and often require physical methods (e.g., application of pressure opposing the electrophoretic movement), chemical methods (e.g., pH), or the use of high bandwidth equipment.^{44,45} The asymmetric Cl salt gradient (a chemical approach) could slow down the transport velocity of proteins analogous to DNA as shown above. Herein, we used the Cas9 mutant, Cas9d10a, for this purpose where we saw the dwell time to be ~5 ms (through a ~25 nm pore under -300 mV) which is slower than the bandwidth-imposed transit time limitation as discussed previously. This permits us to detect any unbound Cas9d10a from the method discussed below without being subjected to finite filter response-driven signal attenuations. Previously, Weckman et. al.⁴⁶ and Yang et. al.⁴⁷ both contributed to detecting dCas9 bound to DNA in LiCl using quartz nanocapillaries and planar nanopores, respectively.

For this study, we chose the more ubiquitous salt of choice, KCl, partly because both the ions are borderline/kosmotropic ions of the Hofmeister series while lithium ion is thought to be a chaotropic ion.^{48,49} Cas9d10a is a nicking enzyme, only creating a single-stranded nick in the DNA sequence when bound. Cas9d10a was incubated with sgRNA and λ -DNA for 30 minutes at 37°C. It is important to note that we did not denature the DNA afterward to yield the nicked products (Cas9 stays bound to the DNA long after

nicking takes place⁵⁰), therefore the only species detectable within the nanopore is unbound Cas9d10a + sgRNA and Cas9d10a + sgRNA bound to λ -DNA (Figure 3.6a). A molar excess of Cas9d10a and sgRNA was added to the solution to ensure all λ -DNA would have one Cas9d10a + sgRNA bound. After incubation, the reaction solution was diluted with 1 M KCl and backfilled into the nanopore which was then inserted into the 4 M KCl electrolyte bath. Events were recorded at -300 mV and the typical current trace of events can be seen in Figure 3.6b. Three event signatures of Cas9d10a + sgRNA (unbound complex) and Cas9d10a + sgRNA bound to λ -DNA (bound complex) are shown in Figures 3.6c and d, respectively. Each event was overlaid on top of each other in cyan to illustrate the template for both populations, with the average shown with a black line. As seen with waveforms shown in Figure 6d, the bound complex exhibits a multi-level event signature. The second, high blockage current level is thought to be arising from the Cas9d10a + sgRNA bound to the template dsDNA. Although this experiment was overwhelmed with Cas9d10a + sgRNA events due to a 30 \times molar excess of the Cas9 + sgRNA, nearly all DNA events had a second, high blockade level indicating that it is unlikely that knots are forming this unique signature. A second experiment was done with Cas9d10a without DNA but in the presence of sgRNA. At the operational pH, Cas9d10a alone is positively charged and negatively charged with sgRNA bound.²⁵ Thus, Cas9 was placed inside the nanopipette, and a negative voltage bias was used to translocate the analyte (same conditions as the DNA under asymmetric C1 salt conditions). The density scatter plot (Figure 3.6e) shows that Cas9d10a + sgRNA has a greater current amplitude change in comparison to free DNA (different pores under the same asymmetric conditions). The

Cas9d10a + sgRNA complex exhibits a greater change in current in comparison to both the folded and linear DNA. The pore size of the Cas9d10a + sgRNA study was estimated to be ~17 nm in diameter, which is slightly larger than the pore used for DNA translocations (~11 nm). This, in combination with K^+ flux opposing the translocation, could be the reason why the current amplitude is higher for Cas9d10a + sgRNA. It is important to note that the number of events stemming from Cas9d10a + sgRNA + DNA is substantially lower in comparison to the number of events from Cas9d10a + sgRNA complex, which is due to the molar excess in favor of Cas9d10 + sgRNA. Because of this, and for ease of interpretation, we have circled where the population of each molecular complex lies within Figure 3.6e. Despite the great variation in length between Cas9d10a and DNA, we see similar dwell times for both (Figure 3.6f). The possible reasoning behind this stems from large potassium flux which would preferentially affect molecules with larger cross-sectional areas. A folded Cas9 protein would occupy a greater cross-sectional area of the pore compared to DNA. We find that our experimental conditions yielded analogous dwell times in comparison to previous studies using dCas9 bound to DNA. Specifically, we see Cas9d10a bound to DNA translocate the pore majorly between 3 and 6 ms. Previously (Figure 3.5c), we have shown that asymmetric salt conditions, with DNA as the analyte, exhibit a flux imbalance in favor of the cation, K^+ , which increases as the voltage applied increases in negativity. The ionic flux generated from asymmetric salt conditions has been previously described to slowdown the translocation of DNA.¹⁴ Thus, under the asymmetric salt (C1) conditions, it is not surprising to witness longer dwell times than what would normally be seen for proteins. Similar to how cationic flux slows down translocating

(negatively charged) DNA molecules, we can anticipate that cationic flux slows down the translocating Cas9d10a molecule as well. If the cationic flux is indeed responsible for the slowdown effect, it is likely that larger cross-sectional areas of the molecule would exacerbate the reduction in velocity. Notably, Cas9 has a much larger cross-sectional area compared to DNA. Nevertheless, we cannot entirely rule out the possibility of protein transiently binding to the pore surface as it translocates.



3.4 Conclusion

In this study, we showcase the impact of salt gradients, their direction (i.e., normal or reversed) on translocation pulse direction, translocation time, and conformation distribution. The salt gradient direction enables the toggling of pulse direction attributed to the flux imbalance. For example, the addition of DNA to the higher electrolyte bath causes conventionally observed resistive pulses whereas when reversed, conductive pulses were observed. In a salt gradient system, ion movement along chemical and electrical gradients can be used to either slow down or accelerate the transit velocity. With the canonical benchmark analyte (λ -DNA), an $\sim 8\times$ retardation of the translocation time was observed when opposing the cation pumping (C1 gradient) compared to the DNA motion at symmetric high salt (R1) conditions. Moreover, the C1 gradient also promoted single file translocations since both electroosmotic force and the cation pumping along the chemical and electrical gradients oppose the electrophoretic movement of λ -DNA wherein we observed 65% of translocation to be single file at -500 mV. Interestingly, the knotted population was meager compared to the linear, partially, and fully folded configurations which are significantly useful when discerning between Cas9d10a + sgRNA (unbound complex) and Cas9d10a + sgRNA bound to λ -DNA (bound complex). We further utilized this translocation configuration to slow down the transport of Cas9d10a, a mutant variant of the nicking protein Cas9.

Fast protein translations defying the electronic limitations set by the instrument bandwidths often become problematic and lead to signal attenuation. By employing the asymmetric C1 gradient, Cas9d10a traversed the nanopore majorly between 3-10 ms.

Additionally, we can discern between the bound and the unbound complex wherein we saw the unbound complex to be a single level event whereas the bound complex to have a signature resembling a 1-2-1 knot structure with the knot-like structure arising due to the presence of the Cas9d10a + sgRNA complex. This is of utmost importance when transitioning to detecting trypsin with λ -DNA. The findings presented in this study suggest that employing asymmetric salt conditions slows down translocating molecules provides higher resolution, improves SNR, and advances the classification of various protein and nucleic acid species within a nanopore.

3.5 Materials and Methods

3.5.1 Fabrication of Nanopores

Quartz nanopipettes (capillaries purchased from Sutter Instruments, QF100-70-7.5) were plasma leached prior to CO₂ laser-assisted pulling (P2000, Sutter Instruments). In brevity, the protocol to fabricate the pores were as follows: HEAT= 630, FIL= 4, VEL= 61, DEL= 145, PUL= values between 145 (larger diameter) and 225 (smaller diameter). The size was initially evaluated through a transmission electron microscope (Appendix B.S1) and more routinely with a solution-based conductance model (equation 1). Briefly, current-voltage (I/V) analysis was performed using Axopatch 200B (Molecular Devices, LLC) and Digidata 1550B (Molecular Devices, LLC) at the beginning of each experiment to determine the open-pore conductance (G) of each pore used (Appendix B.S1). The data were acquired at a sampling rate 250 kHz and lowpass filtered at 10 kHz using the inbuilt Bessel filter of the Axopatch. The G and inner diameter (d_i) are related through^{21,51}

$$d_i = \frac{4Gl}{\pi g d_b} \quad (1)$$

where l is the length of the conical pore (taper length), d_b is the diameter of the capillary at the beginning of the conical taper, and g is the measured conductivity of the ionic solution. The l was recorded using an optical microscope.

3.5.2 Electrolyte Preparation

All KCl (409316-100G, Sigma-Aldrich) electrolytes were prepared using DI water and buffered at pH \sim 7.4 using Tris-EDTA (BP2475-500, Thermo Fisher). Both pH and conductivity of the final solutions were measured using AB200 pH/Conductivity Benchtop Meter (Fisher Scientific) at room temperature. All solutions were filtered using 0.2-micron syringe filters (S6596FMOSK, Thermo Fisher Scientific) prior to nanopore experiments.

3.5.3 Biomolecule Preparation and Translocation Experiments

The Cas9 mutant, Cas9d10a, was purchased from New England BioLabs (M0650S) and the sgRNAs were purchased by Synthego (custom made, protocol can be found in Appendix B.S5). The reaction and incubation procedures were modeled after a protocol provided by New England Biolabs. Reagents including nuclease-free water, buffer, sgRNA, and Cas9d10a were pre-incubated together at 25°C for 10 minutes. Afterward, λ -DNA (N3011S, New England BioLabs) was added to the mixture and the entire solution was left to incubate at 37°C for 30 minutes. Both concentrations of sgRNA and Cas9d10a were at 30 nM and the DNA concentration was at 3 nM. This was done to ensure that only two populations: (1) Cas9d10a + sgRNA and (2) Cas9d10a + sgRNA + DNA were within

the nanopore. The sequence of the sgRNA that was used is as follows: AGCAGUCCAGCACAAUCGA.

All electrical data were acquired using freshly prepared Ag/AgCl electrodes. Electrodes were constructed using silver wires soaked in bleach overnight (~8 hours) followed by thorough rinsing with water to remove any residual bleach. Fabricated nanopores were then backfilled with either the electrolyte solution alone or electrolyte + analyte solution. Afterward, the nanopores were inspected using an optical microscope for any irregularities. Once the nanopores pass the visual inspection, they are then secured onto a head stage with electrodes connecting to the Axopatch 200B. The gain was optimized prior to recording. The λ -DNA was used as supplied and diluted to a final concentration of ~500 pM with the electrolyte of interest. Additionally, the M13mp18 ssDNA and dsDNA (N4040S and N4018S, NE BioLabs) were diluted to a final concentration of 500 pM.

3.5.4 Data Analysis and Machine Learning

All events were analyzed using custom-made MATLAB scripts as previously. A custom machine learning algorithm was used to train and classify events based on their unique current signatures. Specifically, linear support vectors with three classes were used to categorize different DNA configurations. Default kernel functions (linear) were utilized to divide the spaces between populations. In each condition presented, it is possible to detect various DNA configurations such as linear, partially folded, and fully folded DNA. Reports of different DNA configurations have been witnessed using high ionic strength conditions with both planar nanopores^{8,22,23,52} and nanocapillaries²¹.

3.6 References

1. Freedman, K. J., Haq, S. R., Edel, J. B., Jemth, P. & Kim, M. J. Single molecule unfolding and stretching of protein domains inside a solid-state nanopore by electric field. *Scientific reports* **3**, 1–8 (2013).
2. Saharia, J. *et al.* Molecular-level profiling of human serum transferrin protein through assessment of nanopore-based electrical and chemical responsiveness. *ACS nano* **13**, 4246–4254 (2019).
3. Karawdeniya, B. I. *et al.* Adeno-associated virus characterization for cargo discrimination through nanopore responsiveness. *Nanoscale* **12**, 23721–23731 (2020).
4. Karawdeniya, B. I., Bandara, Y. N. D., Nichols, J. W., Chevalier, R. B. & Dwyer, J. R. Surveying silicon nitride nanopores for glycomics and heparin quality assurance. *Nature communications* **9**, 1–8 (2018).
5. Li, J., Gershow, M., Stein, D., Brandin, E. & Golovchenko, J. A. DNA molecules and configurations in a solid-state nanopore microscope. *Nature Materials* **2**, 611–615 (2003).
6. Bell, N. A. W. & Keyser, U. F. Digitally encoded DNA nanostructures for multiplexed, single-molecule protein sensing with nanopores. *Nature Nanotechnology* **11**, 645–651 (2016).
7. Liu, K. *et al.* Detecting topological variations of DNA at single-molecule level. *Nature Communications* **10**, 3 (2019).
8. Plesa, C. *et al.* Direct observation of DNA knots using a solid-state nanopore. *Nature Nanotech* **11**, 1093–1097 (2016).
9. Sze, J. Y. Y., Ivanov, A. P., Cass, A. E. G. & Edel, J. B. Single molecule multiplexed nanopore protein screening in human serum using aptamer modified DNA carriers. *Nat Commun* **8**, 1552 (2017).
10. Dekker, C. Solid-state nanopores. *Nature Nanotechnology* **2**, 209–215 (2007).
11. Smeets, R. M. M., Keyser, U. F., Dekker, N. H. & Dekker, C. Noise in solid-state nanopores. *PNAS* **105**, 417–421 (2008).
12. Smeets, R. M. M. *et al.* Salt Dependence of Ion Transport and DNA Translocation through Solid-State Nanopores. *Nano Lett.* **6**, 89–95 (2006).

13. Nouri, R., Tang, Z. & Guan, W. Quantitative Analysis of Factors Affecting the Event Rate in Glass Nanopore Sensors. *ACS Sens.* **4**, 3007–3013 (2019).
14. Wanunu, M., Morrison, W., Rabin, Y., Grosberg, A. Y. & Meller, A. Electrostatic focusing of unlabelled DNA into nanoscale pores using a salt gradient. *Nature Nanotech* **5**, 160–165 (2010).
15. Vu, T. *et al.* Employing LiCl salt gradient in the wild-type α -hemolysin nanopore to slow down DNA translocation and detect methylated cytosine. *Nanoscale* **11**, 10536–10545 (2019).
16. Saharia, J., Bandara, Y. M. N. D. Y. & Kim, M. J. Investigating protein translocation in the presence of an electrolyte concentration gradient across a solid-state nanopore. *ELECTROPHORESIS n/a*,.
17. Lan, W.-J., Kubeil, C., Xiong, J.-W., Bund, A. & White, H. S. Effect of Surface Charge on the Resistive Pulse Waveshape during Particle Translocation through Glass Nanopores. *J. Phys. Chem. C* **118**, 2726–2734 (2014).
18. Luo, L., Holden, D. A. & White, H. S. Negative Differential Electrolyte Resistance in a Solid-State Nanopore Resulting from Electroosmotic Flow Bistability. *ACS Nano* **8**, 3023–3030 (2014).
19. Ivanov, A. P. *et al.* On-Demand Delivery of Single DNA Molecules Using Nanopipets. *ACS Nano* **9**, 3587–3595 (2015).
20. Kalman, E. B., Sudre, O., Vlasiouk, I. & Siwy, Z. S. Control of ionic transport through gated single conical nanopores. *Anal Bioanal Chem* **394**, 413–419 (2009).
21. Steinbock, L. J., Otto, O., Chimere, C., Gornall, J. & Keyser, U. F. Detecting DNA Folding with Nanocapillaries. *Nano Lett.* **10**, 2493–2497 (2010).
22. Li, J., Gershow, M., Stein, D., Brandin, E. & Golovchenko, J. A. DNA molecules and configurations in a solid-state nanopore microscope. *Nature Materials* **2**, 611–615 (2003).
23. Storm, A. J., Chen, J. H., Zandbergen, H. W. & Dekker, C. Translocation of double-strand DNA through a silicon oxide nanopore. *Phys. Rev. E* **71**, 051903 (2005).
24. Das, S., Dubsy, P., van den Berg, A. & Eijkel, J. C. T. Concentration Polarization in Translocation of DNA through Nanopores and Nanochannels. *Phys. Rev. Lett.* **108**, 138101 (2012).

25. Wang, P. *et al.* Genome Editing for Cancer Therapy: Delivery of Cas9 Protein/sgRNA Plasmid via a Gold Nanocluster/Lipid Core–Shell Nanocarrier. *Adv Sci (Weinh)* **4**, (2017).
26. Yusko, E. C. *et al.* Controlling protein translocation through nanopores with bio-inspired fluid walls. *Nature Nanotech* **6**, 253–260 (2011).
27. Bandara, Y. M. N. D. Y., Farajpour, N. & Freedman, K. J. Nanopore Current Enhancements Lack Protein Charge Dependence and Elucidate Maximum Unfolding at Protein’s Isoelectric Point. *J. Am. Chem. Soc.* **144**, 3063–3073 (2022).
28. Larkin, J., Henley, R. Y., Muthukumar, M., Rosenstein, J. K. & Wanunu, M. High-Bandwidth Protein Analysis Using Solid-State Nanopores. *Biophysical Journal* **106**, 696–704 (2014).
29. Nir, I., Huttner, D. & Meller, A. Direct Sensing and Discrimination among Ubiquitin and Ubiquitin Chains Using Solid-State Nanopores. *Biophysical Journal* **108**, 2340–2349 (2015).
30. Arima, A. *et al.* Selective detections of single-viruses using solid-state nanopores. *Sci Rep* **8**, 16305 (2018).
31. Im, J., Lindsay, S., Wang, X. & Zhang, P. Single Molecule Identification and Quantification of Glycosaminoglycans Using Solid-State Nanopores. *ACS Nano* **13**, 6308–6318 (2019).
32. Xia, K. *et al.* Synthetic heparan sulfate standards and machine learning facilitate the development of solid-state nanopore analysis. *PNAS* **118**, (2021).
33. Lastra, L. S., Bandara, Y. M. N. D. Y., Nguyen, M., Farajpour, N. & Freedman, K. J. On the origins of conductive pulse sensing inside a nanopore. *Nat Commun* **13**, 2186 (2022).
34. Nguyen, G., Howorka, S. & Siwy, Z. S. DNA strands attached inside single conical nanopores: ionic pore characteristics and insight into DNA biophysics. *The Journal of membrane biology* **239**, 105–113 (2011).
35. Wang, V., Ermann, N. & Keyser, U. F. Current Enhancement in Solid-State Nanopores Depends on Three-Dimensional DNA Structure. *Nano Lett.* **19**, 5661–5666 (2019).
36. Wang, V., Ermann, N. & Keyser, U. F. Current enhancement in solid-state nanopores depends on three-dimensional DNA structure. *Nano letters* **19**, 5661–5666 (2019).

37. Zhang, Y. *et al.* Ionic current modulation from DNA translocation through nanopores under high ionic strength and concentration gradients. *Nanoscale* **9**, 930–939 (2017).
38. Ermann, N. *et al.* Promoting single-file DNA translocations through nanopores using electro-osmotic flow. *J. Chem. Phys.* **149**, 163311 (2018).
39. Chen, P. *et al.* Probing Single DNA Molecule Transport Using Fabricated Nanopores. *Nano Lett.* **4**, 2293–2298 (2004).
40. Manning, G. S. A procedure for extracting persistence lengths from light-scattering data on intermediate molecular weight DNA. *Biopolymers: Original Research on Biomolecules* **20**, 1751–1755 (1981).
41. Tsutsui, M. *et al.* Transverse electric field dragging of DNA in a nanochannel. *Sci Rep* **2**, 394 (2012).
42. Kesselheim, S., Müller, W. & Holm, C. Origin of Current Blockades in Nanopore Translocation Experiments. *Phys. Rev. Lett.* **112**, 018101 (2014).
43. He, Y., Tsutsui, M., Fan, C., Taniguchi, M. & Kawai, T. Controlling DNA Translocation through Gate Modulation of Nanopore Wall Surface Charges. *ACS Nano* **5**, 5509–5518 (2011).
44. Plesa, C. *et al.* Fast Translocation of Proteins through Solid State Nanopores. *Nano Lett.* **13**, 658–663 (2013).
45. Bell, N. A. W. & Keyser, U. F. Specific Protein Detection Using Designed DNA Carriers and Nanopores. *J. Am. Chem. Soc.* **137**, 2035–2041 (2015).
46. Weckman, N. E. *et al.* Multiplexed DNA Identification Using Site Specific dCas9 Barcodes and Nanopore Sensing. *ACS Sens.* **4**, 2065–2072 (2019).
47. Yang, W. *et al.* Detection of CRISPR-dCas9 on DNA with Solid-State Nanopores. *Nano Lett.* **18**, 6469–6474 (2018).
48. Mohanakumar, S., Luettmmer-Strathmann, J. & Wiegand, S. Thermodiffusion of aqueous solutions of various potassium salts. *J. Chem. Phys.* **154**, 084506 (2021).
49. Okur, H. I. *et al.* Beyond the Hofmeister Series: Ion-Specific Effects on Proteins and Their Biological Functions. *J. Phys. Chem. B* **121**, 1997–2014 (2017).
50. Raper, A. T., Stephenson, A. A. & Suo, Z. Functional Insights Revealed by the Kinetic Mechanism of CRISPR/Cas9. *J. Am. Chem. Soc.* **140**, 2971–2984 (2018).

51. DeSorbo, W. Ultraviolet effects and aging effects on etching characteristics of fission tracks in polycarbonate film. *Nuclear Tracks* **3**, 13–32 (1979).
52. Kumar Sharma, R., Agrawal, I., Dai, L., Doyle, P. S. & Garaj, S. Complex DNA knots detected with a nanopore sensor. *Nature Communications* **10**, 4473 (2019).

Chapter 4: Enhancing Peptide Length Discrimination by Integrating Denaturing Agents

4.1 Abstract

Due to their high sensitivity and selectivity, nanopores have emerged as a promising platform for detection of various biomolecules including proteins and peptides. Specifically, peptide length is a crucial parameter in the identification and characterization of protein samples and plays a critical role in a wide range of fields, from research to clinical diagnostics. Unlike their biological counterparts, solid-state nanopores have difficulties detecting small molecules, such as peptides, as the dwell times are extremely short. Additionally, the detection of peptides and proteins is complicated by their non-uniform charge and nonlinear structure. To combat these challenges, in this chapter we incorporate various denaturing agents to linearize and provide a uniformly negative charge to peptides suspended in solution. This methodology allows us to resolve peptide lengths with 20 amino acids resolution. Additionally, once the ratio of concentrations between analyte and denaturing solution is optimized, we see a signal to noise ratio of ~ 100 and can differentiate between various peptides based on their change in current. Overall, this demonstration of nanopore-based single molecule detection in denaturing solution paves the way for the development of new diagnostic tools, targeted therapies, and personalized medicine.

4.2 Introduction

Nanopores are tiny channels or holes that typically have diameters < 100 nm. These pores can be found in a variety of natural and synthetic materials, such as cell membranes (biological), thin films (planar), and quartz (nanopipette). While biological nanopores have been known for their sequencing abilities¹⁻³, solid-state nanopores are highly tunable⁴, thus lending themselves to be used when detecting larger molecules and complexes⁵⁻⁷. Nanopores have attracted significant attention in recent years for their potential use in a wide range of applications, including biosensing⁸, protein-drug interactions⁹, and protein fingerprinting¹⁰. One area where nanopores have shown particular promise is in the analysis of biomolecules such as proteins and peptides.

Proteins are essential molecules for life as they perform a wide range of functions, such as enzymatic reactions, signaling pathways, and immune responses. Their structure is crucial to their function and interactions with other molecules. Due to the complex structures of proteins, it is highly sought after to define their properties and structure in order to interpret their functions. Peptides, the building blocks of proteins, are small chains of amino acids strung together via peptide bonds to form a chain. The sequence of amino acids in the peptide chain determines the protein's unique structure and function. Once synthesized, the peptide chains may undergo various post-translational modifications, including folding and the addition of chemical groups, which further shape their final structure and function. The short chains of amino acids play a variety of roles in the body, including hormones, neurotransmitters, and signaling molecules. When combined with the single-molecule sensor, nanopores, the structure properties of the peptide can be

determined. By passing these molecules through a nanopore, researchers can gather information about their size, shape, and other physical properties, which can in turn provide insights into their structure and function.

Currently, there exist several approaches to characterize peptides and proteins such as mass spectrometry^{11,12}, ELISA¹³, real-time PCR¹⁴, immuno-staining¹⁵, and fluorescence spectroscopy¹⁶. However, these traditional techniques have their disadvantages. They provide information for a group of molecules, which could conceal any data about diverse populations in a sample. Moreover, these techniques often require high concentrations and are not always suitable to detect low-copy proteins, unlike nanopores which can detect concentrations in the femtomolar range¹⁷. Mass spectrometry, the established benchmark of protein and peptide analysis, incurs low signal-to-noise ratio for analytes present at low concentrations¹⁸ and are restricted to a dynamic range of $\sim 10^4$ to 10^5 for the most advanced devices¹⁹. Additionally, the dynamic range needed for human biofluids is near $\sim 10^9$ to ensure a comprehensive analysis of the vast range of protein concentrations found in human plasma²⁰. Thus, putting mass spectrometry at a disadvantage for examining autodigestion in the blood. Other techniques such as fluorescence necessitate the use of a fluorescent dye, which can influence protein properties. Furthermore, protein sensing frequently involves lengthy sample preparation procedures, which require a significant amount of chemicals or consumables to extract the target. Finally, the analysis of proteins usually involves costly facilities such as mass spectroscopy, NMR, or fluorescence. Therefore, a methodology is needed to observe low analyte concentrations and small sample volumes without labelling or sample preparation which alters protein function.

Nanopore-based single molecule detection works by passing individual molecules through a nanometer sized hole and measuring the changes in electrical current that occur. Often, when a translocating molecule passes through the pore opening, a decrease in current ensues (due to the blockage of ion flow at the pore aperture), similar to the Coulter-Counter principle. Because the current fluctuations are affected by the size, length, charge, and shape of the peptide²¹, researchers can use these measurements to determine the various properties of peptides with high accuracy and sensitivity. To date, there are many studies investigating peptides and their properties with biological nanopores²²⁻²⁵. Even though solid-state nanopores are more robust and tunable than their biological counterparts²⁶, smaller molecules pass through far too quickly, namely small proteins and peptides. To address these challenges, some of the following has been incorporated into nanopore detection such as: (1) usage of higher bandwidth instruments²⁷, (2) electroosmotic flow²⁸, (3) pressure^{29,30}, and (4) surface modifications to lengthen the dwell time³¹.

Despite these novel ideas and advancements, there have been scarce studies published in the field of quartz nanopipettes used to detect peptide length differences. Wang et. al. demonstrated the usage of resistive-pulse sensing of nanoparticles and particles with allergen epitope peptide layers using nanopipettes³². Recently, a study was published detailing nanopipettes detecting supercharged unstructured polypeptides fused with proteins (molecular carrier technique) can be used for protein sensing. Another study, albeit using biological nanopores, demonstrated a novel protocol that could quantify the number of cysteines in a peptide chain. In summary, while there has been progression in

characterizing peptides by their length, the work has been done with biological nanopore, and not solid-state. Additionally, the research performed with quartz nanopipettes generally uses peptides as a functional layer or as a conduit to detect other molecules.

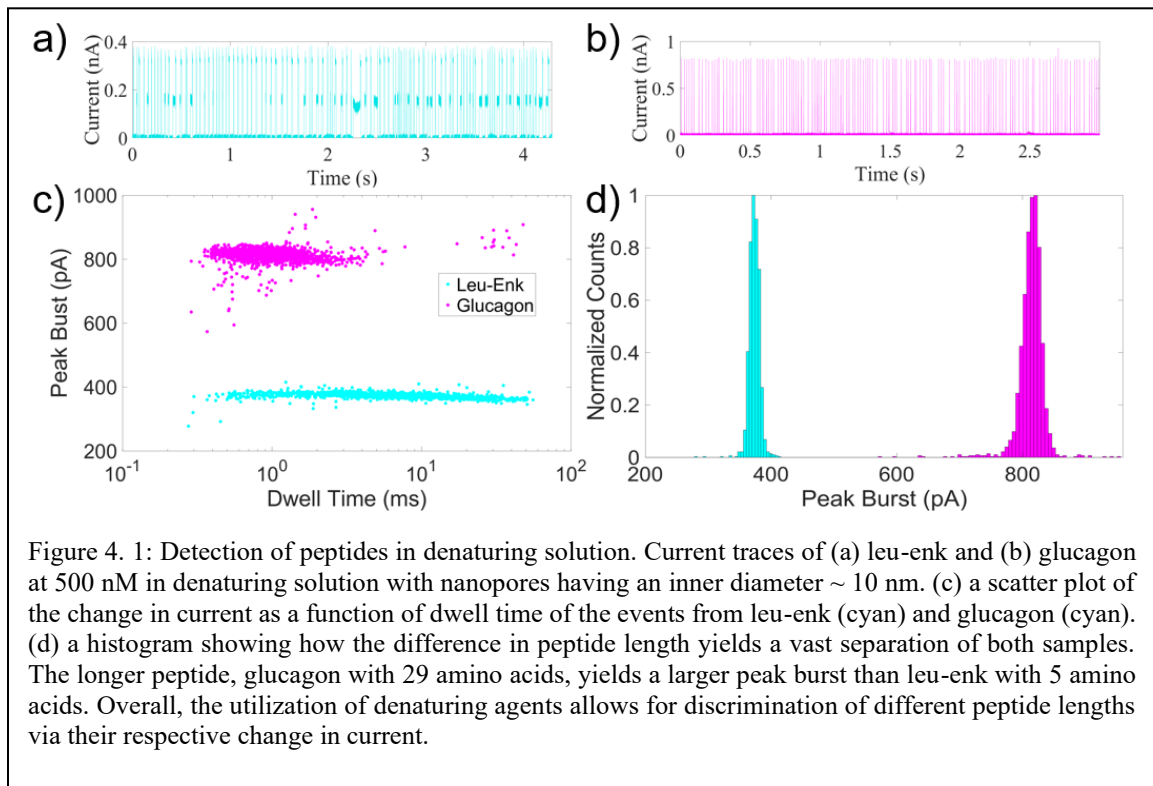
The incorporation of denaturing solutions has been previously reported³³⁻³⁵. Specifically, sodium dodecyl sulfate (SDS), is utilized for its denaturing properties as well as its coating abilities of the nanopore's inner walls³⁶. The other components of the denaturing solution used in this study, guanidinium hydrochloride (GuHCl) and dithiothreitol (DTT), have also been integrated into nanopore detection solutions to aid in unfolding and denaturing proteins^{37,38}. We decided to combine the aforementioned denaturing chemicals (SDS, GuHCl, and DTT) to decrease the effective pore diameter (SDS coating), provide a uniform negative charge, unfold, and negate any disulfide bridges to ensure the differences in event properties between the molecules were indicative of the length of the molecule.

The premise behind this aim was to transition away from detecting the protease itself (trypsin) to detecting the peptide fragments generated via trypsin. This would provide information regarding the protease's activity level by characterizing the quantity and size of the peptide fragments produced. The research detailed in this chapter leap the quartz nanopipette field forward by demonstrating how denaturing solutions can be implemented to detect length differences between peptides. Overall, nanopores are a powerful tool for analyzing biomolecules such as peptides, and their use is likely to continue to grow as researchers develop new and innovative ways to harness their unique properties.

4.3 Results and Discussion

4.3.1 Critical micelle concentration of sodium dodecyl sulfate

Sodium Dodecyl Sulfate (SDS) molecules can spontaneously form spherical micelles within a solution. The concentration in which micelles form is known as the critical micelle concentration (CMC). To address the challenge of linearizing and providing a uniform charge to peptides in solution, SDS was utilized. It is stated that the CMC in water is 8 mM³⁹ and the value decreases with the addition of salt.⁴⁰ With this in mind, we performed an assay with increasing concentrations of SDS in 1 M KCl to determine the usable concentration that did not yield any precipitation from the combination of KCl and SDS⁴¹. The working concentration of SDS used for this chapter was determined to be 1 mM.

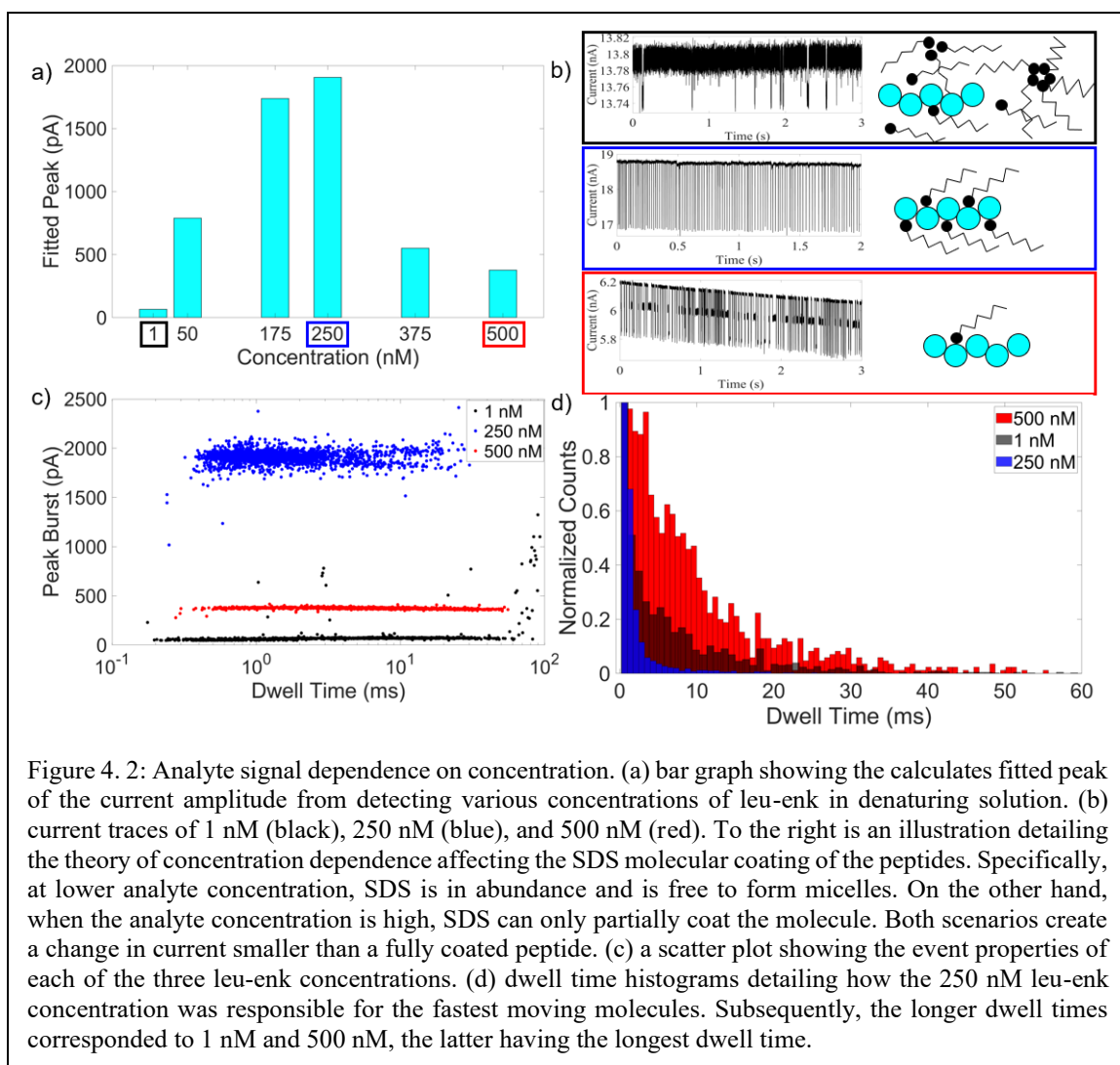


In addition to SDS, other denaturing agents were employed to assist in unfolding biomolecules and eliminating disulfide bridges, such as guanidine hydrochloride (GuHCl) and dithiothreitol (DTT). The concentration of GuHCl and DTT was determined to be 0.5 M and 50 mM, respectively after assays were completed with each in 1 M KCl. Lastly, sodium hydroxide (NaOH) was added to yield a pH of 10.5, as values above five do not influence CMC value of SDS⁴². Overall, the denaturing solution was determined via assays and prior literature to be: 1 M KCl, 1 mM SDS, 0.5 M GuHCl, 50 mM DTT, and 100 mM NaOH. Prior to usage with the nanopore, the solution was heated up to 95 C for five minutes following the protocol previously published³⁵.

4.3.2 Detection of Peptides in Denaturing Solution

With the denaturing solution developed, we first sought to detect peptides suspended in solution of known concentration and length. The peptides, leu-enkephalin (leu-enk) and glucagon, were exposed to denaturing solution which contain 5 and 29 amino acids in length, respectively. The concentrations of each peptide were maintained at 500 nM in denaturing solution. Because SDS molecules giving the peptides an overall negative charge, the applied voltage was +500 mV and the results can be seen in Figure 4.1 where glucagon is labelled in magenta and leu-enk is in cyan. In Figure 4.1a and 4.1b, the event traces are shown as changes in current as a function of time for leu-enk and glucagon, respectively. Each deviation from the baseline is designated as one event, meaning one molecule (peptide in this case) has translocated through the pore. There is a noticeable difference between the peak current amplitude of the events stemming from glucagon in comparison to those corresponding to leu-enk. Specifically, the change in current is higher

in glucagon than it is for leu-enk. This is more quantitatively shown in Figures 4.1c and 4.1d where 4.1c shows the change in current as a function of dwell time in milliseconds for each event and 4.1d displays the differences in peak distributions for the changes in current. The main difference between these two peptides is the length of amino acids that comprise them. Glucagon is the longer peptide, having 29 amino acids, while leu-enk contains 5 amino acids. The overall charges of the molecules are negative, given the treatment of SDS specifically. Therefore, we can conclude that the difference in current amplitude is



attributed to the length of the peptides. Specifically, glucagon contains more amino acids and shifts the current by ~ 800 pA upon translocation while leu-enk, having only five amino acids, yields ~ 370 pA displacement, a vast decrease. Hence, the denaturing solution provides peptide length information through the change in current as the peptides translocate the pore.

Following the peptide length characterization, we decided to delve into investigating the relationship between peptides and denaturing solution, SDS specifically. For this study, we varied the concentration of leu-enk while keeping the concentration of SDS in the denaturing solution constant. Leu-enk was diluted to 1, 50, 175, and 375 nM (the 500 nM condition had already been performed in the previous study). The results indicate that there is a concentration dependence between the analyte (leu-enk) and denaturing solution. In Figure 4.2a, the event information at each condition was extracted with a custom-made MATLAB script and the current amplitudes were found to fluctuate as a function of the analyte concentration. In more detail, the fitted peak of the current amplitudes exhibits a gaussian distribution in terms of the analyte concentration, where the extreme values (1 nM and 500 nM) produce the lowest changes in current. Meanwhile, at 250 nM, the fitted peak of the current amplitudes is at its highest.

To provide additional support, Figure 4.2b shows the current traces of both extreme conditions (1 nM and 500 nM in black and blue, respectively) as well as the 250 nM conditions (red). On the right side, there are three illustrations, corresponding to the three different analyte concentrations, depicting the theory behind the differences in current amplitude. To reiterate, the concentration of SDS in the denaturing solution is kept at the

same value, 1 mM, for each experiment. In the highest analyte concentration, 500 nM, we speculate that there is an insufficient number of SDS molecules to fully coat the peptide. Because of this, the diameter of the translocating molecule is less than the 250 nM condition. The illustration (within the red box) in Figure 4.2b depicts this scenario. This would explain why the change in current amplitude for the 500 nM leu-enk condition is less than the 250 nM condition. For the lowest concentration, 1 nM, we suspect that there is surplus of SDS molecules in the solution because there is a small quantity of analyte that SDS can bind itself onto. Because of this, the formation of micelles may be energetically favorable over the binding to the peptide itself, which could explain the few large events seen in the scatter plot of Figure 4.2c. Lastly, the ratio between the SDS molecules and the peptide is optimized in the 250 nM concentration, meaning that a fully uniform coating via SDS occurs and no micelle formation is present, which is depicted in the blue box.

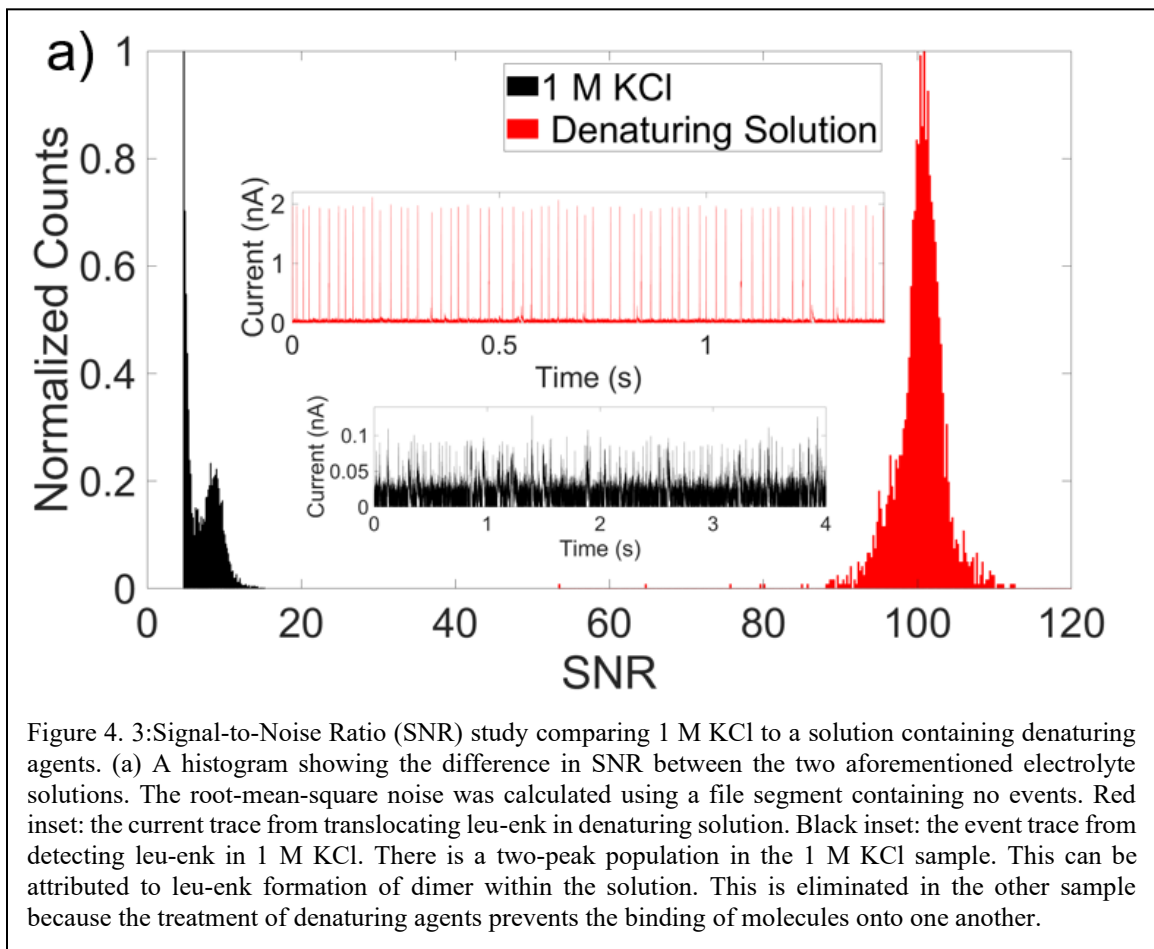
In Figure 4.2c, the same three conditions are further examined in terms of their respective current amplitudes and dwell times. Strikingly, the peak burst of the entire 250 nM population is over four times greater than the other two conditions. Additionally, the dwell times of each of the conditions differ substantially as seen in Figure 4.2d. The dwell times corresponding to the 250 nM concentration were the fastest while the other two concentrations had longer dwell times, the 500 nM condition exhibiting the longest out of the three. We theorize that this can also be attributed to SDS coating of the peptide. There is a certain value in which the quantity of SDS molecules and peptides are at its optimum, meaning that the entirety of the peptide is coated and there are not any free SDS molecules and/or micelles forming within the solution. This is one of the reasons why the 250 nM

condition is responsible for the largest change in current, because SDS is completely coating an additional layer on the peptide itself, allowing the peptide to transiently block a substantial amount of the ion flow, resulting in a large current amplitude. SDS is known to give all molecules a negative charge which is why it is most widely used in gel electrophoresis. Theoretically, a fully coated peptide molecule will have a more negative charge in comparison to a partially coated, or even uncoated, molecule. When a positive voltage is applied, negatively charged molecules will sense the voltage application, and begin their journey towards that positive pole. With this in mind, we hypothesized that the 250 nM concentration is responsible for having the most negative charge, due to the full coating of SDS, resulting in a faster translocation time. As for the low and high analyte concentration, it is possible that SDS is in abundance (leading to partial coating due to the formation of micelles) and in scarcity, giving the molecule a weaker negative charge, respectively.

4.3.3 Signal-to-Noise Study in Denaturing Solution

One of the most commonly used electrolyte solution is 1 M KCl. This is often seen as the standardized buffer solution in which alternative experimental results are compared to. Some of the reasons as to why 1 M KCl has become one of the most prevalent buffers for nanopore sensing are: (1) KCl dissociates into K^+ and Cl^- ions which (at 1 M) creates an ionic strength that reduces electrostatic screening, (2) it is highly compatible with a wide range of biomolecules, and (3) it is relatively non-toxic, making it a safer choice when working with biological samples.

There are a variety of parameters that affect the signal (either change in current or dwell time) of the translocating molecule such as pH, pore diameter, method of translocation, starting location of the analyte, electrolyte concentration, and alkali chloride type^{28,43–45}. One metric that does not fall into this category is analyte concentration. Because nanopore sensing is a highly stochastic process, molecules diffuse within the solution until they enter what is known as the capture zone: the volume in which the electric field is sensed. Once the molecule diffuses into the capture zone, it is electrochemically driven to enter the nanopore. To our knowledge, there has yet to have been a study indicating that the concentration of analyte has any relationship to the signal generated.



Although, it is known that higher concentrations can lead to increased event rates and vice versa⁴⁶. The electrolyte concentration, however, does affect the signal of the molecule. This is because the electrolyte concentration directly affects the number of ions that are present in an open-pore scenario. When a molecule transiently blocks this flow, the signal will reflect that change in current based off the quantity of ions that are within the aperture of the pore (electrolyte concentration).

Because of this signal dependence on analyte concentration, we then performed an experiment using the same peptide, leu-enk, in 1 M KCl to compare to the leu-enk translocations using denaturing solution. The same voltage polarity was applied (+500 mV for denaturing solution and -500 mV for 1 M KCl) and the same pore size was used (~10 nm diameter). The results can be seen in Figure 4.3. which shows a histogram of the SNR of both conditions. The SNR was calculated by extracting the current amplitudes of each event and then dividing those values by the root-mean-square noise ($\text{RMS}_{\text{noise}}$) which was calculated by selecting a portion of the data file that contained no events. The SNR of the leu-enk translocations in 1 M KCl and denaturing solution can be found in black and red, respectively. The inset in the middle of Figure 4.3a shows the current traces corresponding to both conditions as well.

An interesting note is that there is a two-peak distribution for the 1 M KCl translocations, and a singular peak in the denaturing solution translocations. It has been previously shown that leu-enk has a tendency to form dimers in solution⁴⁷⁻⁴⁹. We believe that this two peak distribution is reflective of leu-enk constructing dimers in the 1 M KCl condition. Because the solution is 1 M KCl, there is no reason for molecules to resist the

formation of secondary structures. Additionally, this is a feature that is not seen when using the denaturing solution, as demonstrated with the singular peak in Figure 4.3. With the treatment of denaturing agents (likely the full coating of SDS), the molecule exhibits a negative charge, which will oppose binding to other negatively charged molecules. Going back to the previous example, in the 1 M KCl case, the peptide chain contains amino acids that are negatively-, neutrally-, and positively-charged. This means that the likelihood of oppositely charged regions of the peptide chain self-assembling into dimers is high. With the results of this study, we have discovered that, not only is the SNR of events in the denaturing solution surpassing 100, but it also prevents the formation of secondary structures of non-uniformly charged molecules.

4.3.4 Multiplexed Sensing of Peptides Using a Peptide Ladder

At this point, we have described how utilizing denaturing solution can provide information surrounding the lengths of peptides, increase SNR drastically, and prevent dimerization formation. In order to improve the throughput and efficiency of peptide detection, it was desirable to detect multiple peptides in a solution with a single nanopore. Therefore, in this section, we aimed to expand the detection capabilities of our nanopore sensor in denaturing solution by investigating its ability to provide peptide length information of differently sized peptides. Here, we describe the results of utilizing six differently sized peptides (peptide ladder) and peptide ladder spiked with one additional peptide of similar length in denaturing solution.

After the analyte concentration series, we arrived at the conclusion that the optimal concentration of peptides in denaturing solution is 140 pg/ μ L (leu-enk molarity 250 nM). When preparing the peptide ladder in denaturing solution, we diluted the ladder down to 140 pg/ μ L and fabricated a nanopore with 10 nm in diameter. The results can be seen in Figure 4.4a. Upon molecular translocation, the data points that comprised each event were plotted into the all points histogram. A final step of normalization of both the x-and y-axis was performed to eliminate any baseline contribution and account for differences in the magnitude of the peaks, respectively. An interesting feature of the all points histogram is the presence of multiple peaks. We hypothesize that the \sim 6 peaks in the all points histogram correspond to the six differently sized peptides in the peptide ladder. Our previous results when researching glucagon and leu-enk indicated a positive relationship between peptide length and current amplitude, meaning longer peptide chains yielded larger changes in current. In this case, the shortest peptide in the ladder (9 amino acids) is thought to correspond to the first, largest peak (shortest change in current) and the longest peptide (247 amino acids) with the right most peak (largest change in current). When studying the peptide ladder, this theory seems to hold true due to the noticeable multi-peak population.

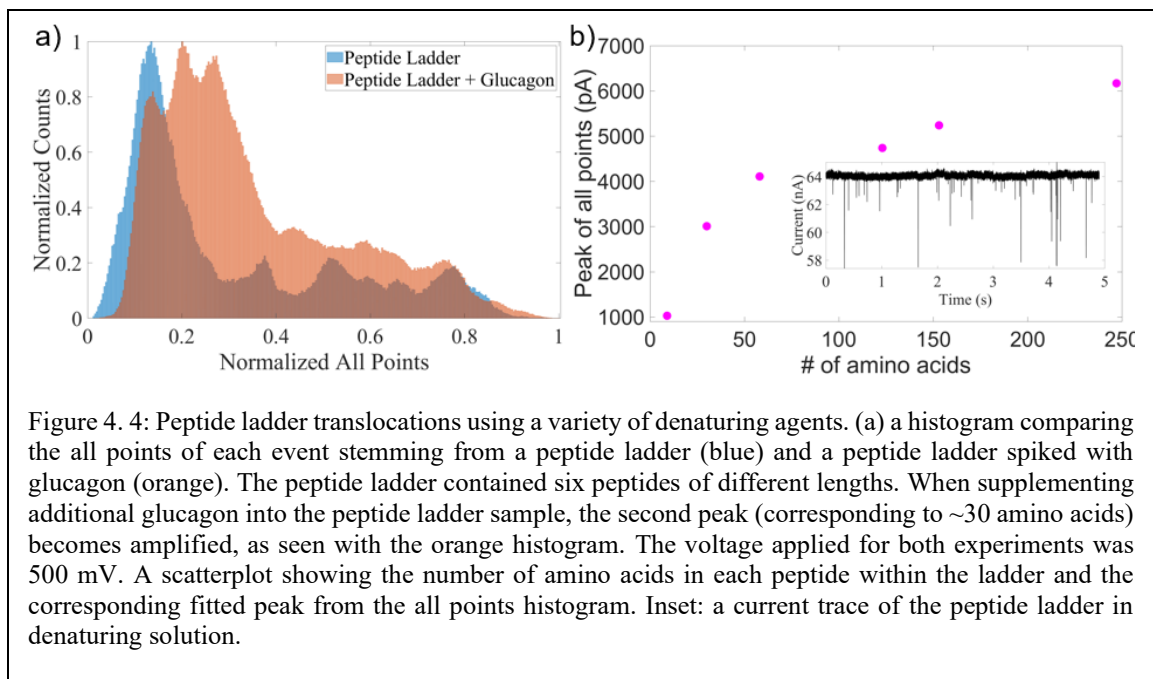


Figure 4. 4: Peptide ladder translocations using a variety of denaturing agents. (a) a histogram comparing the all points of each event stemming from a peptide ladder (blue) and a peptide ladder spiked with glucagon (orange). The peptide ladder contained six peptides of different lengths. When supplementing additional glucagon into the peptide ladder sample, the second peak (corresponding to ~ 30 amino acids) becomes amplified, as seen with the orange histogram. The voltage applied for both experiments was 500 mV. A scatterplot showing the number of amino acids in each peptide within the ladder and the corresponding fitted peak from the all points histogram. Inset: a current trace of the peptide ladder in denaturing solution.

In the same figure, we show the results of a similar experiment with the same pore size. The peptide ladder contained peptides with lengths of: 9, 30, 58, 123, 153, and 247 amino acids. In this study, we supplemented the ladder with an additional peptide, glucagon, to increase the concentration of the second shortest peptide within the ladder. Here, we are assuming that by adding a surplus of glucagon with 29 amino acids to the peptide ladder, the 30 amino acid peptide and glucagon will increase the second peak in the all points distribution. The results, in the form of the all points histogram, are also shown in Figure 4.4a. Fascinatingly, there is an overall increase in the second peak amplitude, which we consider to be indicative of the additional 29-30 amino acid peptides. In Figure 4.4b we relate the peptide length to the fitted peak of the all points histogram for the peptide ladder. Similar to the experiments with glucagon and leu-enk, we suspect the change in current to be indicative of the peptide length, meaning the largest change in current corresponds to the longest peptide chain, and vice versa. In the inset, the current

trace of the peptide ladder in denaturing solution shows the variance in event peaks for the differently sized peptides. This section highlights the potential of our platform to detect and discriminate the size differences of peptides in complex mixtures. Moreover, they demonstrate the flexibility and sensitivity in adapting to different experimental conditions and optimizing the detection of specific molecules.

4.4 Conclusion

In this chapter, we formulated a novel sensing solution with a highly probable potential of utilizing for protein fingerprinting. By incorporating 1 M KCl, SDS, DTT, and GuHCl in a slightly alkaline environment, the resulting solution allows for the linearization and negative polarization of molecules. Subsequently, the change in current positively correlates to the length of the translocating peptide. Moreover, this methodology is capable of detecting small oligopeptides (five amino acids in length) and differently sized peptides in a heterogenous mixture. As shown with leu-enk, glucagon, and then with peptide ladders, both the change in current and the all points method can be used to discriminate between peptides of different sizes. Another advantageous reason to employ usage of the denaturing solution is the extremely high SNR, surrounding a value of 100. When compared to the gold standard sensing solution, not only is the denaturing solution SNR greater, but it also eliminates the formation of secondary configurations. The study using leu-enk in both solutions showed that the 1 M KCl condition had the formation of two peaks, corresponding to dimerization of the peptides.

While there are genuine benefits to utilizing this solution, we have discovered that the signal is highly dependent upon the ratio of analyte to SDS concentration. Such that, there is an optimal analyte concentration in which SDS can coat the molecule entirely without the formation of micelles. Studying leu-enk at various concentrations introduced the idea that SDS may or may not be able to fully coat the entire molecule. To optimize the SNR, the concentration of analyte should be known to perform the corresponding dilution. Because of this and knowing that in the next chapter we will be working with extremely heterogenous solution of unknown concentrations, we decided to pivot away from utilizing denaturing solution and work under conditions where no concentration optimization need to occur. Overall, the results of this chapter demonstrate a strong approach to detecting length differences in amino acids and take a step towards peptide sequencing using quartz nanopipettes.

4.5 Materials and Methods

4.5.1 Nanopore Preparation

Quartz capillaries (Sutter Instruments, QF100-70-7.5) of 7.5 cm in length, 1.00 mm in outer diameter, and 0.70 mm inner diameter were plasma cleaned for a minimum of five minutes. Afterwards, the capillaries were transported to the P-2000 laser puller (Sutter Instrument Co.) where a CO₂ laser directed into the center of the capillary length created two identical nanopipettes. and a one-line protocol was used: (1) HEAT: 630; FIL: 4; VEL: 61; DEL: 145; PULL: either 210 or 220. This resulted in two identical, conical nanopores within a heat duration of approximately 4.8 s.

Silver electrodes wires were cut into inch long fragments and then placed into a bleach bath overnight. Afterwards, the electrodes were rinsed DI water. Nanopipettes were then backfilled with electrolyte solution. Prior to attaching the sample and nanopipette to the Axopatch head stage, the nanopipettes were observed under an optical microscope. This was done to check for any breaks or bubbles in the nanopore tip. After inspection, the nanopore and sample were secured within the head stage in a metal box and connected with wires attached to silver chloride electrodes.

4.5.2 Denaturing Solution and Preparation

A denaturing solution was created to contain 1 M KCl (Thermo Fisher, P217-500), 1 mM SDS (Thermo Fisher, BP2436-200), 50 mM DTT (Thermo Fisher, BP172-5), 100 mM NaOH (Thermo Fisher, S318-500), and 0.5 M GuHCl (Thermo Fisher, BP178-500). These reagents were chosen specifically for the following properties: high salt concentration to utilize electrophoretic forces, give a uniform negative charge, break any disulfide bridges, increasing pH to aid in preventing aggregation, and cause unfolding, respectively. Lastly, the solution was heated up to 95°C for 5 minutes to eliminate any precipitates that may have formed. The pH of this solution was determined to be 8.75 using AB200 pH/Conductivity Benchtop Meter (Fisher Scientific). Glucagon (69271) and leucine-enkephalin (AAJ66801LB0) were purchased from Thermo Fisher and the peptide ladder (Ultra-low range Molecular Weight Marker 1,060-26,600, M3546) was purchased from Sigma-Aldrich.

4.5.3 Data Acquisition and Analysis

The Axopatch 200B patch-clamp amplifier (Molecular Devices) in voltage-clamp mode was used to measure the current fluctuations in time. Prior to acquisition, the gain was optimized and the signal was filtered with a low-pass Bessel filter at 10 kHz and digitized using the Digidata 1550B (Molecular Devices). The data was acquired at a frequency of 250 kHz. A custom-made MATLAB script was utilized to analyze the events acquired via Axopatch 200B.

4.6 References

1. Butler, T. Z., Pavlenok, M., Derrington, I. M., Niederweis, M. & Gundlach, J. H. Single-molecule DNA detection with an engineered MspA protein nanopore. *Proceedings of the National Academy of Sciences* **105**, 20647–20652 (2008).
2. Stoddart, D., Heron, A. J., Mikhailova, E., Maglia, G. & Bayley, H. Single-nucleotide discrimination in immobilized DNA oligonucleotides with a biological nanopore. *Proceedings of the National Academy of Sciences* **106**, 7702–7707 (2009).
3. Franceschini, L., Mikhailova, E., Bayley, H. & Maglia, G. Nucleobase recognition at alkaline pH and apparent pKa of single DNA bases immobilised within a biological nanopore. *Chem. Commun.* **48**, 1520–1522 (2012).
4. Chen, Q. & Liu, Z. Fabrication and Applications of Solid-State Nanopores. *Sensors* **19**, 1886 (2019).
5. Xia, Z., Lin, C.-Y. & Drndić, M. Protein-enabled detection of ibuprofen and sulfamethoxazole using solid-state nanopores. *PROTEOMICS* **22**, 2100071 (2022).
6. Zhao, X. *et al.* Translocation of tetrahedral DNA nanostructures through a solid-state nanopore. *Nanoscale* **11**, 6263–6269 (2019).
7. Kong, J., Bell, N. A. W. & Keyser, U. F. Quantifying Nanomolar Protein Concentrations Using Designed DNA Carriers and Solid-State Nanopores. *Nano Lett.* **16**, 3557–3562 (2016).
8. Sze, J. Y. Y., Ivanov, A. P., Cass, A. E. G. & Edel, J. B. Single molecule multiplexed nanopore protein screening in human serum using aptamer modified DNA carriers. *Nat Commun* **8**, 1552 (2017).
9. Jeong, K.-B. *et al.* Single-molecule fingerprinting of protein-drug interaction using a funneled biological nanopore. *Nat Commun* **14**, 1461 (2023).
10. Lucas, F. L. R., Versloot, R. C. A., Yakovlieva, L., Walvoort, M. T. C. & Maglia, G. Protein identification by nanopore peptide profiling. *Nat Commun* **12**, 5795 (2021).
11. Walther, T. C. & Mann, M. Mass spectrometry–based proteomics in cell biology. *Journal of Cell Biology* **190**, 491–500 (2010).
12. Maffioli, E. *et al.* High-Resolution Mass Spectrometry-Based Approaches for the Detection and Quantification of Peptidase Activity in Plasma. *Molecules* **25**, 4071 (2020).

13. Abe, H. *et al.* Preparation of recombinant MK-1/Ep-CAM and establishment of an ELISA system for determining soluble MK-1/Ep-CAM levels in sera of cancer patients. *Journal of Immunological Methods* **270**, 227–233 (2002).
14. Liu, J. *et al.* Novel, fluorescent, SSB protein chimeras with broad utility. *Protein Science* **20**, 1005–1020 (2011).
15. Maity, B., Sheff, D. & Fisher, R. A. Chapter 5 - Immunostaining: Detection of Signaling Protein Location in Tissues, Cells and Subcellular Compartments. in *Methods in Cell Biology* (ed. Conn, P. M.) vol. 113 81–105 (Academic Press, 2013).
16. Chen, Y. & Barkley, M. D. Toward understanding tryptophan fluorescence in proteins. *Biochemistry* **37**, 9976–9982 (1998).
17. Freedman, K. J. *et al.* Nanopore sensing at ultra-low concentrations using single-molecule dielectrophoretic trapping. *Nature Communications* **7**, 10217 (2016).
18. Domon, B. & Aebersold, R. Options and considerations when selecting a quantitative proteomics strategy. *Nat Biotechnol* **28**, 710–721 (2010).
19. Zubarev, R. A. The challenge of the proteome dynamic range and its implications for in-depth proteomics. *PROTEOMICS* **13**, 723–726 (2013).
20. A cast of thousands. *Nat Biotechnol* **21**, 213–213 (2003).
21. Varongchayakul, N., Song, J., Meller, A. & W. Grinstaff, M. Single-molecule protein sensing in a nanopore: a tutorial. *Chemical Society Reviews* **47**, 8512–8524 (2018).
22. Li, S., Cao, C., Yang, J. & Long, Y.-T. Detection of Peptides with Different Charges and Lengths by Using the Aerolysin Nanopore. *ChemElectroChem* **6**, 126–129 (2019).
23. Hu, Z.-L., Huo, M.-Z., Ying, Y.-L. & Long, Y.-T. Biological Nanopore Approach for Single-Molecule Protein Sequencing. *Angewandte Chemie* **133**, 14862–14873 (2021).
24. Mereuta, L. *et al.* A Nanopore Sensor for Multiplexed Detection of Short Polynucleotides Based on Length-Variable, Poly-Arginine-Conjugated Peptide Nucleic Acids. *Anal. Chem.* **94**, 8774–8782 (2022).
25. Sutherland, T. C. *et al.* Structure of Peptides Investigated by Nanopore Analysis. *Nano Lett.* **4**, 1273–1277 (2004).
26. Dekker, C. Solid-state nanopores. *Nature Nanotechnology* **2**, 209–215 (2007).

27. Larkin, J., Henley, R. Y., Muthukumar, M., Rosenstein, J. K. & Wanunu, M. High-Bandwidth Protein Analysis Using Solid-State Nanopores. *Biophysical Journal* **106**, 696–704 (2014).
28. Lastra, L. S., Bandara, Y. M. N. D. Y., Sharma, V. & Freedman, K. J. Protein and DNA Yield Current Enhancements, Slow Translocations, and an Enhanced Signal-to-Noise Ratio under a Salt Imbalance. *ACS Sens.* **7**, 1883–1893 (2022).
29. Sharma, V., Farajpour, N., Lastra, L. S. & Freedman, K. J. DNA Coil Dynamics and Hydrodynamic Gating of Pressure-Biased Nanopores. *Small* **18**, 2106803 (2022).
30. Lu, B. *et al.* Pressure-Controlled Motion of Single Polymers through Solid-State Nanopores. *Nano Lett.* **13**, 3048–3052 (2013).
31. Yusko, E. C. *et al.* Controlling protein translocation through nanopores with bio-inspired fluid walls. *Nature Nanotech* **6**, 253–260 (2011).
32. Wang, Y. *et al.* Resistive-pulse measurements with nanopipettes: detection of Au nanoparticles and nanoparticle -bound anti-peanut IgY. *Chemical Science* **4**, 655–663 (2013).
33. Soni, N., Freundlich, N., Ohayon, S., Huttner, D. & Meller, A. Single-File Translocation Dynamics of SDS-Denatured, Whole Proteins through Sub-5 nm Solid-State Nanopores. *ACS Nano* **16**, 11405–11414 (2022).
34. Chinappi, M. & Cecconi, F. Protein sequencing via nanopore based devices: a nanofluidics perspective. *J. Phys.: Condens. Matter* **30**, 204002 (2018).
35. Restrepo-Pérez, L., John, S., Aksimentiev, A., Joo, C. & Dekker, C. SDS-assisted protein transport through solid-state nanopores. *Nanoscale* **9**, 11685–11693 (2017).
36. M. Eggenberger, O., Ying, C. & Mayer, M. Surface coatings for solid-state nanopores. *Nanoscale* **11**, 19636–19657 (2019).
37. Sun, H. *et al.* Nanopore single-molecule biosensor in protein denaturation analysis. *Analytica Chimica Acta* **1243**, 340830 (2023).
38. Wan, X., Wang, D. & Liu, S. Fluorescent pH-Sensing Organic/Inorganic Hybrid Mesoporous Silica Nanoparticles with Tunable Redox-Responsive Release Capability. *Langmuir* **26**, 15574–15579 (2010).
39. Hammouda, B. Temperature Effect on the Nanostructure of SDS Micelles in Water. *J Res Natl Inst Stand Technol* **118**, 151–167 (2013).
40. Niraula, T. P., Bhattarai, A. & Chatterjee, S. K. Critical micelle concentration of sodium dodecyl sulphate in pure water and in methanol-water mixed solvent media

in presence and absence of KCl by surface tension and viscosity methods. *BIBECHANA* **11**, 103–112 (2014).

41. Hejazi, S. M., Erfan, M. & Mortazavi, S. A. Precipitation Reaction of SDS and Potassium Salts in Flocculation of a Micronized Megestrol Acetate Suspension. *Iran J Pharm Res* **12**, 239–246 (2013).
42. Rahman, A. & Brown, C. W. Effect of pH on the critical micelle concentration of sodium dodecyl sulphate. *Journal of Applied Polymer Science* **28**, 1331–1334 (1983).
43. Bandara, Y. M. N. D. Y., Farajpour, N. & Freedman, K. J. Nanopore Current Enhancements Lack Protein Charge Dependence and Elucidate Maximum Unfolding at Protein's Isoelectric Point. *J. Am. Chem. Soc.* **144**, 3063–3073 (2022).
44. Lastra, L. S., Bandara, Y. M. N. D. Y., Nguyen, M., Farajpour, N. & Freedman, K. J. On the origins of conductive pulse sensing inside a nanopore. *Nat Commun* **13**, 2186 (2022).
45. Kowalczyk, S. W., Wells, D. B., Aksimentiev, A. & Dekker, C. Slowing down DNA Translocation through a Nanopore in Lithium Chloride. *Nano Lett.* **12**, 1038–1044 (2012).
46. Nouri, R., Tang, Z. & Guan, W. Quantitative Analysis of Factors Affecting the Event Rate in Glass Nanopore Sensors. *ACS Sens.* **4**, 3007–3013 (2019).
47. Cai, X. & Dass, C. Structural characterization of methionine and leucine enkephalins by hydrogen/deuterium exchange and electrospray ionization tandem mass spectrometry. *Rapid Communications in Mass Spectrometry* **19**, 1–8 (2005).
48. Milosavljević, A. R. *et al.* VUV photofragmentation of protonated leucine-enkephalin peptide dimer below ionization energy. *Eur. Phys. J. D* **68**, 68 (2014).
49. Milosavljević, A. R., Cerovski, V. Z., Canon, F., Nahon, L. & Giuliani, A. Nanosolvation-Induced Stabilization of a Protonated Peptide Dimer Isolated in the Gas Phase. *Angewandte Chemie International Edition* **52**, 7286–7290 (2013).

Chapter 5: Real-time, Nanopore-Based Monitoring of Enzymatically Active Protease in Whole Blood

5.1 Abstract

In this chapter, we demonstrate the feasibility of utilizing nanopores as a diagnostic device. The robust single-molecule sensor, nanopores, has been used to detect a wide range of biomolecules at low concentrations, enabling the potentiality of becoming clinically relevant. The incorporation of nanopores in a lab-on-a-chip device comes close to this goal without the need for labelling or pre-treatment. One of the major implications in employing nanopores in complex solutions is that they can contain various types of non-target molecules that can interact with and accumulate inside the system, thereby reducing the efficiency and sensitivity of the detection method. Because this can lead to inaccurate measurements, pre-treatment methods or labelling techniques are often required when working with biological samples. Here, we demonstrate a fully modifiable and inexpensive detection platform to monitor and quantify the peptide fragments generated from trypsin digestion, a crucial phenomenon occurring under a state of autodigestion without any pre-treatment techniques. The autodigestion theory, detailing how trypsin leaks from the small intestine to the cardiovascular system, can eventually lead to multi-organ failure and death, if not treated promptly. This powerful approach allows us to capture cleaved peptide fragments as autodigestion is occurring, in real-time. By combining previous pore sensing optimizations, electrolyte conditions, and fabrication techniques, we have developed a novel design that has the potential to guide diagnostic advancements for years to come. Overall, this chapter demonstrates the tremendous potential of nanopores as a diagnostic

device and sets the stage for future breakthroughs in clinical diagnostics, personalized medicine, and disease monitoring.

5.2 Introduction

Circulatory shock describes the traumatic, and often deadly, insult to the human body when insufficient blood reaches the tissues. Despite extensive research into the pathophysiology of the condition, it is still the leading cause of death in the intensive care unit (ICU)¹. The poor prognosis for patients in circulatory shock, or simply ‘shock’, stems from a poor understanding of key events which ultimately leads to system-wide destruction including multiple organ failure². There are four stages in shock: initial, compensatory, progressive, and refractory. Accurate diagnosis must occur before the refractory period, as it is at this time when the patient has lost more than 40% of their blood volume and the chance of survival is severely limited³. Unfortunately, shock symptoms can vary greatly depending on age, health, cause of injury, and how much blood has been lost, emphasizing the need for an accurate, quick, diagnostic device.

One hypothesis is that the permeability of the intestinal barrier is a key factor in shock^{4,5} and that measurements of intestinal barrier function are useful in accessing the degree of shock and the likelihood to respond to treatments. The loss of barrier function at the epithelial and mucosal layers of the intestine implicates digestive enzymes as key factors in systemic dysfunction^{5,6}. The tight junctions in the epithelial layer serve as gatekeepers that normally hold back enzymes including proteases and lipases. When barrier function fails, quarantined enzymes begin diffusing into the bloodstream where they

are distributed to healthy tissues of the body. As a result, homeostasis throughout the body is severely and irreversibly disturbed. Additionally, when animal models of shock were treated with various enzyme inhibitors, the survival rate increased compared to the untreated group⁷. Proteases have been the focus of current studies and mounting evidence supports that these enzymes play a key factor in shock. However, it is important to note that the mere detection of proteases does not necessarily indicate their biological activity or functional relevance.

Detecting the presence of peptide fragments generated by proteases can provide valuable information about the activity levels of the enzymes, this is because the quantity of peptides cleaved directly correlates with enzymatic activity. Therefore, by detecting and analyzing these peptide fragments, it is possible to determine the level of activity in a sample. Additionally, there is evidence suggesting that the amount of peptides found within the blood of a rat experiencing hemorrhagic shock is greater than in a healthy rat⁶, specifically, 295 peptides were found under a state of shock while 126 peptides were found under healthy conditions (with 96 peptides found in both conditions). Interestingly, the number of circulating peptides under a state of shock was significantly reduced when in the presence of tranexamic acid (protease inhibitor)⁸. Thus, in this chapter, we sought to combine the studies indicating that trypsin activity in the blood leads to multi-organ failure and death with nanopore detection techniques to quantify the increase in peptide production as trypsin continues its non-specific digestion in the blood.

Nanopores are an excellent single-molecule sensor because of their high throughput, specificity, and real-time detection abilities. Because of this, nanopores have

been used to detect and analyze a wide range of biomolecules, including DNA^{9,10}, RNA¹¹, proteins^{12,13}, and metabolites¹⁴. These pores can be made from a variety of materials, including proteins¹⁵, silicon¹⁶, and graphene¹⁷, and can be engineered to have different sizes, shapes, and chemical properties to accommodate detection of a multitude of molecules. One of the key advantages of nanopores is their ability to detect and differentiate between different molecules based on their size, shape, and charge. When a molecule passes through a nanopore, it changes the electrical properties of the pore, allowing it to be detected and analyzed using sensitive electrical techniques¹⁸.

To ensure specificity and prevent clogging, most nanopore studies utilize purified samples. Because of this, studies that incorporate the usage of complex solutions, such as biofluids, are scarce. One study by Sze. et. al. synthesized molecular carriers from DNA to detect up to three protein targets using human serum with nanopipettes¹⁹. In a planar membrane nanopore, a study was done detailing how magnetic nanoparticles can be used to detect prostate-specific antigen (PSA) down to 0.8 femtomolar concentration²⁰. Both studies involved pre-treatment steps to work with the biological samples. The former diluted the human serum 1:20 in electrolyte solution while the latter exposed the plasma portion of the blood to their fabricated anti-PSA magnetic nanoparticles. Combined, these studies demonstrate the potential of using nanopores for analysis in complex biological samples. With the fabrication of PDMS chip and incorporation of a dialysis unit, proteins and peptides can be detected without the need of centrifugation or treatment of alternative labelling components.

Additionally, noteworthy investigations have been conducted to examine trypsin concentrations in biofluids. In one particular study, trypsinogen activation peptide, which is cleaved in equimolar quantities during the transition from trypsinogen to active trypsin²¹. The effects of pancreatitis were observed through enzyme-linked immunosorbent assay (ELISA). However, the measured concentrations of trypsinogen activation peptide in this study ranged from 24.1 mM²², which is considerably higher compared to the working concentrations that yield observable changes in event properties as demonstrated in this chapter. Furthermore, a recent publication reported the detection of trypsin using a microcontact imprinted surface, with a detection range spanning from 1.0×10^{-13} to 1.0×10^{-7} M, along with measurement of trypsin activity²³. It is important to acknowledge that these measurements were conducted in isolated systems without complex biofluids, necessitating further adjustments to accommodate diverse samples. With this chapter, our aim is to bridge the gap between these studies by employing a real-time, label-free detection sensor capable of monitoring trypsin digestion products in highly heterogeneous solutions, such as human blood.

To date, solid-state nanopores have been used to detect a wide range of biomolecules. In protein detection applications, nanopores can be used to detect the presence and concentration of specific proteins in a sample based on their size and charge²⁴⁻²⁶. Overall, nanopores are a powerful tool for the detection and analysis of a wide range of biomolecules, offering high sensitivity and specificity, rapid detection times, and the potential for real-time monitoring and analysis. As such, they are an important technology

for advancing our understanding of biological systems and developing new diagnostic and therapeutic approaches for a range of diseases.

In this final chapter, we present a diagnostic approach utilizing the remarkable single-molecule sensor, nanopores. This revolutionary technology has the potential to advance clinical diagnosis, as it allows for the detection of a vast array of biomolecules at extremely low concentrations, without the need for labeling or pre-treatment. We demonstrate a lab-on-chip device capable of monitoring and quantifying peptide fragments generated from trypsin digestion. This is a crucial phenomenon as autodigestion, the process in which trypsin leaks from the small intestine to the cardiovascular system, can lead to multi-organ failure and even death if not treated promptly. Our innovative approach captures cleaved peptide fragments in real-time as autodigestion is occurring, providing a powerful tool for disease diagnosis and monitoring. By utilizing nanopores to detect peptide fragments generated by trypsin, our approach offers a novel and promising approach to the diagnosis and monitoring of autodigestion-related diseases.

5.3 Results and Discussion

5.3.1 Peptide and Protein Characterization in High Ionic Strength Solution

In the previous chapter, we detailed how exposing peptides to various denaturing agents allowed for the observation of peptide length differences based on the change in current experienced by the nanopore upon peptide translocation. While this technique has its advantages, the main drawback is the need for concentration optimization, which can only be done if the analyte concentration is known. Because of this, a different

methodology must be adopted, given that the final goal is to use a sample of human blood, in which the concentrations of the various biomolecules would be timely to obtain.

We chose to revisit the usage of 1 M KCl with peptides and proteins to gain further information regarding the unique event characteristics with using this electrolyte solution. Similar to the previous chapter, the peptides glucagon and leucine-enkephalin (leu-enk) were studied at a concentration of 500 nM and with 15 nm diameter pore sizes. The voltage applied was -500 mV, and glucagon and leu-enk were driven to translocate into the pore (Figure 5.1a and b, respectively). A scatter plot of both peptides' event information is displayed in Figure 5.1c. In this figure, the current amplitude for both peptides are similar. Both populations are contained within 55-130 pA. However, when looking at the dwell time distributions, there is a noticeable difference. The longer peptide, glucagon (magenta), has slower dwell times than the shorter peptide, leu-enk (cyan). The peaks of the dwell time for glucagon and leu-enk are 1.2 and 0.5 ms, respectively. Under the 1 M KCl salt condition, peptide length information is determined by the dwell time of the molecule.

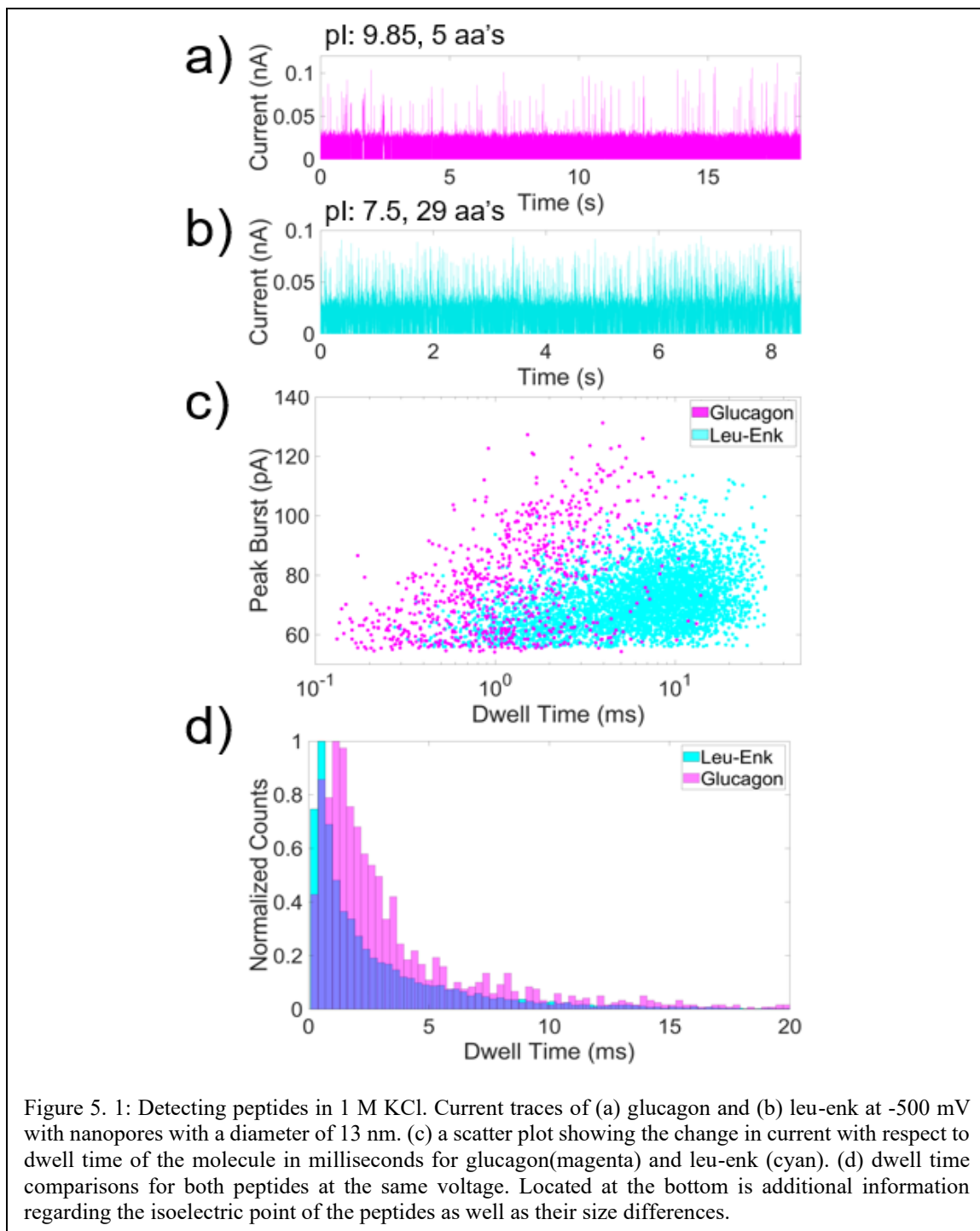


Figure 5. 1: Detecting peptides in 1 M KCl. Current traces of (a) glucagon and (b) leu-enk at -500 mV with nanopores with a diameter of 13 nm. (c) a scatter plot showing the change in current with respect to dwell time of the molecule in milliseconds for glucagon(magenta) and leu-enk (cyan). (d) dwell time comparisons for both peptides at the same voltage. Located at the bottom is additional information regarding the isoelectric point of the peptides as well as their size differences.

We then shifted our attention to detecting proteins with the 1 M KCl solution.

Proteins are notorious for transiently adhering to the walls of solid-state nanopores^{27,28}. In

the case where that does not occur, proteins often translocate through the nanopore rapidly. For this next section, bovine serum albumin (BSA) and trypsin were diluted to 1 nM concentrations in 1 M KCl. The nanopore was filled with 1 M KCl (symmetric

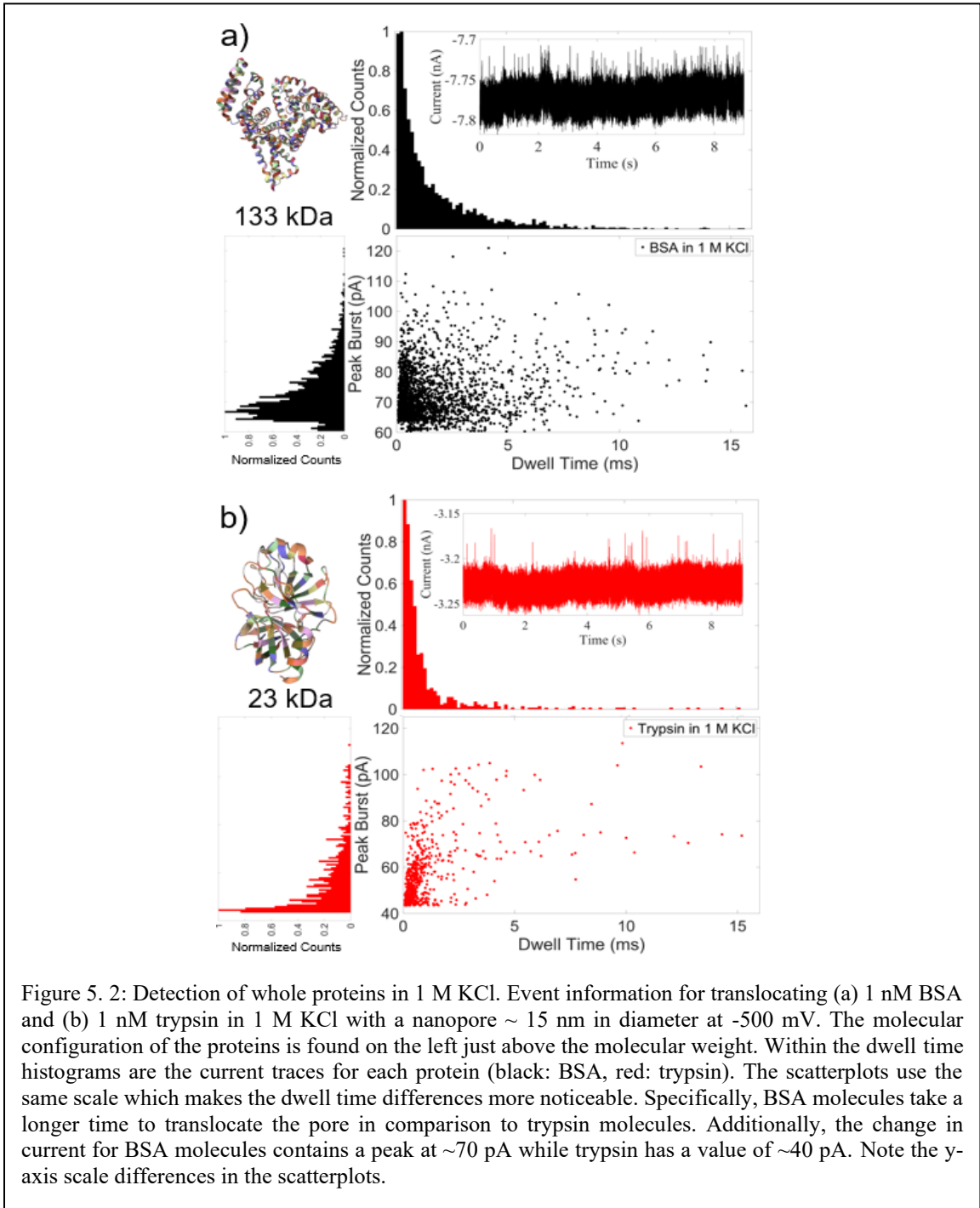
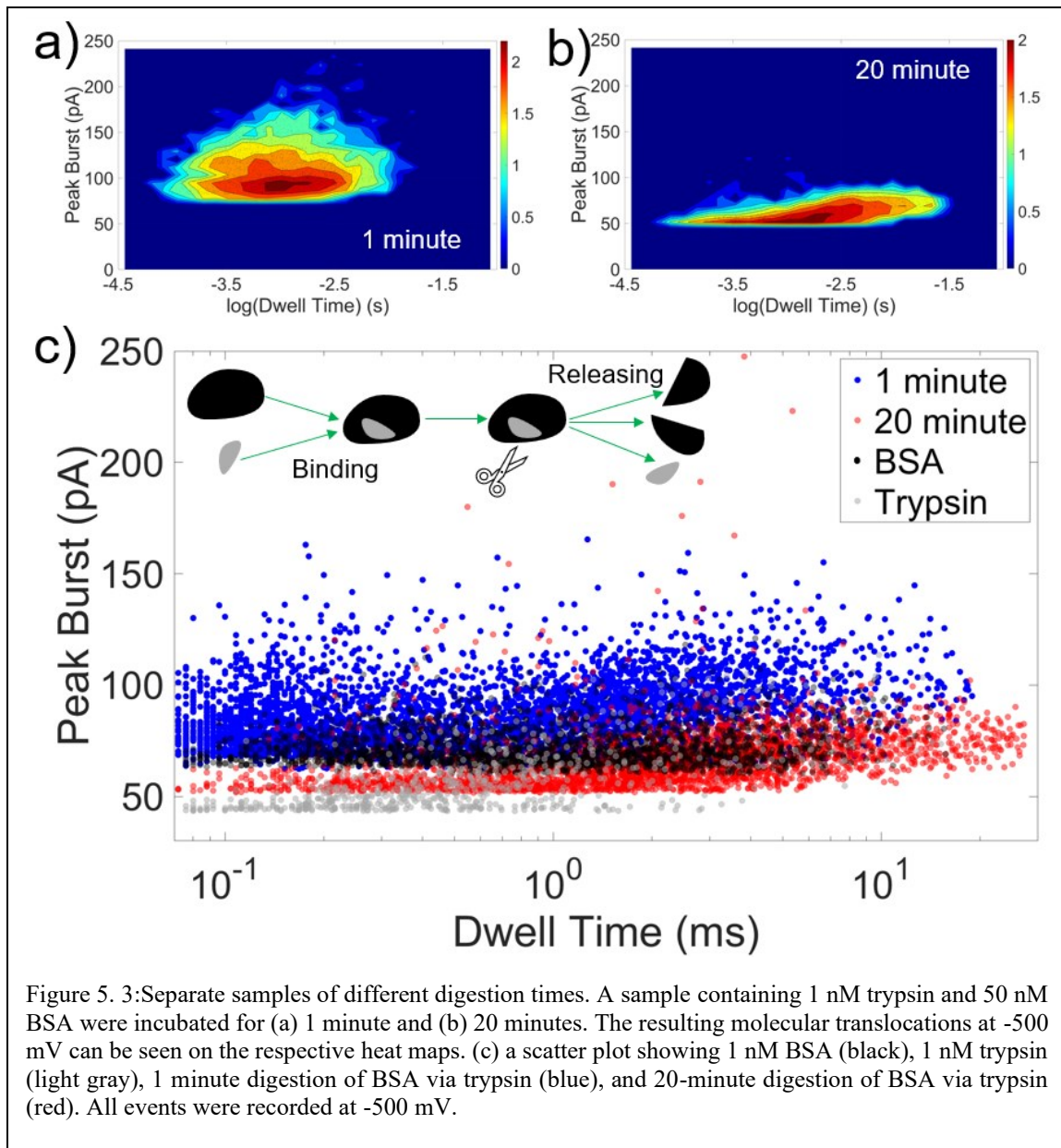


Figure 5. 2: Detection of whole proteins in 1 M KCl. Event information for translocating (a) 1 nM BSA and (b) 1 nM trypsin in 1 M KCl with a nanopore ~ 15 nm in diameter at -500 mV. The molecular configuration of the proteins is found on the left just above the molecular weight. Within the dwell time histograms are the current traces for each protein (black: BSA, red: trypsin). The scatterplots use the same scale which makes the dwell time differences more noticeable. Specifically, BSA molecules take a longer time to translocate the pore in comparison to trypsin molecules. Additionally, the change in current for BSA molecules contains a peak at ~70 pA while trypsin has a value of ~40 pA. Note the y-axis scale differences in the scatterplots.

concentrations) and -500 mV was applied. The event properties of BSA and trypsin are shown in Figure 5.2a and b, respectively. First, a molecular diagram of each protein is displayed, color coded by hydrophobicity. The molecular weights of each protein are vastly different, BSA being much larger than trypsin. The corresponding scatter plots and histograms detailing the current amplitude and dwell time of the events are shown in black and red for BSA and trypsin, respectively. The key differences between the molecules can be described by the change in current and dwell time. BSA, the larger molecule, is responsible for greater current amplitudes (65-75 pA) and longer dwell times (most occurring below 3 ms). While trypsin, on the other hand, contains peak bursts between 40 and 50 pA and most molecules translocate the pore in less than 2 ms. We can attribute BSA having a larger peak burst due to it being the larger molecule. As BSA enters the pore, its molecular diameter is larger than trypsin, allowing it to block a larger ionic flow, resulting in a greater change in current. The dwell time differences can be explained similarly, by the length of the molecules. Because these proteins are entering the pore in their globular state, the BSA molecule (being larger than trypsin) can enter the pore in a way that is longer than trypsin. The theory that longer molecules can exhibit longer dwell times has been reported, and we can use that reasoning to explain the dwell time differences that we see here, as well.

5.3.2 BSA Digested via Trypsin

Up to this point, we have shown that, in 1 M KCl, we can detect both peptides and proteins in solution. To prepare for detection of peptide fragments generated under a state



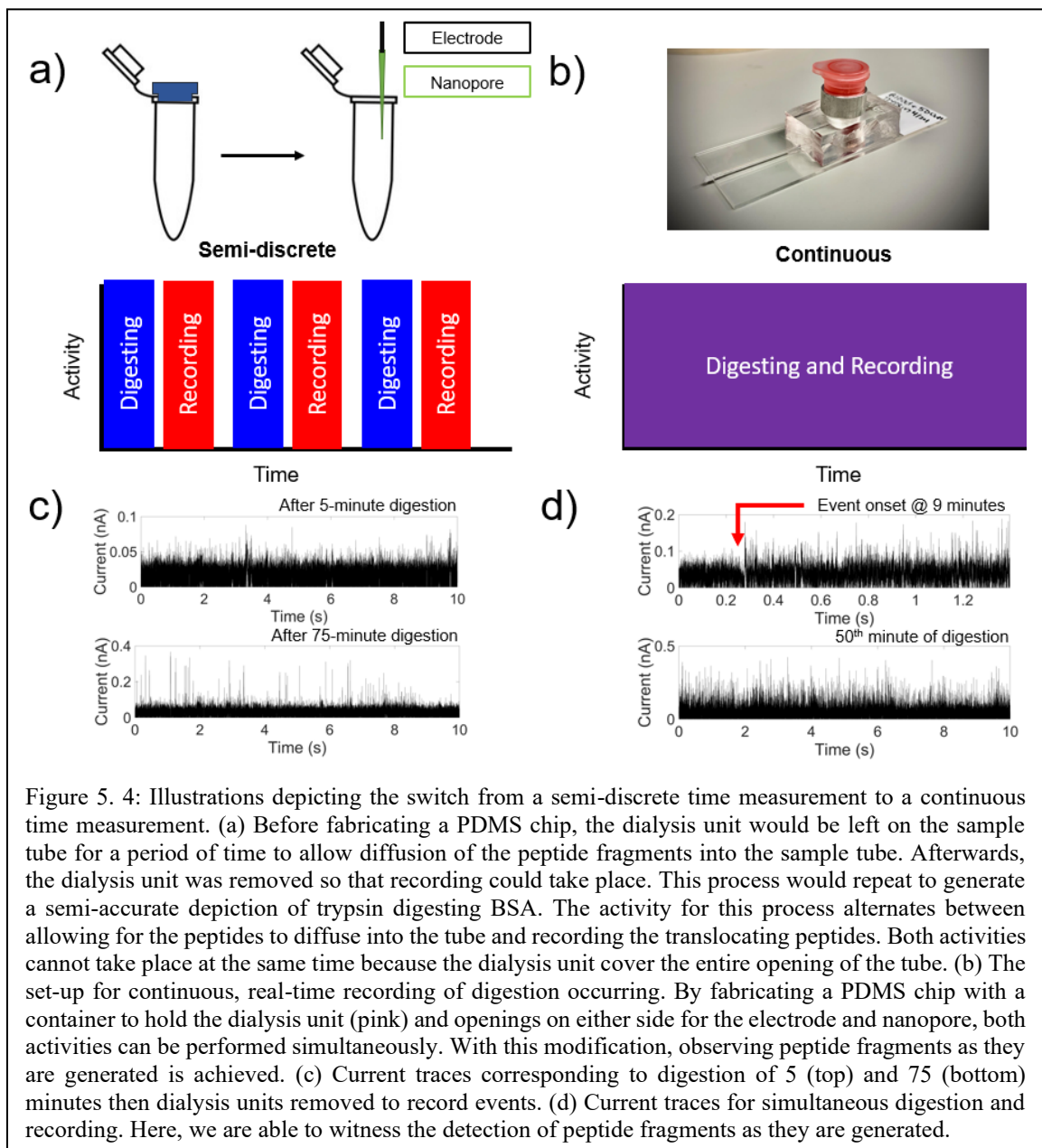
of autodigestion, we decided to perform two experiments having 50 nM BSA undergo digestion by 1 nM trypsin for two different time scales. By maintaining a 50:1 BSA:trypsin

ratio, we can ensure that most of the peptide fragments generated originate from BSA and not trypsin autodigesting itself. We chose to have a digestion time of 1 minute and 20 minutes. After the allotted time, the reactions were stopped via heat denaturation and then taken to the Axopatch 200B for recording.

Figure 5.3a and b present heat maps of the 1 minute and 20-minute digestion times of BSA via trypsin, respectively. The main noticeable difference is seen within the current amplitudes of the events. For the 1-minute incubation, the peak bursts of the events are mostly contained between 60-225 pA. Once digestion progresses, more cleavages are made by trypsin, resulting in smaller fragments. That is why, for the 20-minute condition, most of the event peak bursts remain between 50-100 pA. The overall range of the current amplitude nearly halves as the trypsin digestion is allowed to proceed. Because of the drastic changes in the event properties when digestion is occurring, we suspected it might be best to compare both digestion times with BSA and trypsin by itself in 1 M KCl. The results can be seen in the scatter plot in Figure 5.3c. In this figure, BSA, trypsin, 1-minute digestion, and 20-minute digestion are displayed as black, light gray, blue, and red dots, respectively.

Interestingly, the 1-minute digestion population contains the largest changes in current amplitude when compared to the other three samples. We suspect that the larger peak bursts might be caused by the transient binding of trypsin onto BSA. Once the sample temperature drops back to room temperature after heat denaturation, there is a possibility that the reconstituted whole proteins or the fragments themselves can anneal to each other. This might explain the generation of the larger events seen in the scatter plot. To illustrate

this, a graphical schematic is displayed at the top of the scatter plot in Figure 5.3c, where trypsin is the smaller light gray object and the larger black icon is BSA. Before the trypsin cleavage takes place, trypsin must bind to BSA. Potentially, the nanopore is detecting the BSA-trypsin complex as one event which has a large change in current.



5.3.3 Development of Real-Time Digestion Device

One of the common issues with nanopore detection is the tendency for the pore to become clogged, especially with a heterogenous sample. To combat this, we sought usage of a 3.5 kDa dialysis unit which allows for molecules < 3.5 kDa to flow through the unit while sequestering molecules > 3.5 kDa. To address the interesting aspect of last section's study (1-minute digestion events having larger peak bursts), we decided to combine the BSA: trypsin digestion with a dialysis unit.

The downside to this method is that the dialysis unit completely covers the opening of the sample tube, as seen in Figure 5.4a. To utilize the dialysis unit, we had to adopt a semi-discrete method for observation of digestion occurring. More specifically, the dialysis unit was left to incubate within the sample tube for a certain amount of time, afterwards the unit was removed and the sample tube was taken to the Axopatch 200B for recording of fragmented peptides. This process was repeated to generate semi-discrete digestion information of BSA via trypsin. An illustration describing procedures can be seen at the bottom of Figure 5.4a. To optimize the sensing conditions, namely, record cleaved peptides in real-time, a PDMS chip was fabricated. The actual PDMS chip set-up can be seen in Figure 5.4b. A hole in the center of the PDMS chip was used to secure the dialysis unit, in pink in the image. Either side of the chip contained an electrode and the nanopore. With this device, the unit is able to filter the digested peptides simultaneously while the nanopore is recording. This is the final device we constructed to observe autodigestion occurring in human blood.

Table 5. 1: Molecular weights of biomolecules found in the blood. The molecules written in **red** are unable to pass through the 3.5 kDa dialysis unit. The remaining are detectable in their globular state in unmodified, whole blood.

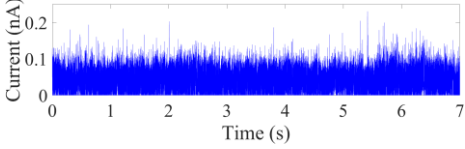
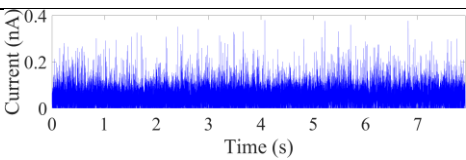
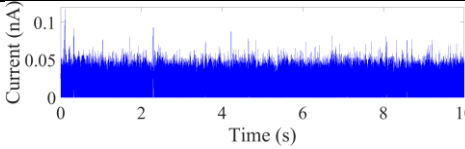
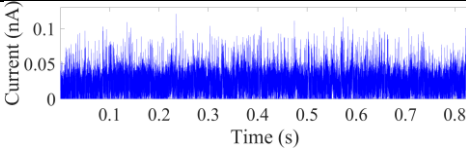
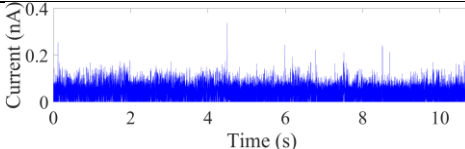
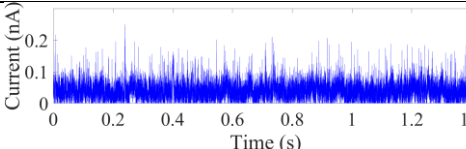
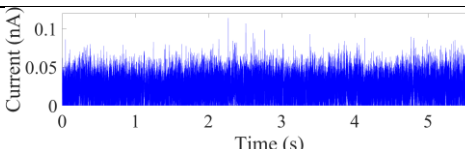
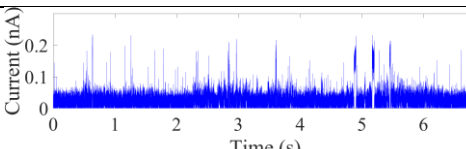
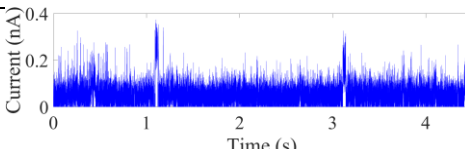
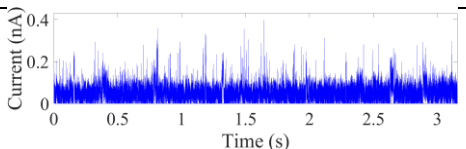
Biomolecule	MW (Da)
Glucose	180
Adrenaline	183
Testosterone	288
Noradrenaline	319
Cholesterol	386
Vitamin E	430
Vitamin K	450
Vitamin A	536
Vitamin D	769
Glucagon	3483
Insulin	5808
Cytokines	~6000-12000
Antibodies	150000

5.3.4 Autodigestion Observation in Whole Blood

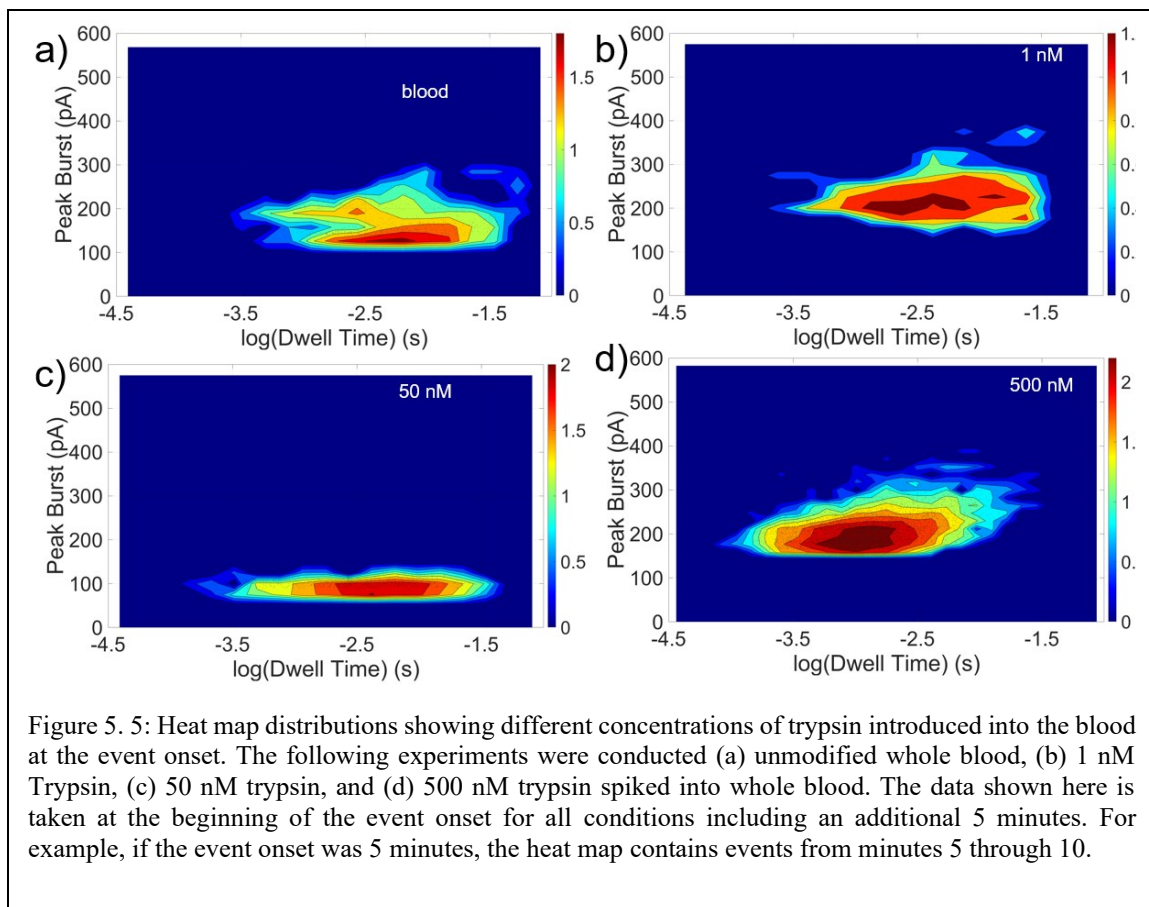
Finally, with the optimized PDMS chip, we can focus on real-time detection of digested peptides under a state of autodigestion. We first decided to examine unmodified whole blood (undiluted) in the dialysis unit. With the cut-off value being 3.5 kDa, certain biomolecules can pass through the filter without being digested. Proteins, such as those

found in Table 5.1, can be detected in their native, globular state. It is imperative to study whole blood as this will develop the baseline event rate for detecting other conditions in which trypsin is spiked into the blood. Table 5.2 contains the current trace of the event onset as well as the current traces of events during the middle of recording for each condition tested. Furthermore, the corresponding table caption provides the precise timing of the event onset for each condition. Unmodified blood experienced the longest event onset time occurring at 23 minutes. The highest concentration of trypsin (500 nM) inserted into the blood had the shortest event onset of three minutes.

Table 5. 2: Current traces for each condition performed using the PDMS device. The event onsets were the following (Descending): 9, 23, 11, 9, and 3 minutes.

Sample Type	Event Onset	Events
50 nM BSA + 1 nM trypsin		
Unmodified Blood		
Blood + 1 nM trypsin		
Blood + 50 nM trypsin		
Blood + 500 nM trypsin		

To mimic autodigestion conditions in which trypsin leaks out of the small intestine into the cardiovascular system, different concentrations of trypsin were spiked into the human blood and the subsequent peptide fragments were detected. Whole blood, blood +



1 nM trypsin, blood + 50 nM trypsin, and blood + 500 nM trypsin heat maps are shown in Figure 5.5a, b, c, and d, respectively. Whole blood (in absence of trypsin) was responsible for the longest dwell times. The reasoning behind this is that mostly whole proteins comprise the molecules detected. There is no trypsin present to digest the proteins into smaller fragments. Because of this, we predict that the longer dwell times correspond to globular proteins. Similar to the BSA study, larger proteins translocating the pore can exhibit longer dwell times. We hypothesize that the longer dwell times in the blood sample occur because of the proteins allowed to filter into the nanopore sample.

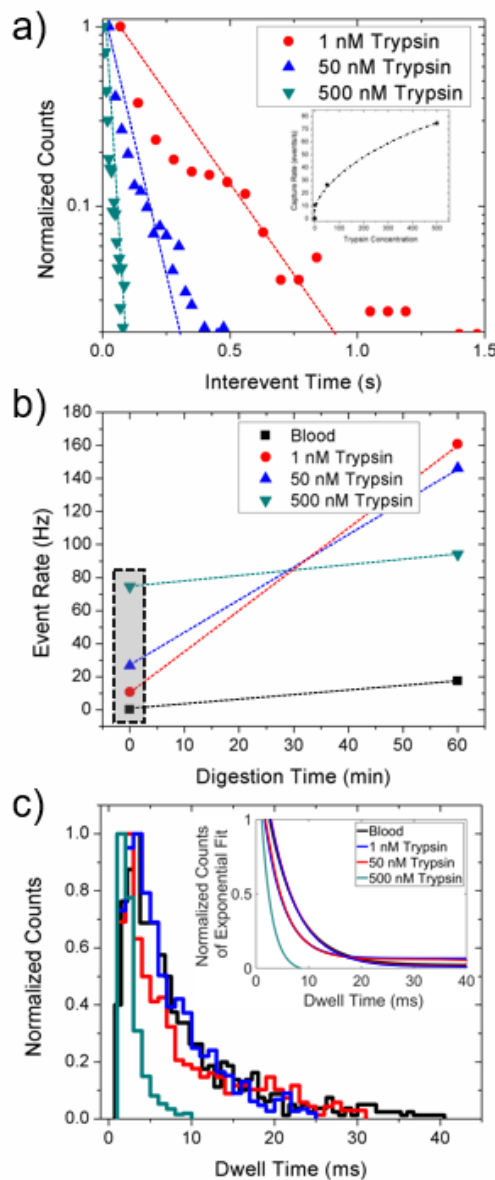


Figure 5. 6: Calculated even rates and dwell time comparisons of unmodified blood and blood with added trypsin to simulate a state of autodigestion. (a) interevent time (the time between two successive events) of each condition (whole blood, blood + 1 nM trypsin, blood + 50 nM trypsin, and blood + 500 nM trypsin) at 10 ± 5 minutes. Because the unmodified whole blood condition did not have any events during this time, it is excluded from the interevent calculation in (a). The lowest event rate belongs to the blood + 1 nM trypsin condition while the fastest event rate take place at blood + 500 nM trypsin. (b) a scatter plot showing the calculated event rates at two different time points for each condition. The section highlighted with a black dotted rectangle is the calculated event rates for (a). The highest concentration of trypsin yielded the highest event rate (and vice versa) during the initiation of events. Additionally, each condition's event rate increases with progressing digestion time, albeit not at the same slope. (c) Histogram of the dwell times at each condition's event onset period + 5 minutes. Inset: An exponential fit of the dwell times.

As trypsin is spiked into the blood system, changes in peak burst as well as dwell time are observed when looking at each heat map. The conditions of whole blood, blood + 1 nM trypsin, and blood + 500 nM trypsin have similar peak burst populations, mostly occurring between 100 and 400 pA. However, the 50 nM condition exhibits a decrease in peak burst. Specifically, the range is limited to 50-180 pA. While the specific reasoning behind this remains elusive, we can also examine the dwell time populations and calculate the event rate of each condition to determine any differences occurring as a result of adding trypsin into the blood.

The interevent time (time between two successive events) was calculated for each condition. The idea behind this was that the higher quantity of trypsin present in the blood, the increased number of peptides fragments would be created, leading to a higher event rate. The interevent time was calculated for each condition by methods previously described by Wanunu et. al²⁹. In brief, histograms of the interevent time were created and then the event rate was calculated by exponentially fitting the interevent time histogram. The results at 10 ± 5 minutes for each condition are shown in Figure 5.6a, where the steepest slope corresponds to the fastest event rate. Located within Figure 5.6a is an inset describing the change in event onset capture rate as a function of trypsin concentration within the system. The relationship between the two follows a logarithmic trend, where lower trypsin concentrations produce a greater change in event rate and vice versa. With this, we anticipate that there is a saturation point in which the event rate will be less responsive at extremely high concentrations of trypsin. Through further development of

this model, we can estimate trypsin concentrations of unknown samples, similar to a standard curve.

Two different time points were taken from each of the four conditions and the event rates were calculated using the aforementioned method (Figure 5.6b). The data points contained within the black dotted box correspond to the results shown in Figure 5.6a and display a positive relationship between event rate and trypsin concentration. Specifically, the higher quantity of trypsin present yielded the greater event rate during the event onset period. As digestion time progresses, the event rate also increases. However, the slope between the two time points for each condition is not the same. The unmodified blood and blood + 500 nM trypsin exhibit a similar change in event rate as digestion time increases. On the other hand, the blood + 1 nM trypsin and blood + 50 nM trypsin experience a steep increase in event rate (over 140 events/second). The underlying mechanism leading to this result remains unclear and warrants further investigation. However, the initial event rate as well as the event onset time correspond well with the theory that trypsin in the blood generates peptide fragments. Specifically, the increased amount of trypsin present in the blood yields a quicker event onset as well as a faster event rate, due to the abundance of peptide fragments.

Because of the relationship occurring between dwell time and peptide length (Figure 5.1) and protein size (Figure 5.2), we sought to also investigate each condition for changes in dwell time (Figure 5.6c). When there is no trypsin present, we expect the events to be representative of the whole proteins that are able to pass through the dialysis unit (shown in Table 5.1). For unmodified whole blood (black), the peak of the dwell time

occurs at 3 ms and extends to over 40 ms while the highest amount of trypsin (500 nM, dark cyan) has a peak dwell time of 1 ms and all molecules translocate in less than 10 ms. We suspect this to be due to trypsin cleaving proteins into peptide fragments or protein subunits, which elicit a shorter dwell time when translocating the pore. As the whole blood condition should contain mostly globular proteins, the longer dwell times that coincide with whole proteins (in comparison to oligopeptides) ostensibly support this result. The intermediate conditions, 1 and 50 nM trypsin, produce peak dwell times of 2 and 3 ms respectively. It is a peculiar result to have the same peak dwell times for both whole blood and blood + 50 nM trypsin. On the same note, the exponential fits of the dwell times (Figure 5.6c inset) show that those two conditions also have similar time constants. We can postulate that the reason behind each condition (excluding 500 nM trypsin) producing similar dwell times can be due to a sensitivity range. Perhaps adding trypsin in concentration quantities between 0 and 50 nM does not elicit much change in dwell times. However, when comparing the dwell times between unmodified whole blood with blood + 500 nM trypsin, we see a strong response in that the dwell times of the blood + 500 nM trypsin condition are much shorter than that of whole blood. Future studies can repeat this analysis with a midpoint (250 nM) and higher (750 nM or 1 μ M) amount of trypsin to confirm or deny the presence of a sensitivity range for dwell time distributions differences.

5.4 Conclusion

In conclusion, we have demonstrated the potential of solid-state nanopores in the detection of small peptides and proteins of varying sizes, utilizing 1 M KCl to enhance the sensitivity of the system. Furthermore, we have shown that protein digestion, specifically

trypsin digestion, can be monitored in real-time through the detection of peptide fragments. The incorporation of a PDMS chip and dialysis unit has allowed for efficient detection of cleaved peptides, offering a powerful tool in understanding the autodigestion process and its implications on human health.

Our results also indicate that the amount of trypsin added to the system affects the event rate of peptides, suggesting the importance of optimizing protease concentration for future experiments. With further development and refinement, the combination of solid-state nanopores, 1 M KCl, and microfluidic devices has the potential to become a powerful diagnostic tool for a wide range of biomolecules, including peptides and proteins, in various biological fluids.

To summarize, this study demonstrates the capability of nanopore technology to provide a rapid and sensitive approach for peptide fingerprinting and protein analysis. The potential for future clinical applications of this technology holds great promise in enhancing our understanding of the underlying mechanisms of diseases and developing new diagnostic tools for early disease detection.

5.5 Materials and Methods

5.5.1 PDMS Chip Fabrication

In a large plastic container, the monomer (40 mL) and curing agent (4 mL) were mixed for 5 minutes with a stirring rod. The transparent PDMS silicone encapsulant elastomer kit was purchased from QSIL 216. After the five minutes passed, the container was degassed to remove all bubbles, which typically took three hours. Once all bubbles

were removed. The solution was poured into a sterile square petri dish (BCP 100 x 100 mm) that held six half rods (1 mm x 300 mm) equally spaced. After pouring, the square petri dish was taken back to degas any bubbles that may have formed during the previous steps. Next, the square petri dish was placed on a heating plate for 2.5 hours at 80 °C. Once the curing process was complete, the half rods were excised out of the PDMS mold and a 10 mm sterile hole punch (Fisher Scientific, NC9236770) was used to create a hole through the mold to secure the 3,500 MWCO dialysis unit (Thermo Scientific, 69552). Microscope slides (Marienfeld Superior, 1000200) were wiped with a Kimwipe Delicate Task Wiper (Kimberly-Clark Professional™ 34120) sprayed with 70% Ethanol before plasma cleaning for five minutes.

At this time, the nanopore was backfilled with 1 M KCl (Thermo Fisher, P217-500) and the electrodes were rinsed. Epoxy was mixed with a plastic stirring rod and used to secure the nanopore and electrode within the half rod indentations. The epoxy was also used to create an airtight seal between the PDMS chip and the microscope slide. The entire device was left sitting for 10 minutes to ensure the epoxy was set. To prepare for nanopore experiments, 150 µL of 1 M KCl was inserted into the hole within the PDMS layer. A combination of nylon (3/8 F/W 0.75 OD x 0.06T, B009OLQTVU) and aluminum (unthreaded 1/4" length, AL-50-37-25-S-100) spacers were used to elevate the dialysis unit to prevent the bottom of the filter from hitting the nanopore. Blood (and trypsin, when appropriate) was inserted into the dialysis unit and a volume of 200 µL was maintained for each experiment.

5.5.2 Fabrication of Quartz Nanopipettes

Quartz capillaries (Sutter Instruments, QF100-70-7.5) of 7.5 cm in length, 1.00 mm in outer diameter, and 0.70 mm inner diameter were plasma cleaned for a minimum of five minutes. Afterwards, the capillaries were transported to the P-2000 laser puller (Sutter Instrument Co.) where a CO₂ laser directed into the center of the capillary length created two identical nanopipettes. and a one-line protocol was used: (1) HEAT: 630; FIL: 4; VEL: 61; DEL: 145; PULL: from 170-190. This resulted in two identical, conical nanopores (diameter between 12 and 15 nm) within a heat duration of approximately 4.8 s.

Silver electrodes wires were cut into inch long fragments and then placed into a bleach bath overnight. Afterwards, the electrodes were rinsed DI water. Nanopipettes were then backfilled with electrolyte solution. Prior to attaching the sample and nanopipette to the Axopatch head stage, the nanopipettes were observed under an optical microscope. This was done to check for any breaks or bubbles in the nanopore tip. After inspection, the nanopore and sample were secured within the head stage in a metal box and connected with wires attached to silver chloride electrodes.

5.5.3 Electrolyte and Sample Preparation

All KCl electrolytes were prepared using DI water and buffered at pH ~7.4 using Tris-EDTA (BP2475-500, Thermo Fisher). Both pH and conductivity of the final solutions were measured using AB200 pH/Conductivity Benchtop Meter (Fisher Scientific) at room temperature. All solutions were filtered using 0.2-micron syringe filters (S6596FMOSK, Thermo Fisher Scientific) prior to nanopore experiments. Glucagon

(69271) and leucine-enkephalin (AAJ66801LB0) were purchased from Thermo Fisher. BSA was purchased through New England BioLabs (#B9000). Human blood (single donor, black male, 38 years of age) was sourced from Innovative Research (SKU IWB1K2E10ML).

5.5.4 Data Acquisition and Analysis

The Axopatch 200B patch-clamp amplifier (Molecular Devices) in voltage-clamp mode was used to measure the current fluctuations in time. Prior to acquisition, the gain was optimized and the signal was filtered with a low-pass Bessel filter at 10 kHz and digitized using the Digidata 1550B (Molecular Devices). The data was acquired at a frequency of 250 kHz. A custom-made MATLAB script was utilized to analyze the events acquired via Axopatch 200B.

5.6 References

1. Vincent, J.-L. & De Backer, D. Circulatory Shock. *New England Journal of Medicine* **369**, 1726–1734 (2013).
2. Rossaint, J. & Zarbock, A. Pathogenesis of Multiple Organ Failure in Sepsis. *CRI* **35**, (2015).
3. Gutierrez, G., Reines, Hd. & Wulf-Gutierrez, M. E. Clinical review: Hemorrhagic shock. *Critical Care* **8**, 373 (2004).
4. Baker, J. W., Deitch, E. A., Li, M. A., Berg, R. D. & Specian, R. D. Hemorrhagic Shock Induces Bacterial Translocation from the Gut. *Journal of Trauma and Acute Care Surgery* **28**, 896 (1988).
5. Schmid-Schönbein, G. W. & Chang, M. The Autodigestion Hypothesis for Shock and Multi-organ Failure. *Ann Biomed Eng* **42**, 405–414 (2014).
6. Aletti, F. *et al.* Peptidomic Analysis of Rat Plasma: Proteolysis in Hemorrhagic Shock. *Shock* **45**, 540–554 (2016).
7. DeLano, F. A., Hoyt, D. B. & Schmid-Schönbein, G. W. Pancreatic Digestive Enzyme Blockade in the Intestine Increases Survival After Experimental Shock. *Science Translational Medicine* **5**, 169ra11-169ra11 (2013).
8. Maffioli, E. *et al.* Peptidomic characterization of hemorrhagic shock plasma samples: Effects of tranexamic acid. *Journal of Critical Care* **42**, 380 (2017).
9. Akahori, R. *et al.* Slowing single-stranded DNA translocation through a solid-state nanopore by decreasing the nanopore diameter. *Nanotechnology* **25**, 275501 (2014).
10. Sharma, V., Farajpour, N., Lastra, L. S. & Freedman, K. J. DNA Coil Dynamics and Hydrodynamic Gating of Pressure-Biased Nanopores. *Small* **18**, 2106803 (2022).
11. Furlan, M. *et al.* Computational methods for RNA modification detection from nanopore direct RNA sequencing data. *RNA Biology* **18**, 31–40 (2021).
12. Bandara, Y. M. N. D. Y., Farajpour, N. & Freedman, K. J. Nanopore Current Enhancements Lack Protein Charge Dependence and Elucidate Maximum Unfolding at Protein's Isoelectric Point. *J. Am. Chem. Soc.* **144**, 3063–3073 (2022).
13. Lastra, L. S., Bandara, Y. M. N. D. Y., Sharma, V. & Freedman, K. J. Protein and DNA Yield Current Enhancements, Slow Translocations, and an Enhanced Signal-to-Noise Ratio under a Salt Imbalance. *ACS Sens.* **7**, 1883–1893 (2022).
14. Zernia, S., van der Heide, N. J., Galenkamp, N. S., Gouridis, G. & Maglia, G. Current Blockades of Proteins inside Nanopores for Real-Time Metabolome Analysis. *ACS Nano* **14**, 2296–2307 (2020).

15. Vu, T. *et al.* Employing LiCl salt gradient in the wild-type α -hemolysin nanopore to slow down DNA translocation and detect methylated cytosine. *Nanoscale* **11**, 10536–10545 (2019).
16. Storm, A. J., Chen, J. H., Zandbergen, H. W. & Dekker, C. Translocation of double-strand DNA through a silicon oxide nanopore. *Phys. Rev. E* **71**, 051903 (2005).
17. Merchant, C. A. *et al.* DNA Translocation through Graphene Nanopores. *Nano Lett.* **10**, 2915–2921 (2010).
18. Dekker, C. Solid-state nanopores. *Nature Nanotech* **2**, 209–215 (2007).
19. Sze, J. Y. Y., Ivanov, A. P., Cass, A. E. G. & Edel, J. B. Single molecule multiplexed nanopore protein screening in human serum using aptamer modified DNA carriers. *Nat Commun* **8**, 1552 (2017).
20. Chuah, K. *et al.* Nanopore blockade sensors for ultrasensitive detection of proteins in complex biological samples. *Nat Commun* **10**, 2109 (2019).
21. Fernández-del Castillo, C., Schmidt, J., Warshaw, A. L. & Rattner, D. W. Interstitial protease activation is the central event in progression to necrotizing pancreatitis. *Surgery* **116**, 497–504 (1994).
22. Hartwig, W. *et al.* Trypsin and activation of circulating trypsinogen contribute to pancreatitis-associated lung injury. *American Journal of Physiology-Gastrointestinal and Liver Physiology* **277**, G1008–G1016 (1999).
23. Ertürk, G., Hedström, M. & Mattiasson, B. A sensitive and real-time assay of trypsin by using molecular imprinting-based capacitive biosensor. *Biosens Bioelectron* **86**, 557–565 (2016).
24. Chau, C. C., Radford, S. E., Hewitt, E. W. & Actis, P. Macromolecular Crowding Enhances the Detection of DNA and Proteins by a Solid-State Nanopore. *Nano Lett.* **20**, 5553–5561 (2020).
25. Firnkes, M., Pedone, D., Knezevic, J., Döblinger, M. & Rant, U. Electrically Facilitated Translocations of Proteins through Silicon Nitride Nanopores: Conjoint and Competitive Action of Diffusion, Electrophoresis, and Electroosmosis. *Nano Lett.* **10**, 2162–2167 (2010).
26. Japrun, D. *et al.* Single-Molecule Studies of Intrinsically Disordered Proteins Using Solid-State Nanopores. *Anal. Chem.* **85**, 2449–2456 (2013).
27. Awasthi, S. *et al.* Polymer Coatings to Minimize Protein Adsorption in Solid-State Nanopores. *Small Methods* **4**, 2000177 (2020).
28. Larkin, J., Henley, R. Y., Muthukumar, M., Rosenstein, J. K. & Wanunu, M. High-Bandwidth Protein Analysis Using Solid-State Nanopores. *Biophysical Journal* **106**, 696–704 (2014).

29. Wanunu, M., Morrison, W., Rabin, Y., Grosberg, A. Y. & Meller, A. Electrostatic focusing of unlabelled DNA into nanoscale pores using a salt gradient. *Nature Nanotech* **5**, 160–165 (2010).

Chapter 6: Conclusion and Outlook

In summary, this thesis has highlighted many diagnostic advantages to incorporating nanopores into the medical field. This work has jumped in complexity with each chapter to ultimately develop a portable, proof-of-concept device to evaluate digestive enzyme activity through the usage of human blood. And, as science often progresses, the path toward the final research idea was not straight forward.

In the first chapter, our work focused on setting the foundation for detecting trypsin via molecular carriers (Lambda DNA) utilizing low ionic strength conditions. With this, we observed DNA translocating the nanopore in the anti-electrophoretic direction. Specifically, DNA would enter the pore when a negative voltage was applied. Through the additional studies performed at various electrolyte concentrations, pore depths, and biomolecules, we developed an alternative theory to the origin of conductive events in a nanopore. Lastly, our report details the detection of proteins and DNA under asymmetric salt conditions, a step towards future planned studies where protein (trypsin) would be bound to DNA and the entire molecular carrier would be detected. Our chapter defines a flux imbalance in favor of cations to be one of the contributing factors in witnessing conductive events in a nanopore.

During the second aim, we further fabricated a molecular carrier to bind to Cas9 to mimic the molecular carrier that would be bound to trypsin. At this time, we witnessed how integrating a salt gradient manipulated the cationic flux and provided a superior signal-to-noise ratio when detecting DNA. To further support this finding, we critically compared the DNA detection results from low ionic strength conditions, high ionic strength

conditions (gold standard), and asymmetric high ionic strength conditions. Additionally, during this chapter, we developed two methodologies to determine the configuration of DNA as it enters the nanopore. This is a crucial step in determining the difference between a molecular carrier bound to its target molecule or a singular DNA in a nonlinear configuration. We found that high asymmetric salt conditions yield the most peak separation in differing DNA configurations and provided longer dwell times due to electroosmotic flow and electrophoretic forces opposing each other. We concluded the second chapter with the detection of DNA (un)bound to Cas9 and reported the difference in the event shape for each complex passing through the nanopore. At the culmination of this chapter, we had shown that molecular carrier detection was achievable with a salt gradient.

At this time, we chose to pivot our research from detecting whole proteins bound to DNA (molecular carrier) to detecting the fragments generated as a result of trypsin activity in the blood. The detection of trypsin would not yield any information in regard to the actual enzymatic activity and if we wanted to step in the direction towards a diagnostic device, the quantity of peptide fragments detected would provide more information surrounding the autodigestion rate within the body. With this in mind, we focused our efforts into developing a solution that would linearize and uniformly charge all peptides. The aforementioned solution was compared to the “gold standard”, 1 M KCl and the results showed that the denaturing solution provided peptide length differentiability and an extremely high signal-to-noise ratio. After looking at two differently sized peptides, glucagon and leu-enkephalin, we expanded our study to a heterogeneous analyte solution

(peptide ladder). Information about length was kept within the change in current as the peptides passed through the pore. In conclusion, we found that this solution outperformed the gold standard in its superior signal to noise ratio as well as peak separation between the changes in current of each peptide. The caveat to this methodology is that the ratio between the denaturing solution and analyte is highly sensitive and specific. In other words, the concentration of the peptides in solution must be known to optimize the concentration of the denaturing solution. Because of this, it would be an extremely difficult and lengthy process to employ a denaturing solution in a diagnostic test, as the concentration of peptides in the blood would be unknown. As impactful as this would be to the protein fingerprinting field, we had to adapt one last time to optimize the detection conditions of peptides in the blood.

For the final aim, we sought to develop a device capable of detecting peptide fragments in the blood generated by trypsin in a state of autodigestion in real-time. Firstly, we conducted experiments to determine if detection as well as size discrimination of peptides was still achievable in 1 M KCl. We then expanded this to sense whole proteins and discrete digestion times of BSA via trypsin. Once we noticed that digestion information can be determined through changes in current, we incorporated usage of a dialysis unit and PDMS mold to filter undigested, larger biomolecules and detect peptide fragments in real-time, respectively. We performed experiments with unmodified whole blood, whole blood spiked with trypsin (autodigestion), and whole blood spiked with trypsin and aprotinin (a serine protease inhibitor to mimic inactive protease in the blood). We saw that the event onset differed from each condition, namely, the higher concentration of trypsin added into

the blood resulted in a quicker event commencement. Additionally, we calculated the event rates at different time points in each condition.

In the future, there are areas of improvement that should be addressed to fully optimize the determination of digestive enzymatic activity level via nanopores. Moving forward, alternative methodologies can be incorporated to slow down and limit the quantity of whole proteins passing through the filter such as applying pressure opposite to the direction of translocation, as well as employing a dialysis unit of a smaller limit, respectively.

Additionally, the alternative electrolyte conditions that were developed in chapters one through three could be tested, especially the asymmetric salt conditions, albeit the challenge of loading the nanopore with the analyte is addressed. One useful analysis method for event detection is through the usage of a template search. With this, one can search through data files for events of a specific shape to achieve specialized detection of events. In the future, perhaps this can be utilized to separate whole proteins from fragmented oligopeptides to provide a time-dependent understanding of the ratio between proteins and peptides during a state of autodigestion via trypsin.

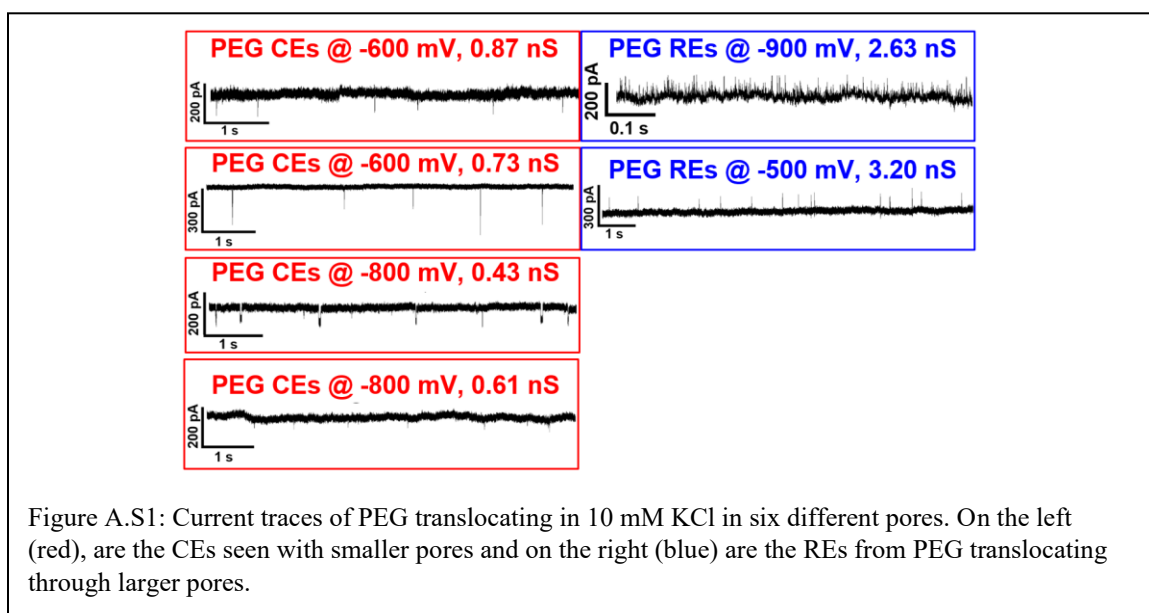
The results from aim three are promising due to utilization of various denaturing agents that can provide spatiotemporal resolution of peptides, given that the concentration is known. This can eventually lead to protein sequencing via quartz nanopipettes. Lastly, the progress in aim one and two significantly improves our knowledge in regard to the understanding of the mechanism behind conductive events. With the long dwell times of

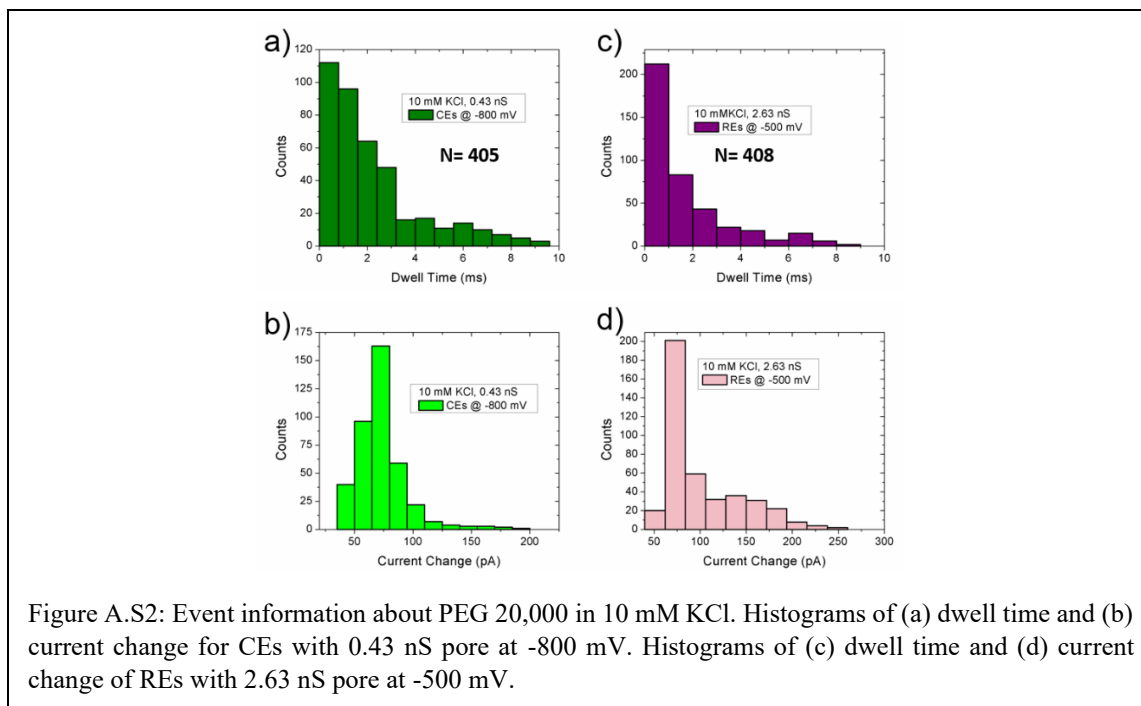
asymmetric salt conditions, the future of solid-state nanopores sequencing nucleic acids is to be expected in the near future. Overall, this work has demonstrated the immense abilities and future capabilities of detecting single molecules with nanopores.

Appendix A: Evaluation of Conductive Pulse Sensing and Its Mechanisms for Enhanced Molecular Sensing

Note A.S1. Translocation of PEG

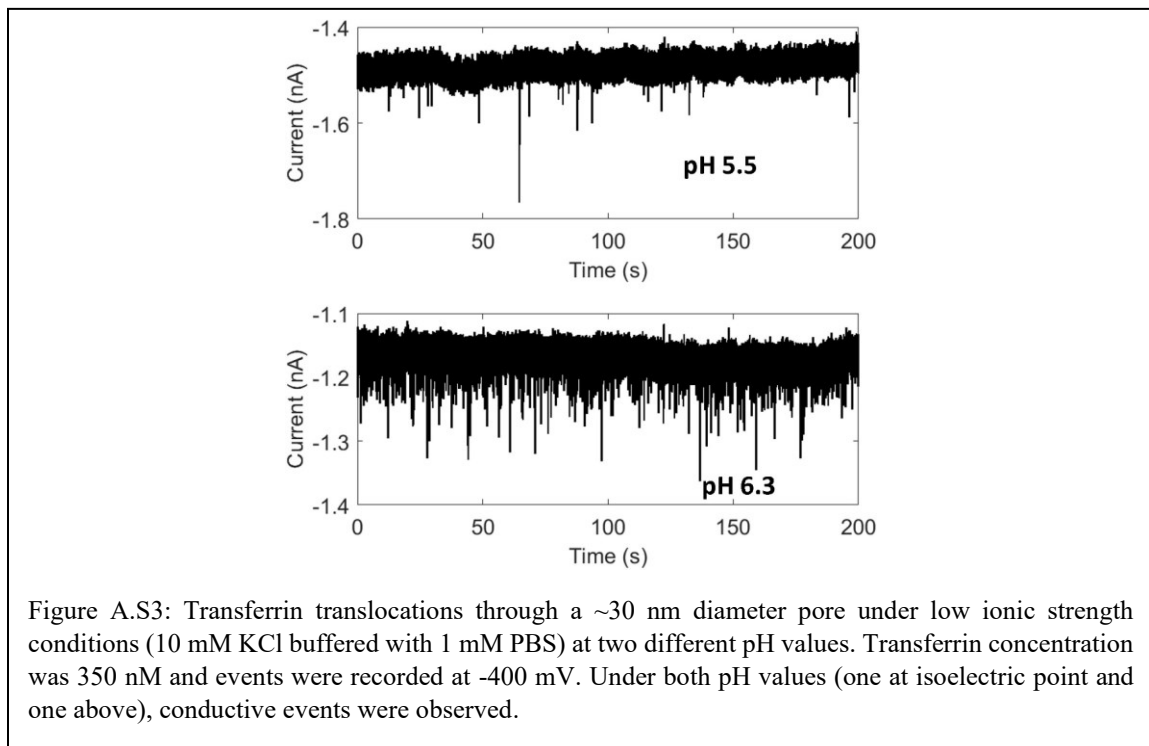
Although the PEG polymer is neutral, when added to KCl it functions like a polycationic polymer due to cation adsorption. PEG 20,000 was diluted to 15% (w/w) in 10 mM KCl and a negative voltage bias was applied wherein PEG events were independently observed with six different pores. Corresponding current traces are shown in Figure A.S1. Interestingly, conductive events (CEs) were most notable at extremely small pore sizes (e.g., 0.43 nS); a pore size regime that we could not observe DNA events. Because PEG is positively charged, we were able to observe events at small pore sizes through EPF unlike DNA (Figure A.S2). Since EOF flow rate decreases with smaller pore sizes and EPF increases, we believe DNA could not energetically overcome the barrier at the pore entrance for translocations to occur. The results indicated that smaller pore sizes





resulted in CEs whereas larger pore translocations yielded resistive events (REs). Consequently, as shown in the main text, when EOF becomes the dominant translocation mechanism, smaller pores yield REs whereas larger pores yield CEs.

Note A.S2. Translocation of Transferrin



Note A.S3. TEM Characterization of Nanopipettes

For TEM imaging and all experiments, nanopores were fabricated through using a laser-assisted pulling machine. To secure the nanopore tip onto the TEM grid, epoxy glue was used. Epoxy was first added into a plastic holder and the nanopore was secured underneath an optical microscope with a microscale actuator. The TEM grid was then held by tweezers and epoxy was applied onto one side of the grid using a plastic stirring rod.

After successful application of epoxy to TEM grid, the grid (glue facing upwards) was then placed underneath optical microscope as well. With the naked eye, the nanopore was moved as close as possible to the epoxy. An optical microscope and micromanipulator were then used to ensure the nanopore tip was just inside the grid, without the pore aperture

touching the epoxy. One last layer of epoxy to secure the nanopore in place was applied once nanopore was in the correct position. This setup was left to dry for 15 minutes.

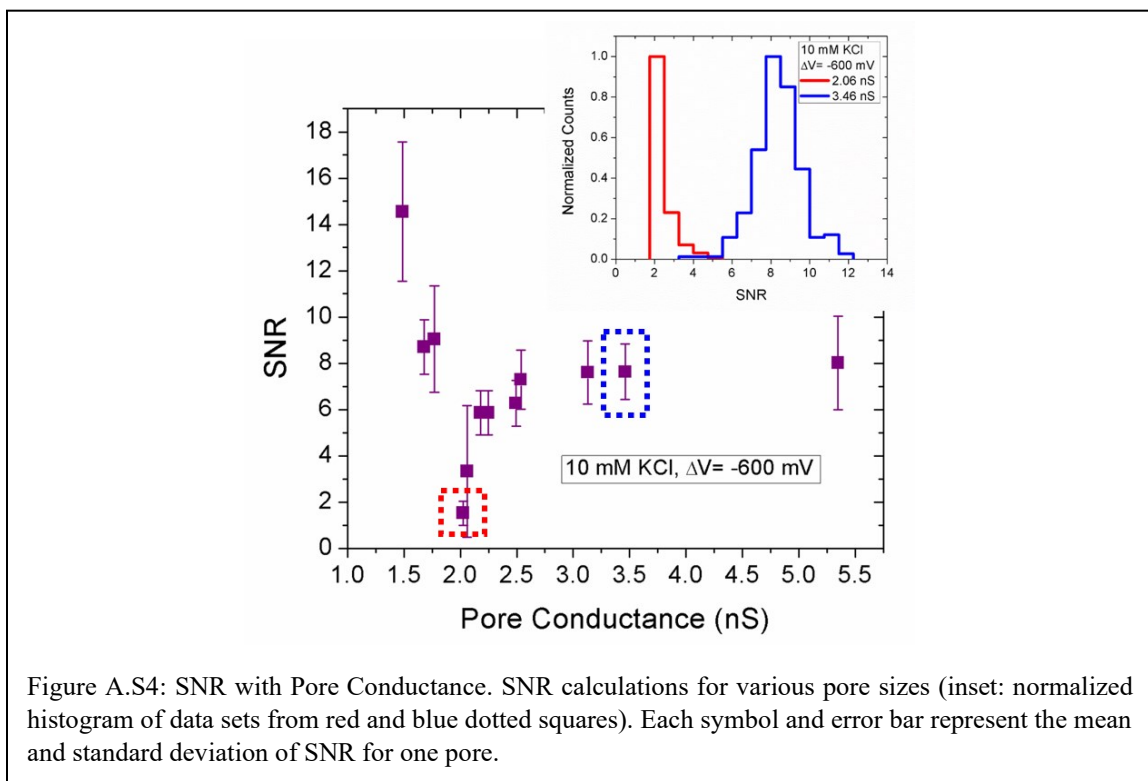
Once 15 minutes has expired, the nanopore was gently broken away from the TEM grid, leaving just the pore inside the grid. Finally, a gold coating was applied to the pore and the grid for preparation of TEM imaging. Specifically, Tecnai12 (Thermo Fisher Scientific) was used for imaging, with a lanthium hexaboride electron source operated at 120 kV.

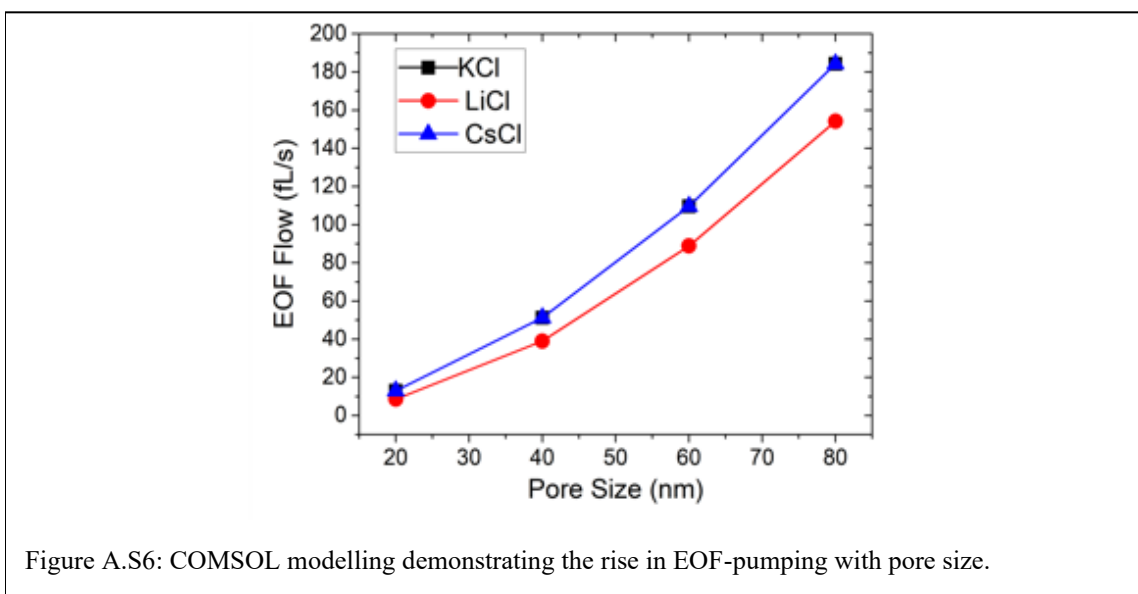
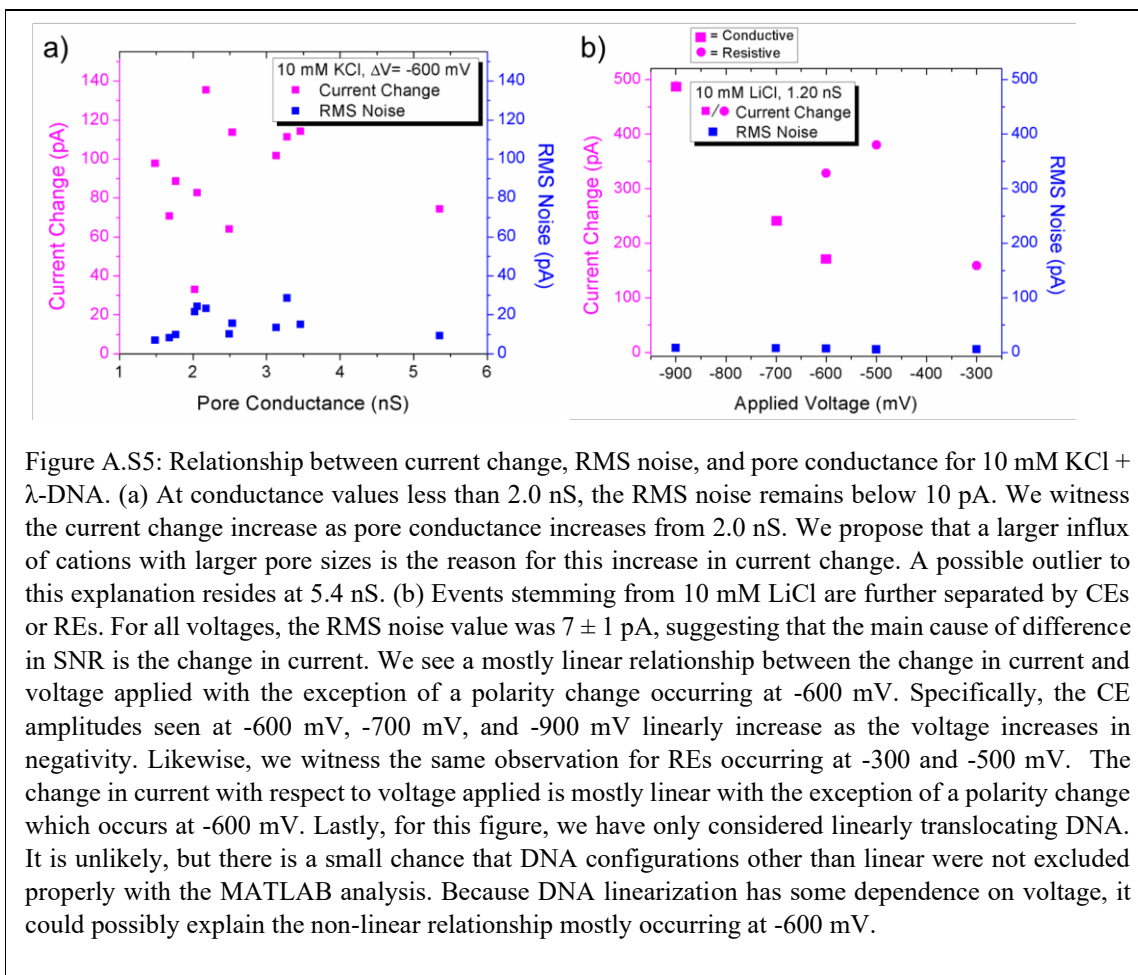
Note A.S4 Signal-to-Noise (SNR) Ratio and Pore Size

For all SNR calculations, we omitted all configurations except for linear DNA translocations. DNA has the ability to translocate linearly, folded, or in knots. To ensure DNA configuration had no effect on SNR, we utilized only linearly translocating DNA to our calculation. We witness an increase in SNR starting at 2.0 nS and saturating around 3.0 nS (Figure A.S4). To determine whether the current enhancement or the noise of the signal is the major contributor to the increase in SNR, we acquired the median current change of all events and the root mean square (RMS) noise of a data segment lacking events.

We witness that the RMS noise maintaining values of 15 ± 7 pA, whereas the current change increases from 30 to 140 pA as pore size increases. For the left side of the graph, we witness a sharp increase in the SNR as the pore size decreases. This can be explained by a decrease in the noise associated with smaller pores.

As seen in Figure S4, the RMS noise is extremely low (< 10 pA) whereas the median current change is approximately 100 pA. Therefore, the higher SNR values for smaller pores stem from lower noise. On the right side of the graph, we speculate that the rise in SNR (and current enhancement) is a result of greater EOF pumping as a function of pore size (Figure A.S6).





Note A.S5: Finite Element Methods

Finite element modelling was developed using COMSOL Multiphysics. The nanopores geometries were built on the TEM images and pulling protocols achieved from the experimental studies. The pore diameters used in figures and text refer strictly to the internal diameters of the most constricting portion of the geometry. The corners of the pore were also curved with an arc radius of 4 nm to avoid anomalies typical of sharp corners. The meshing of the geometry was performed with boundary layers accentuated for increased resolution and accuracy of the ionic flux within these layers (1-10 nm from all surfaces). A conical nanopore with a 25 nm diameter pore and a 4° half-cone angle was used unless otherwise stated. The diffusion coefficients were considered 2E-9 [m²/s] and 1.78E-9 [m²/s] for the potassium (K⁺) and chloride (Cl⁻) ions, respectively. The Poisson, Nernst-Planck, and Navier-Stokes equations were simultaneously solved to model the ionic behavior in a 2D axisymmetric steady-state model. The Poisson's equation [$\nabla^2(V) = -\rho v/\epsilon$] described the relationship between the electric potential and ion transport mechanism. An important dimensional quantity in the Poisson equation is the Debye length, defined as

$$\lambda_D = \sqrt{\frac{RT\epsilon_0\epsilon_s}{F^2I}}$$
 where I is the ionic strength and F is Faraday's constant. Poisson's equation

can also be written as $\rho = F \sum_i c_i z_i$ where ρ is the space charge density of the fluidic domain. In COMSOL, the space charge density was specified within the *Electrostatics* module as well as the *Transport of Diluted Species* module as a volume force acting on the fluid (electroosmotic flow) and was defined specifically for binary electrolytes as: $\rho = N^*e^*z_1*c_1 + N^*e^*z_2*c_2$ where for the electrolyte containing c_1 (K⁺) and c_2 (Cl⁻) ionic species, z and e were set as the valency and electron charge, respectively. The electrostatics

boundary condition used for the glass was set at a surface charge density of $-2E-2$ [C/m^2] in the vicinity of the pore opening to consider the surface charge contributions. The electric potential was set as variable field and the initial values were defined as zero potential.

The Poisson-Nernst-Planck equation was solved for the transport properties and ionic fluxes using convection, diffusion, and migration terms. The equation was described as: $J_i = -D_i \nabla c_i - z_i \mu_{m,i} F c_i \nabla^2 V + c_i u$ where J_i , D_i , c_i , u , $\mu_{m,i}$ and z_i are the ion flux, ion diffusion coefficient, concentration, fluid velocity, ion mobility and the charge number respectively. A no flux ($J=0$) condition was defined on the nanopore walls. The initial concentrations values of K^+ and Cl^- species were set to $10E-3$ [mol/L] for the entire domain. The inlet and outlet of the fluidic chamber was defined using an open boundary condition and the concentrations of the bulk electrolyte. The open boundary condition allows for convective inflow and outflow to occur which is important since convection currents could affect the concentration of ions within the system. The concentration of any “inflow” is set at the bulk value of the concentration. The fluid flow and pressure were modeled by the Navier-Stokes’s equation as: $\rho(u \cdot \nabla)u = (-\nabla p + \eta \nabla^2 u - F (\sum z_i c_i) \nabla \Phi$. The u and Φ are the position dependent velocity field and potential field, z_i and c_i are species i charge and concentration in solution, ρ and η are the fluid density and dynamic viscosity, p is the pressure and F is the Faraday’s constant. Initial values of zero were assigned to the velocity field and pressure. The boundary condition for the pore wall was set to be $u=0$ (no-slip). To model the fluid flow, the volumetric force on the fluid was defined as ions space charge density multiplied by the electric field vectors. The fluid velocity was averaged over a 2D line spanning the nanopore orifice width. Peak velocity was at the center of the pore due to the

zero potential boundary condition for the pore walls. Velocity and pressure were specified as the boundary conditions for the inlet and outlet, respectively.

Note A.S6. Event Rate Calculation

Interevent time (δt) was calculated using a custom MATLAB code. Once interevent information was retrieved, a histogram was developed, and points corresponding to the histogram (δt and normalized counts) were plotted on a semilogarithmic graph. To calculate the event frequency in Figure 2.1e, a different approach was utilized to display more variables within the plot. Using this method, the interevent time for each data file (60 s) was calculated and summed together. The total number of events was then divided by the total interevent time to yield units of events per second for each depth.

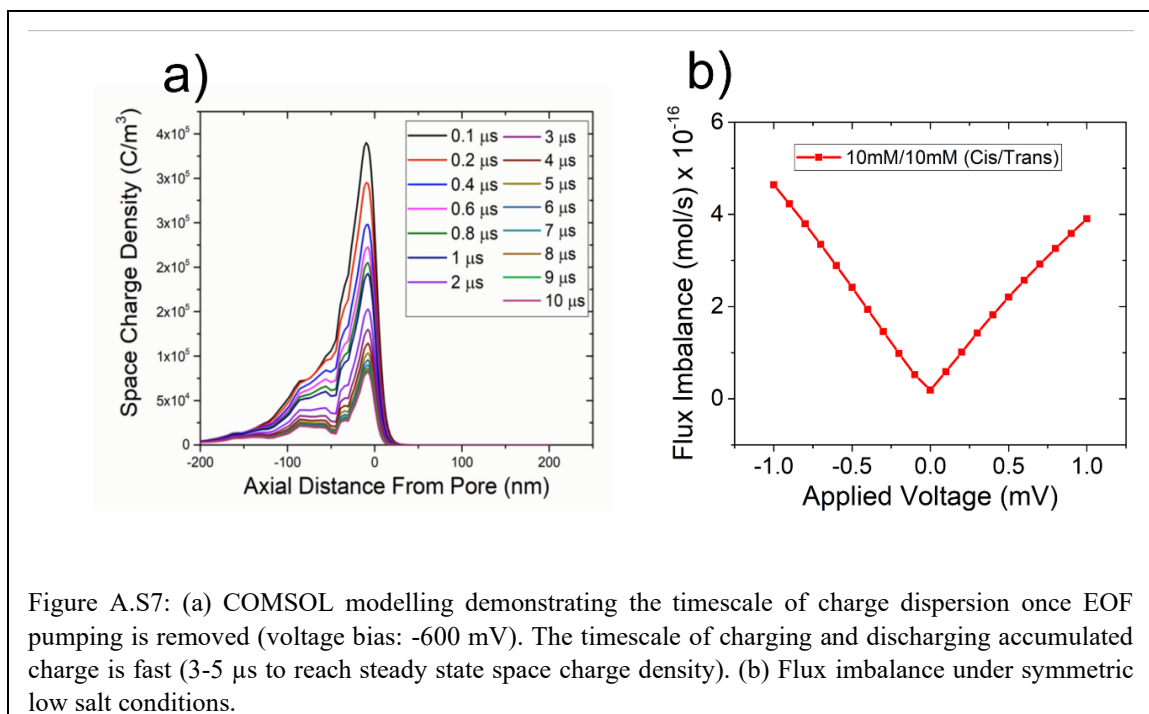
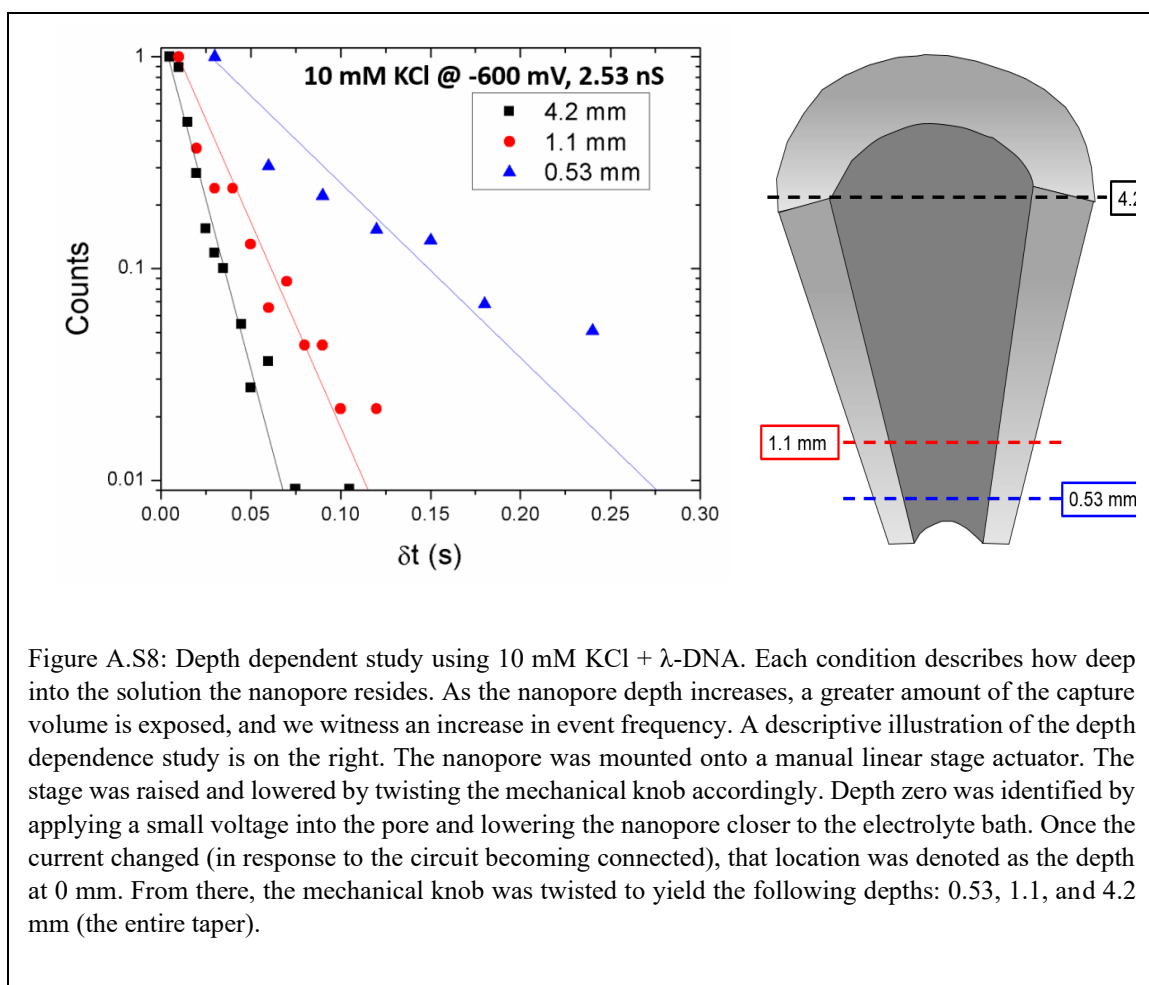


Figure A.S7: (a) COMSOL modelling demonstrating the timescale of charge dispersion once EOF pumping is removed (voltage bias: -600 mV). The timescale of charging and discharging accumulated charge is fast (3-5 μ s to reach steady state space charge density). (b) Flux imbalance under symmetric low salt conditions.

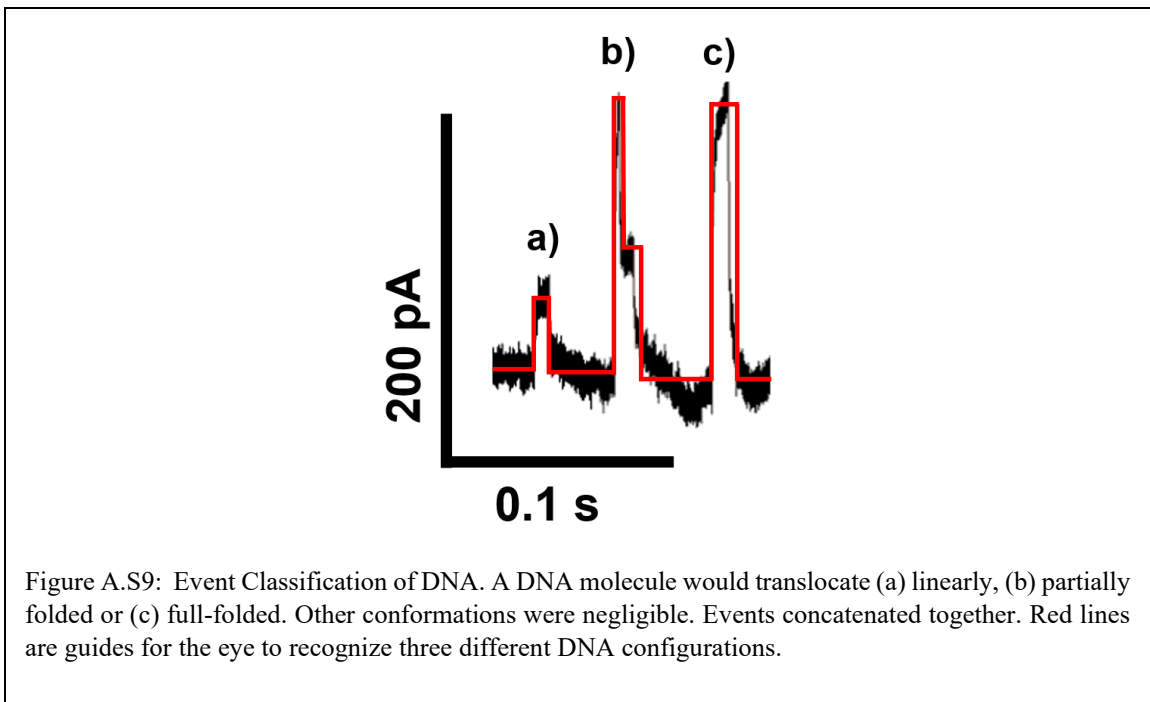
It is important to note that each nanopipette was examined using an optical microscope prior to any experiments. This was performed to ensure the pore was free of any breaks, clogs, or air bubbles that may affect the quality of the current fluctuations. Our largest depth was recorded at 4.2 mm, meaning that the entire taper was submerged within the electrolyte solution. We speculate that the event frequency will not increase vastly above 40 Hz for depths exceeding the entire taper (i.e., the entire capillary), as that would entail the EOF capture zone to extend into the centimeter regime. Further validation of this model is needed but may provide a framework for future experiments.



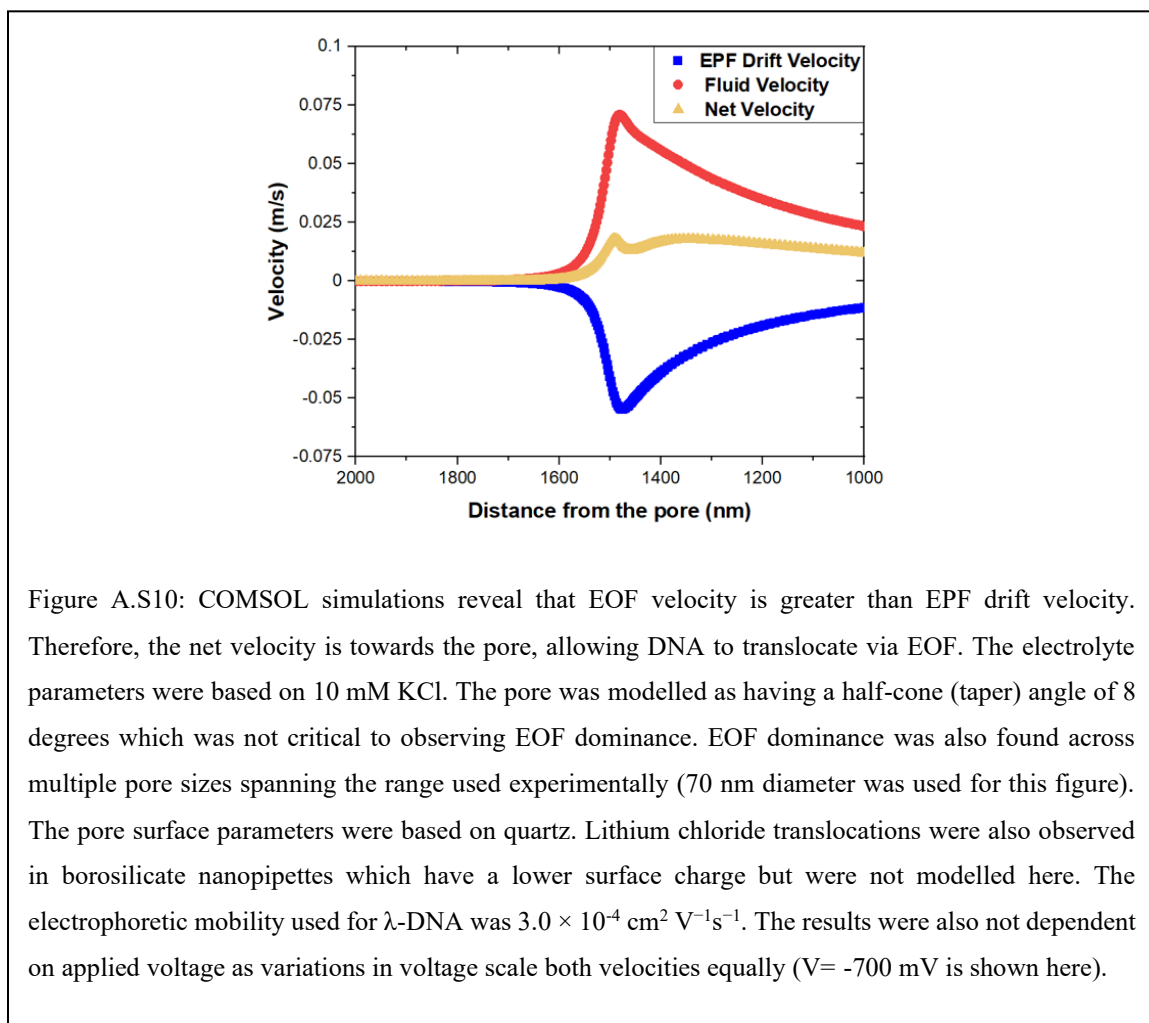
Note A.S7. Event Extraction and Classification of Conformations

Events were extracted from raw current traces by subtracting the baseline variations, and using a thresholding algorithm, an event was flagged for further analysis. For each threshold crossing, the code would iteratively back-track and move forward until the baseline was reached. The full-width-half-max (FWHM) of the event was used for the event duration or dwell time. The maximum current (peak current) and area (in units of $\text{pA}\cdot\text{s}$) for each event was also extracted. These three event properties (event duration, peak amplitude, and area) were fed into a support vector machine classifier that was trained on user-defined folding states of the DNA. After running the classifier, all events were double checked to ensure classification was accurate.

Note A.S8. Electroosmotic versus Electrophoretic Transport and Flux Imbalances



Flux imbalances differ from ion selectivity in that a flux imbalance can be produced through externally manipulating the pore size, salt concentration, voltage applied, or salt type (i.e., KCl, LiCl, CsCl) whereas ion selectivity stems from the properties of the pore itself. Under symmetric, low ionic strength conditions (10 mM KCl), EOF pumps cations into the pore, producing a flux imbalance in favor of K^+ , yielding CEs when DNA translocates the pore. The surrounding pore environment can be altered to have a cationic flux imbalance when a concentration gradient is used (1 M KCl inside and 4 M KCl outside). While a negative voltage is applied inside the pore, K^+ is pumped into the pore



via EPF, producing CEs when DNA exits the pore. Similarly, the pore environment can have a flux imbalance in favor of anions, where 4 M KCl is inside the pore and 1 M KCl is outside. When a positive voltage is applied to attract DNA, Cl^- is pumped into the pore. Upon translocation, REs are generated. Thus, we conclude that a flux imbalance in favor of cations produces CEs and a flux imbalance in favor of anions produces REs.

Note A.S9. Streaming Current

Although the ionic diffusion coefficients and electrophoretic mobilities encapsulate basic transport properties, all the while being utilized as variables in the finite element simulations, they neglect the geometric size of the ions and therefore the packing

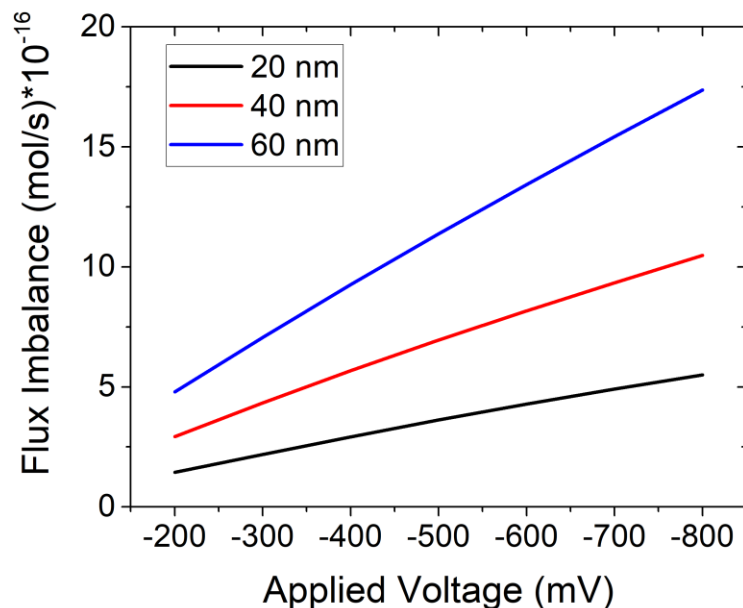
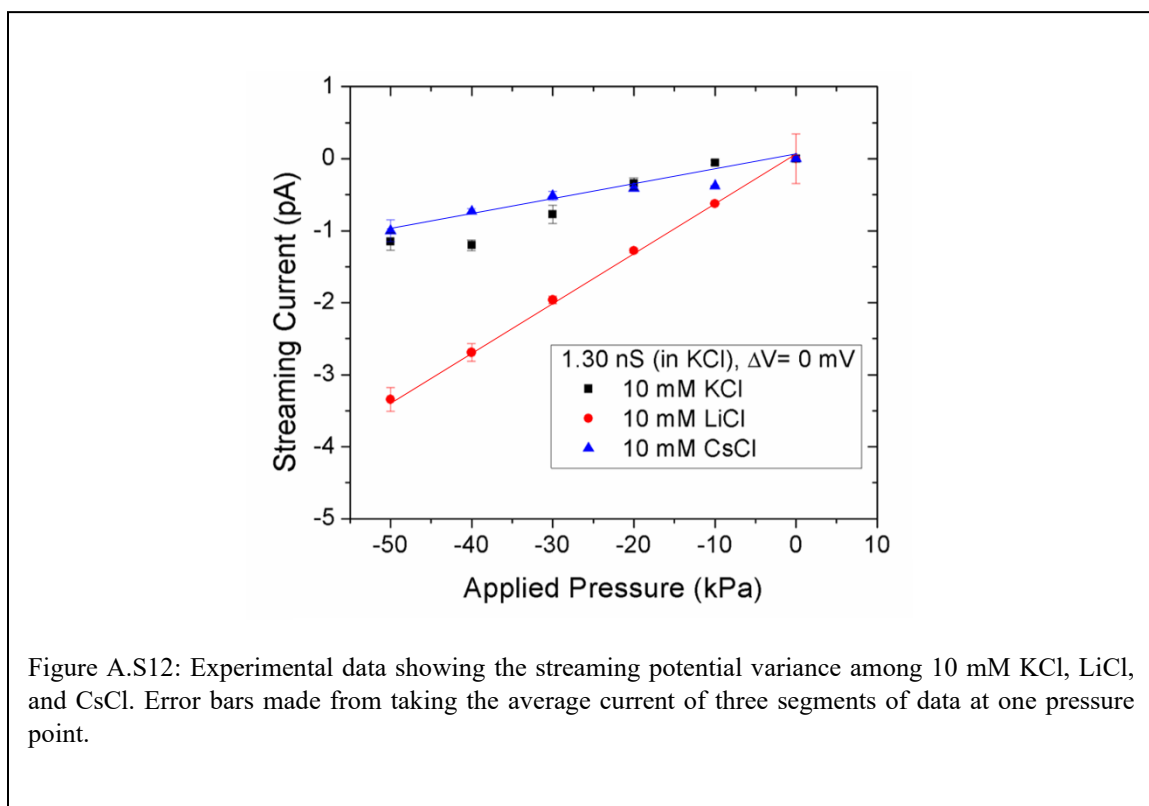


Figure A.S11: COMSOL simulations reveal flux imbalances are voltage and pore size dependent. Flux imbalance was found by integrating the difference in cation flux and anion flux across the pore lumen. Positive flux imbalance indicates that the cation is dominant. The conditions for the simulation included a pore wall with surface charge of 20 mC/m² and a salt concentration of 10 mM. The salt condition used for this figure was KCl.

density/strength on oppositely charged surfaces. To understand the link between electrohydrodynamics and Debye layer screening of the quartz surface charge, streaming current measurements were used as a proxy for cation mobility within the diffuse ion layer. Contrary to EOF, where mobile ions drag fluid, streaming currents measure the fluid's ability to drag along ions co-axial to the fluid motion. A pressure bias was used to generate a streaming current and the resulting data can be seen in Figure A.S12. Negative pressures generate a flow into the nanopore and in the same direction as EOF in our experiments. We see that larger pressures create larger streaming currents. Interestingly, LiCl has significantly higher streaming currents compared KCl and CsCl at negatively biased pressures. The same pore (1.3 nS in 10 mM KCl) was used for all measurements to reduce variability due to different pore sizes.

When an electrolyte solution is traveling through the negatively charged glass nanopore via pressure, an electrical double layer is constructed. In this layer, there is an increase in cation (K^+ , Li^+ , or Cs^+) concentration and a decrease in chloride concentration locally at the pore surface. The resulting electrical double layer produced by streaming



currents is comparable to the Debye screening layer and the streaming potential is directly related to the zeta potential. Thus, by performing streaming current measurements, we obtain information relating to the Debye length and zeta potential at low ionic strength conditions.

Note A.S10. Translocation Characteristics in LiCl and CsCl

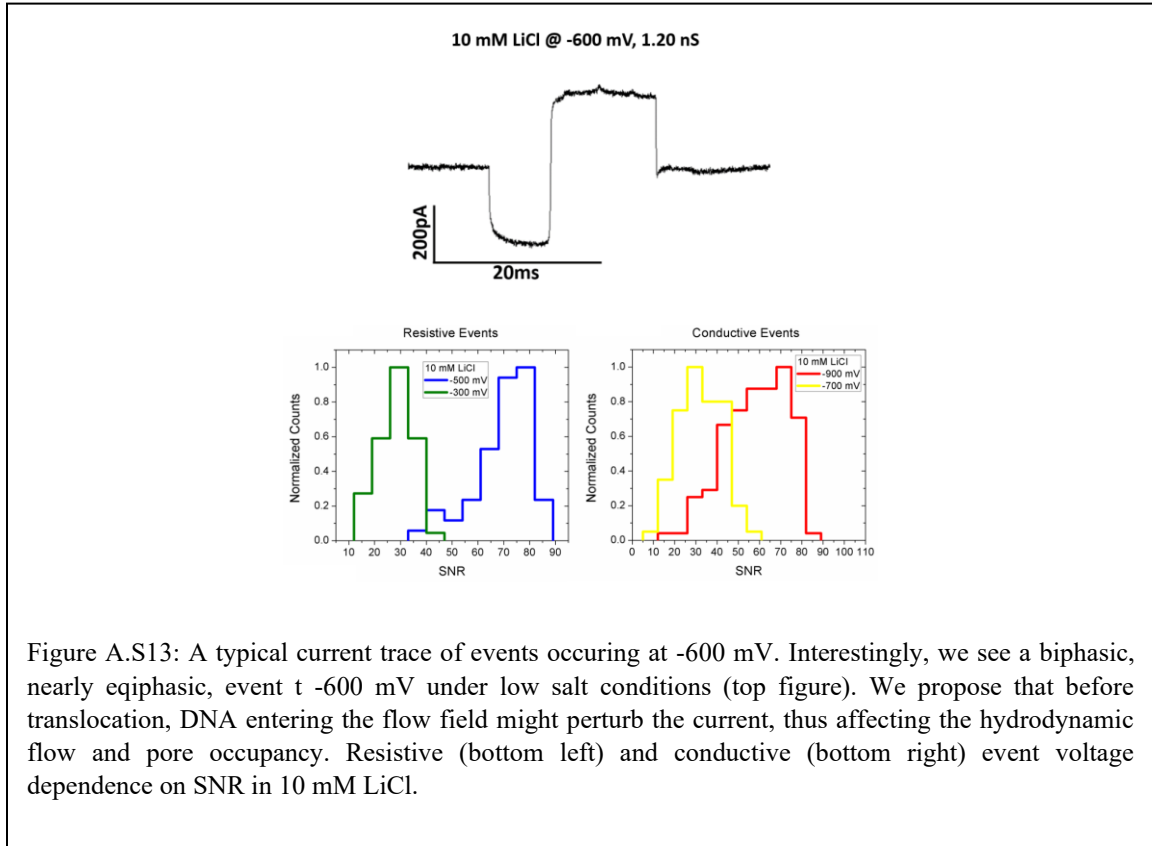
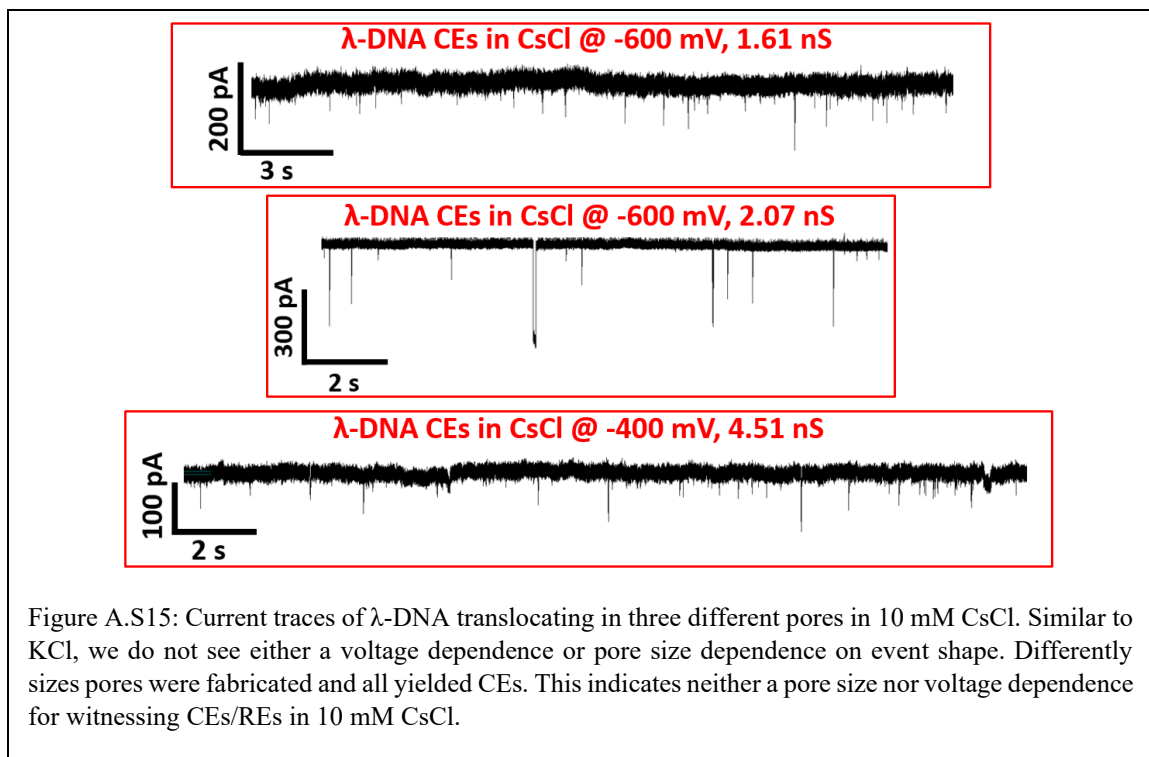
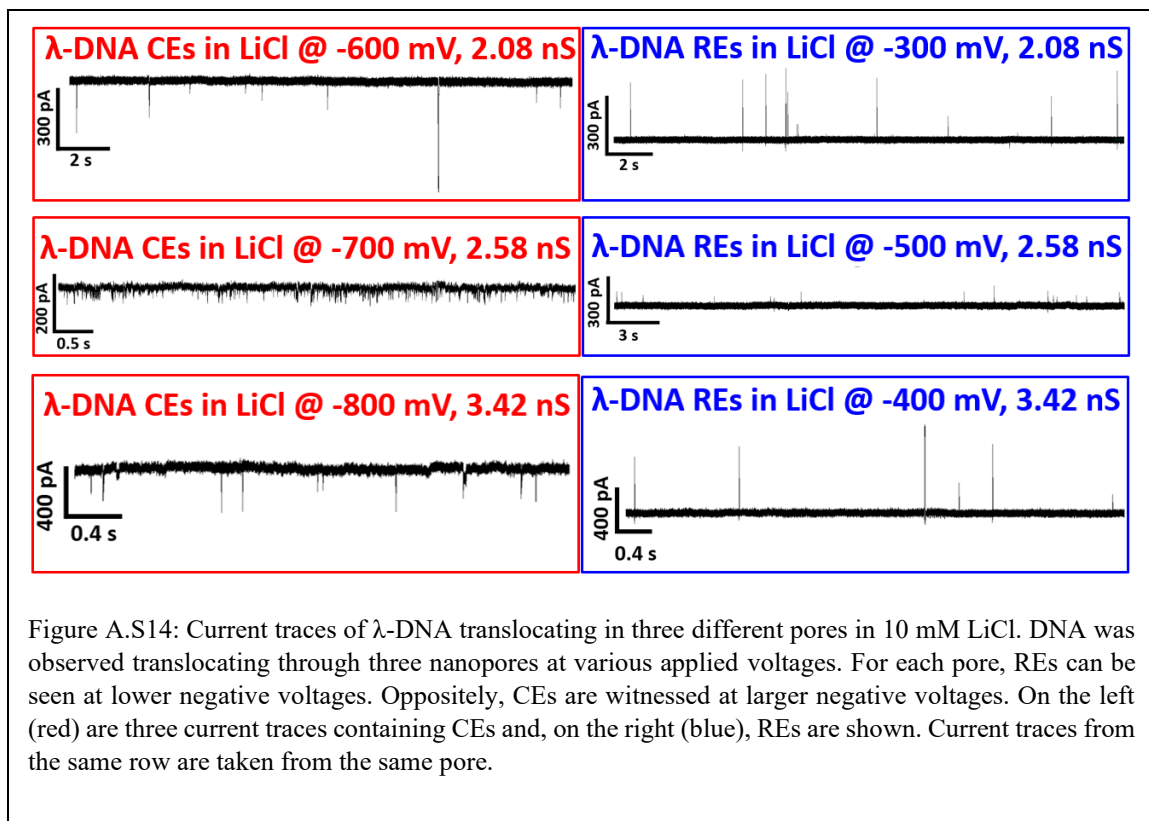
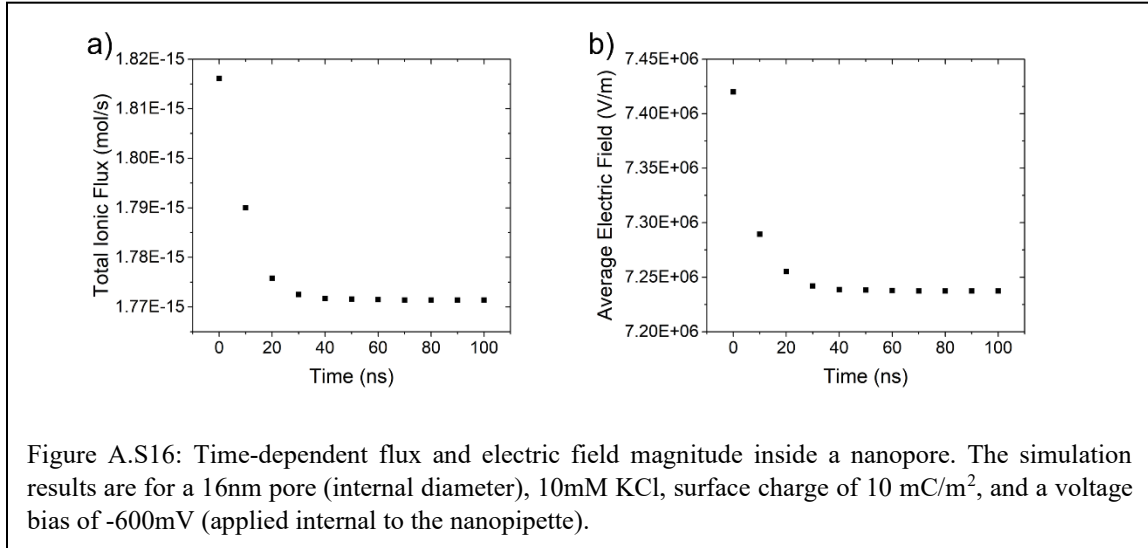


Figure A.S13: A typical current trace of events occurring at -600 mV. Interestingly, we see a biphasic, nearly eqiphasic, event t -600 mV under low salt conditions (top figure). We propose that before translocation, DNA entering the flow field might perturb the current, thus affecting the hydrodynamic flow and pore occupancy. Resistive (bottom left) and conductive (bottom right) event voltage dependence on SNR in 10 mM LiCl.



Note A.S11. Time-Dependent Electric field and Flux Models



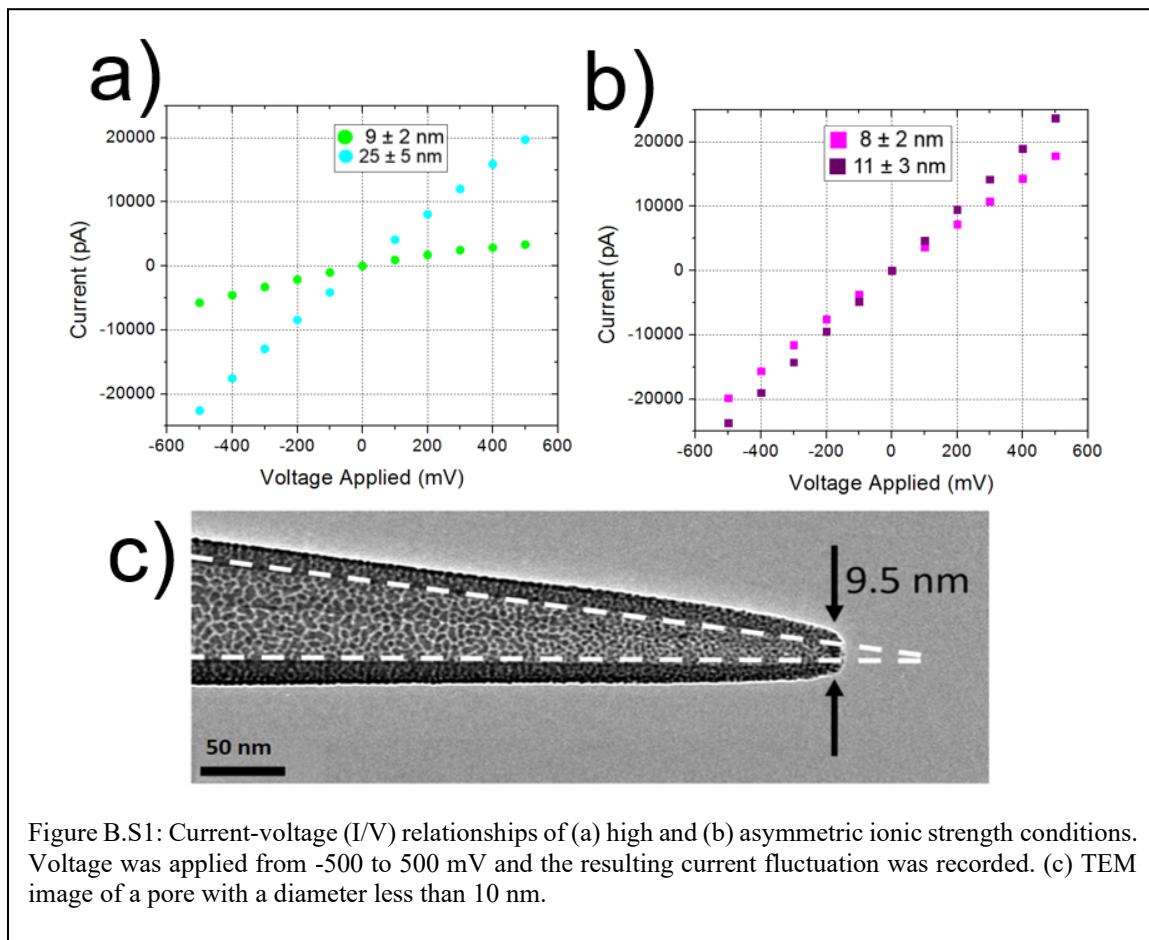
Appendix B: Evaluating Electrolyte Conditions for Enhanced Detection of DNA and Protein Complexes

Note B.S1. Nanopore Fabrication and Set-Up

Quartz capillaries from Sutter Instrument Co. (inner diameter 0.70 mm, outer diameter 1.00 mm, and 7.5 cm length) were plasma cleaned for 5 minutes to remove any surface impurities and contaminations. Afterwards, quartz capillaries were secured within the P-2000 laser puller (Sutter Instrument Co.). A CO₂ laser heated the center of the quartz capillary while the machine simultaneously pulled the ends of the capillary away from each other. The protocol used to fabricate all nanopipettes was used: (1) HEAT: 630; FIL: 4; VEL: 61; DEL: 145; PUL: between 145 and 225. This resulted in two identical, conical nanopores varying in diameter between 50 and 8 nm, respectively. The heat duration was approximately 4.5 s.

Silver wire was dipped in bleach for 30 minutes before each experiment to use as electrodes. Nanopipettes were backfilled with Tris-EDTA (pH 7.4) and either 10 mM KCl, 1 M KCl, or 1 M KCl + analyte (500 pM). After backfilling, an optical microscope was used to inspect the nanopipettes to ensure there were no irregularities at the pore tip. After inspection, the nanopore was secured in the Axopatch head stage with electrodes placed both inside the back end of the pore and within the bath solution. The Axopatch 200B patch-clamp amplifier (Molecular Devices, USA) was used in a voltage clamp mode to measure the ionic current fluctuations. Prior to recording, the gain was always optimized,

and the signal was filtered with a low-pass filter at 10 kHz. A custom MATLAB code was used for data analysis of event characteristics.



Note B.S2. Size Characterization

Current-voltage (I/V) analysis was performed at the beginning of each experiment to reveal the conductance of each pore used (Figure B.S1). The following equation relates pore conductance (G) and inner diameter (d_i) to allow us to estimate the size of the pore aperture:

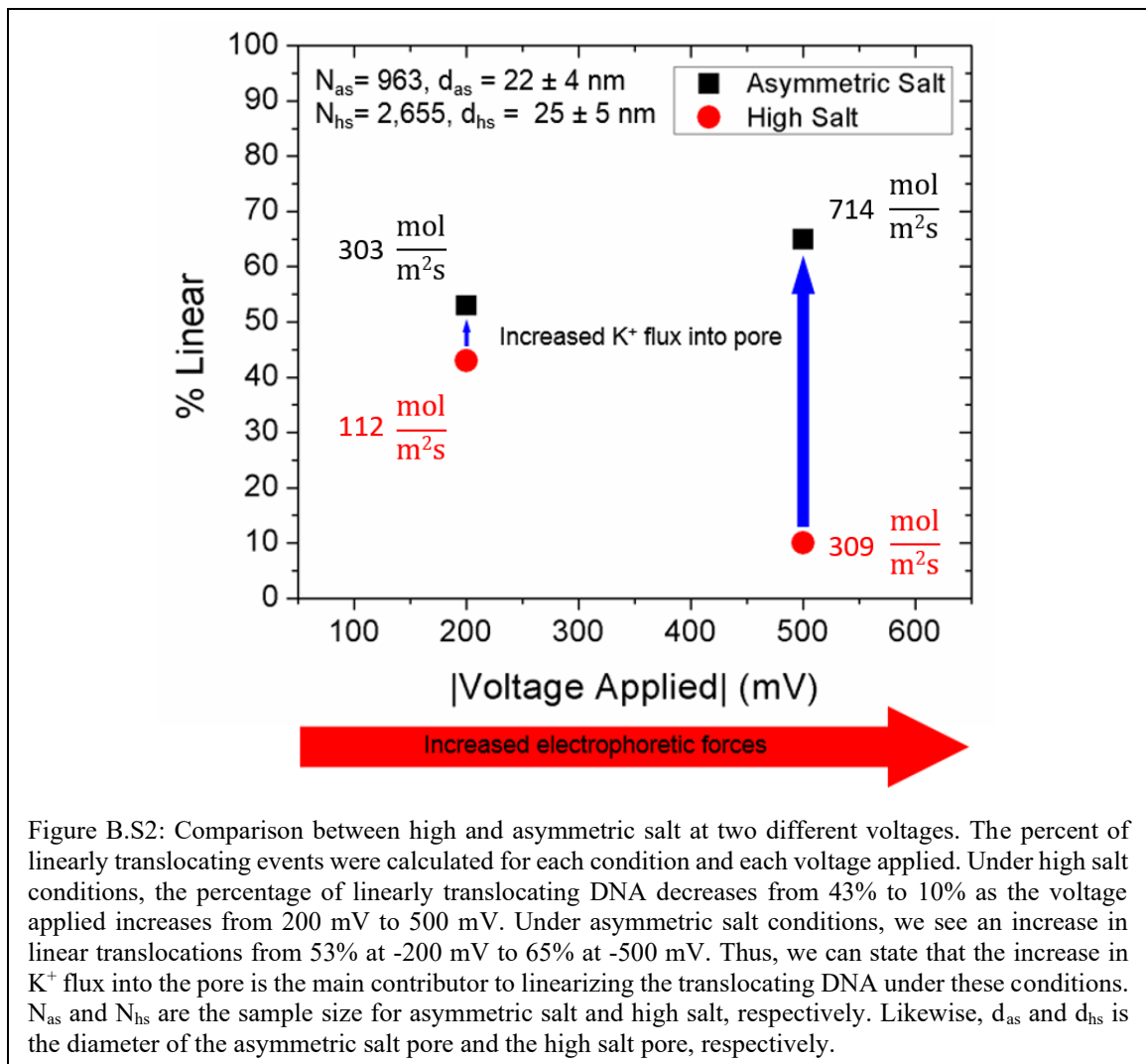
$$d_i = \frac{4Gl}{\pi g d_b} \quad (1)$$

In this equation, l is the length of the conical pore (taper length), d_b is the diameter of the capillary at the beginning of the conical taper, and g is the measured conductivity of the ionic solution. Taper length, l , was recorded using an optical microscope and buffer conductivity was measured using an Accumet AB200 pH/Conductivity Benchtop Meter (Fisher Scientific) at room temperature. This calculation allowed us to estimate the inner pore diameter when using the TEM was unavailable.

Note B.S3. K⁺ Flux

To provide additional documentation surrounding the effect K⁺ flux into the pore plays, regarding DNA configuration, a comparison was performed using two pores of similar size. One pore under high salt conditions yielded electrophoretically-driven DNA translocations at 200 mV and 500 mV. The second pore, under asymmetric salt conditions, also yielded electrophoretically-driven DNA translocations at -200 mV and -500 mV. By keeping the diameter size the same, the only changes seen within these four samples are either due to the electric field strength (difference in applied voltage) or the K⁺ flux into the pore (see main text Figure 3.5c). Because the magnitude of the electric field strength is the same for -200 mV as it is for +200 mV, which is also true for -500 mV and +500 mV, we are able to compare both -200 mV with 200 mV, and -500 mV with 500 mV. The results showing that the K⁺ flux linearizes DNA translocations can be seen in Figure B.S2.

In addition to the comparison of linear translocating events, we sought to compare the capture rates between two conditions: high symmetric (R1) and asymmetric (R3) conditions (Figure B.S3). The reason for selecting R3 to compare with R1 is for the following two reasons: (1) the DNA starting location (in the bath) and (2) the electrical direction of events (resistive in this case) to be the same in both cases. From exponentially fitting the interevent times, the capture rate for R1 was calculated to be ~ 21 events/s and for R3, ~ 35 events/s.



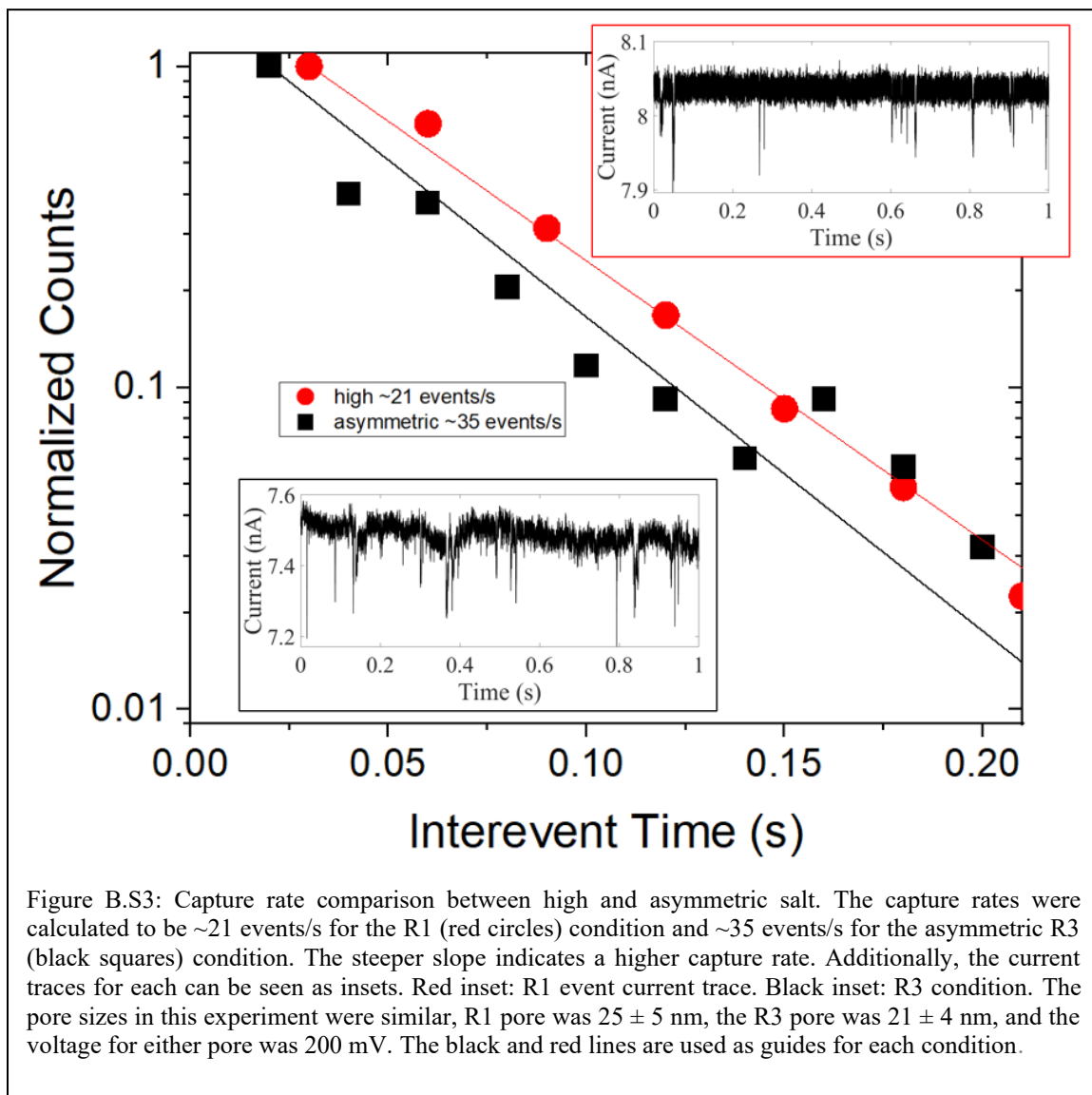
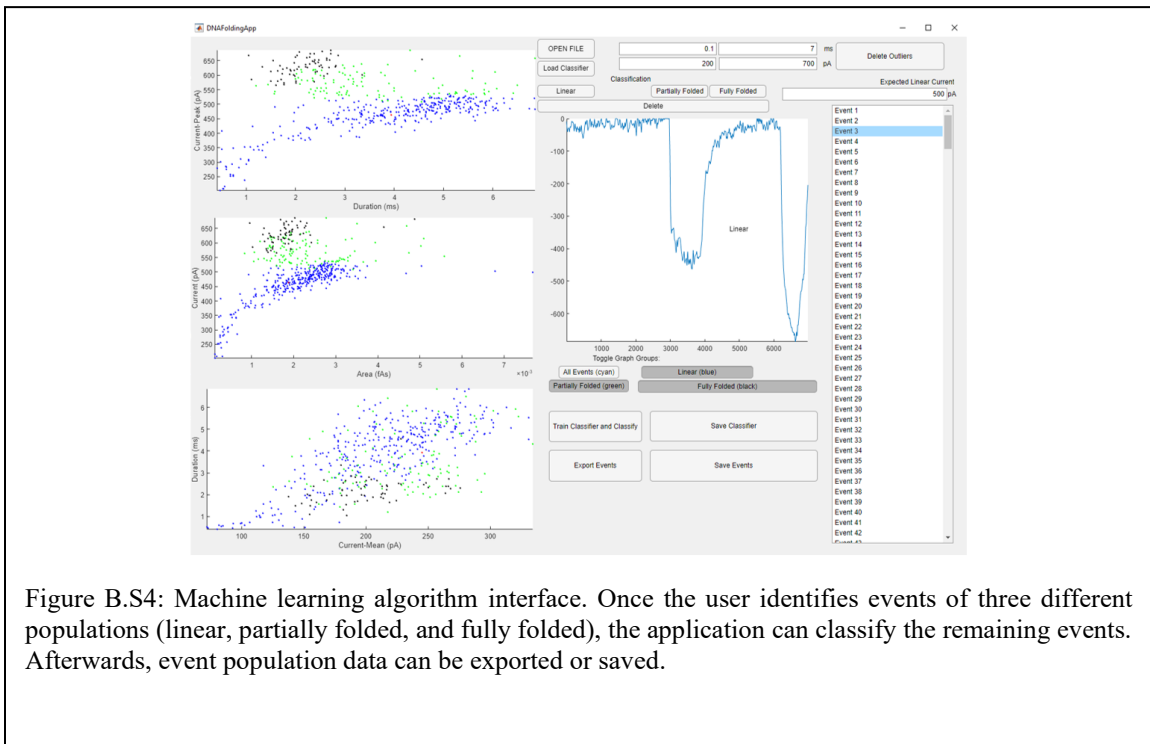


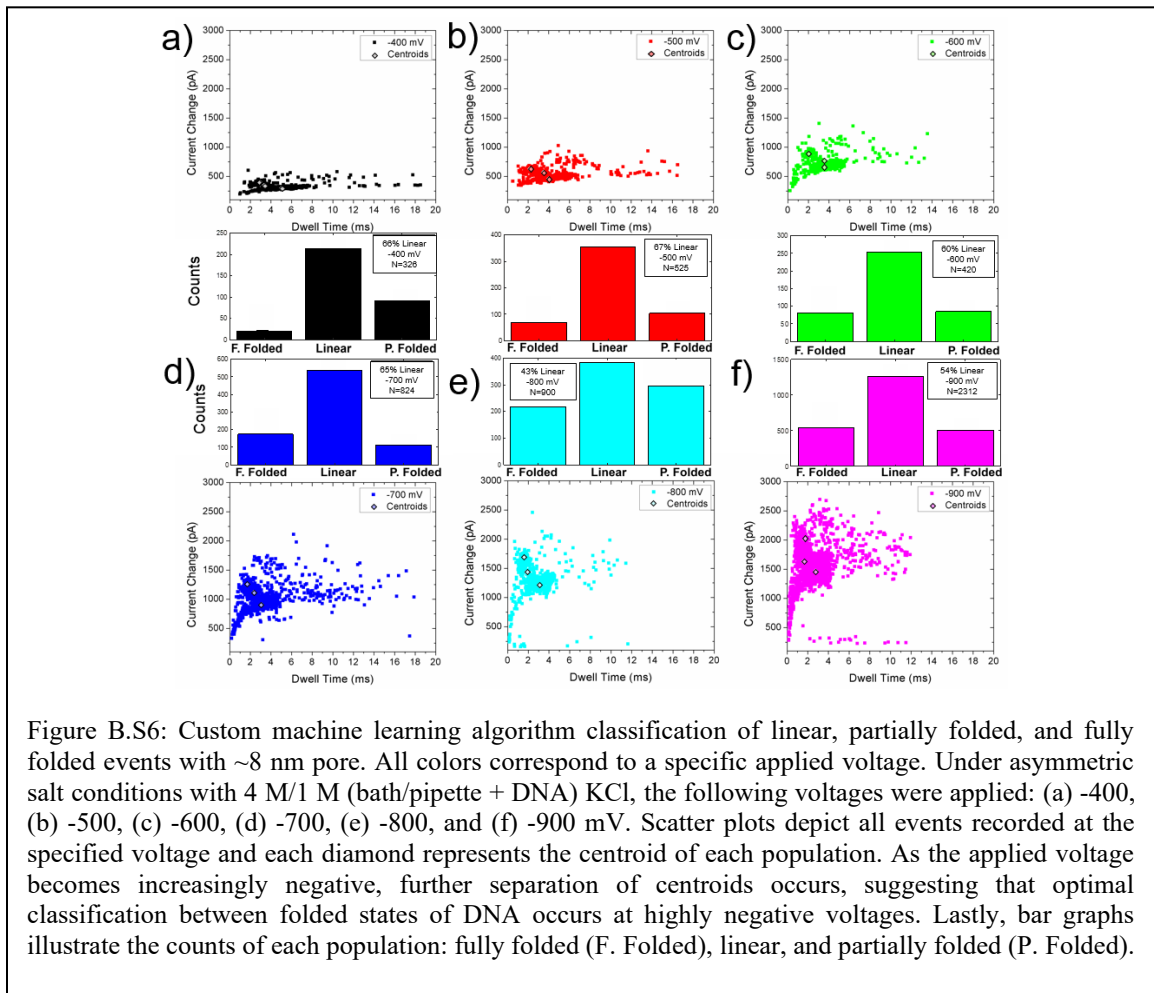
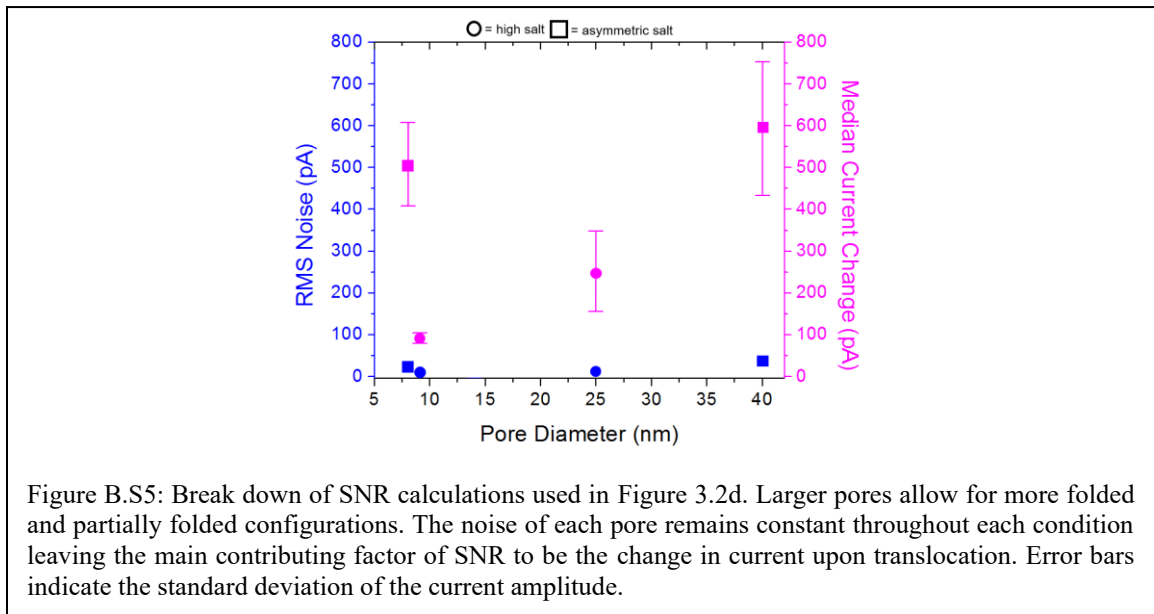
Figure B.S3: Capture rate comparison between high and asymmetric salt. The capture rates were calculated to be ~21 events/s for the R1 (red circles) condition and ~35 events/s for the asymmetric R3 (black squares) condition. The steeper slope indicates a higher capture rate. Additionally, the current traces for each can be seen as insets. Red inset: R1 event current trace. Black inset: R3 condition. The pore sizes in this experiment were similar, R1 pore was 25 ± 5 nm, the R3 pore was 21 ± 4 nm, and the voltage for either pore was 200 mV. The black and red lines are used as guides for each condition.

Note B.S4. Machine Learning DNA Classification

Using MATLAB, machine learning algorithm was developed to classify different DNA configurations translocating the nanopore. Each file with data was passed through MATLAB to retrieve event information at each specific voltage. Once this finished, the algorithm created a scatter plot based of the dwell time and current change of each event.

Using default (linear) kernel functions, three populations of DNA configurations can be classified. In the upper right, there is an option to remove outliers by inputting regions to consider. As such, any unfeasible event was not considered with this analysis. Each event can then be selected by a researcher as either linear, partially folded, or fully folded. Once enough events are classified (more than 10 for each class), the algorithm will determine the nature of the remaining events via linear support vectors. Figure B.S4 displays the interface of the algorithm after events have been classified. From the main text Figure 2d, the calculated RMS noise and current amplitude change for each of the two pores for each condition can be found in Figure B.S5. The machine learning algorithm was also used to classify all DNA configurations occurring with the ~ 8 nm diameter pore under asymmetric salt conditions at multiple voltages. Stemming from main text figure 3c, the remaining % configurations of each class can be found in Figure B.S6.





Note B.S5. Cas9d10a Reaction

The Cas9 mutant, Cas9d10a reaction and incubation procedure was modeled after a protocol provided by New England BioLabs. Reagents including nuclease-free water, buffer, sgRNA, and Cas9d10a were pre-incubated together at 25°C for 10 minutes. Afterwards, DNA was added to the mixture and the entire solution was left to incubate at 37°C for 30 minutes. Both concentrations of sgRNA and Cas9d10a were at 30 nM and the DNA concentration was at 3 nM. This was done to ensure that only two populations: (1) Cas9d10a + sgRNA and (2) Cas9d10a + sgRNA + DNA were within the nanopore.

Note B.S6. COMSOL

Finite element modelling was developed using COMSOL Multiphysics. The nanopores geometries were built on the TEM images and pulling protocols achieved from the experimental studies. The simulation was designed at a low ionic strength electrolyte using the conical nanopore with a 25 nm diameter pore and a 4° half cone angle. The diffusion coefficients were considered 2E-9 [m²/s] and 1.78E-9 [m²/s] for the potassium (K⁺) and chloride (Cl⁻) ions, respectively. The Poisson, Nernst-Planck, and Navier-Stokes equations were simultaneously solved to model the ionic behavior in a 2D axisymmetric steady-state model. The Poisson's equation [$\nabla^2(V) = -\rho/\epsilon$] described the relationship between the electric potential and ion transport mechanism. The electrostatics boundary condition used for the glass was set at a surface charge density of -2E-2 [C/m²] in the vicinity of the pore opening to consider the surface charge contributions. The electric potential was set as variable field and the initial values were defined as zero potential. The

space charge density was defined as $\rho = N^*e^*z_1^*c_1 + N^*e^*z_2^*c_2$ for the electrolyte containing c_1 (K^+) and c_2 (Cl^-) ionic species where z and e were set as the valency and electron charge, respectively.

The Nernst-Planck equation was solved for the transport properties and ionic fluxes using convection, diffusion, and migration terms. The equation was described as: $J_i = -D_i \nabla c_i - z_i \mu_{m,i} F c_i \nabla^2 V$ where J_i , D_i , c_i , $\mu_{m,i}$ and z_i are the ion flux, ion diffusion coefficient, concentration, ion mobility and the charge number respectively. A no flux ($J=0$) condition was defined on the nanopore walls. For low salt simulations, the initial concentrations values of K^+ and Cl^- species were set to $10E-3$ [mol/L] for the entire domain. For asymmetric salt simulations, an internal boundary at the pore orifice was used to define a 1 [mol/L] domain and a 4 [mol/L] domain. The external boundary conditions for each chamber was set to be a fixed concentration that matched the initial conditions of the domain. The electric force driven flow and pressure were modeled by the Navier-Stokes's equation as: $\rho(u \cdot \nabla)u = (-\nabla p + \eta \nabla^2 u - F (\sum z_i c_i) \nabla \Phi$. The u and Φ are the position dependent velocity field and potential field, z_i and c_i are species i charge and concentration in solution, ρ and η are the fluid density and dynamic viscosity, p is the pressure and F is the Faraday's constant. Initial values of zero were assigned to the velocity field and pressure. The boundary condition for the pore wall was set to be $u=0$ (no-slip). To model the fluid flow, the volumetric force on the fluid was defined as ions space charge density multiplied by the electric field vectors. The flux of ions through the pore was the average over a 2D line which spans the entrance of the pore (radius, $r=0$ to $r=\text{pore radius}$). At high salt conditions, the dominant mode of ion transport was electrophoresis.

Note B.S7. First Passage Prediction

The data point at $|\Delta V|=400$ mV was fit using the first passage time equation given by:

$$f(\tau) = \frac{l}{\sqrt{4\pi D\tau^3}} \exp\left(-\frac{(l-v\tau)^2}{4D\tau}\right) \quad (2)$$

where τ , D , v and l are the effective passage or dwell time of DNA, the diffusion coefficient of DNA, the drift velocity of DNA, and the effective sensing length of the nanopipette, respectively. D , v and l were used as fitting parameters in the $|\Delta V|=400$ mV case, and D and l were kept constant for all voltages thereafter ($D=5\times 10^{-10}$ m²/s, $l=10$ μ m). The velocity of DNA was then scaled to the experimentally applied ΔV to show the expected trend in DNA dwell time as shown in Figure B.S7.

